CHAPTER 5

THEORETICAL FRAMEWORK IV: GASTROINTESTINAL TRANSIT MODELS AND INTEGRATION

"The river's current never fails, and yet the water never stays the same."

—Chomei Kamono

5.1 GI TRANSIT MODELS

5.1.1 One-Compartment Model/Plug Flow Model

The one-compartment model is the simplest model used to represent the drug absorption process for oral and other administration routes. Even though it is simple, it is often enough to represent the key features of the drug absorption process. As the Occam's razor principle suggests,[1] when the number of the parameters in the model becomes minimum, the risk of overlearning is minimum.

In the case of oral absorption, the one-compartment model assumes that the small intestine is the main absorption site and neglects the contributions of the stomach and the colon. It was found that the one-compartment model gave satisfactory results when the effect of the stomach pH is negligible [1−6].

---

[1]The simplest model that can explain the observation is the best model. This is also related to parameter distinguishing and identifying abilities.

The following equation is often used to correlate Fa% with the permeation rate coefficient of a drug.

$$Fa = 1 - \exp(-k_{perm}T_{si}) \tag{5.1}$$

5.1.2 Plug Flow Model

Amidon and coworkers [7] used the plug flow model, in which the time parameter is replaced by the distance from the pylorus. The distance is then normalized by the total length of the small intestine as

$$L_{GI}* = \frac{t \times Q_{GI}}{L_{GI}} \tag{5.2}$$

where Q_{GI} is the flow rate along the small intestine. Using this conversion, the dissolution and permeation equations can be rewritten as the function of the normalized position of a particle in the GI tract. These equations were then solved numerically to obtain Fa%. The most significant finding by this approach is that the equations are now expressed using three dimensionless parameters, which are intrinsic to oral absorption of a drug, that is, dose number (Do), dissolution number (Dn), and absorption number (An). This finding is the basis for the bioequivalence guidelines and biopharmaceutical classification system (BCS). A simpler version to derive these parameters is discussed in Section 9.2.

The plug flow model can be regarded as a variation of the one-compartment model (Fig. 5.1a). If the physiological conditions are consistent along the GI
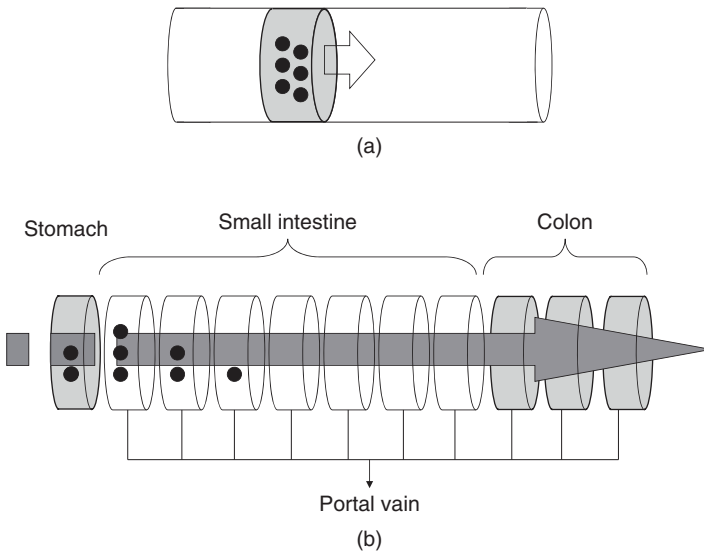

(a)

(b)

Figure 5.1 Plug flow and multiple-compartment models. (a) One-compartment model/plug flow model and (b) Multiple-compartment model (S1I7C3).

tract over time, when one plug compartment moves down the GI tract, the plug flow model becomes identical with the one-compartment model. Therefore, the analytical solution for the plug flow model and the one-compartment model becomes mathematically identical.

5.1.3 Three-Compartment Model

The GI tract should be divided into at least three compartments, the stomach, the small intestine, and the colon, to reflect the significant differences in the physiological conditions of these sections (S1I1C1 system,[2] mixed tank model). The transit kinetics could be zero order, first order, etc., to represent the observed GI transit profile. Despite of its simplicity, the predictability is appropriate for many cases and has been employed often in the literature.

5.1.4 S1I7CX (X = 1–4) Compartment Models

To represent the regional differences, the small intestine and the colon can be divided into multiple compartments. On the basis of the best fitting to the distribution of the colon exit time, when the first-order transit kinetics was applied for the transfer between the compartments, the optimal compartment number for the small intestine was found to be 7 [8, 9].

The S1I7CX (X = 1–4) system is operationally convenient to represent the regional differences of the GI physiology, such as pH, bile concentration, and transporter and metabolic enzyme expression levels. Several variations of the S1I7CX system have been reported in the literature, such as the advanced compartment absorption transit (ACAT) model [10], the gastro-intestinal transit absorption (GITA) model [11–14], and the advance dissolution absorption and metabolism (ADAM) model [15] (Figs. 5.1b and 5.2).

The movement of the API particles, the dissolved drug, the GI fluid between the compartments can be represented by the first-order kinetics.

$$\frac{dN_{API,GI,k}}{dt} = K_{t,k-1}N_{API,GI,k-1} - K_{t,k}N_{API,GI,k} \tag{5.3}$$

$$\frac{dX_{dissolv,k}}{dt} = K_{t,k-1}X_{dissolv,k-1} - K_{t,k}X_{dissolv,k} \tag{5.4}$$

$$\frac{dV_{GI,k}}{dt} = K_{t,k-1}V_{GI,k-1} - K_{t,k}V_{GI,k} \tag{5.5}$$

where $K_{t,k}$ is the first-order transit rate constant ($=$ compartment number/mean transit time, T_{si}) [8]. The movement of particles represented by the S1I7C1 system is shown in Figure 5.3 [16]. According to the S1C7C1 system, drug particles are widely dispersed in the small intestine at 120 min.

---

[2]In this book, the compartment systems were expressed such as S1I1C1 in which S, I, and C corresponds to the stomach, small intestine, and colon, respectively, and the following number indicates the number of compartment.
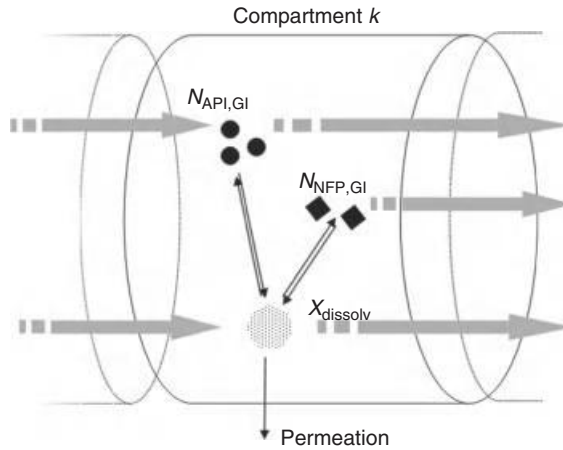
Figure 5.2 Mass balance in a compartment. N_{API} and N_{NFP} are the numbers of original API particles and newly formed precipitated particles, respectively.
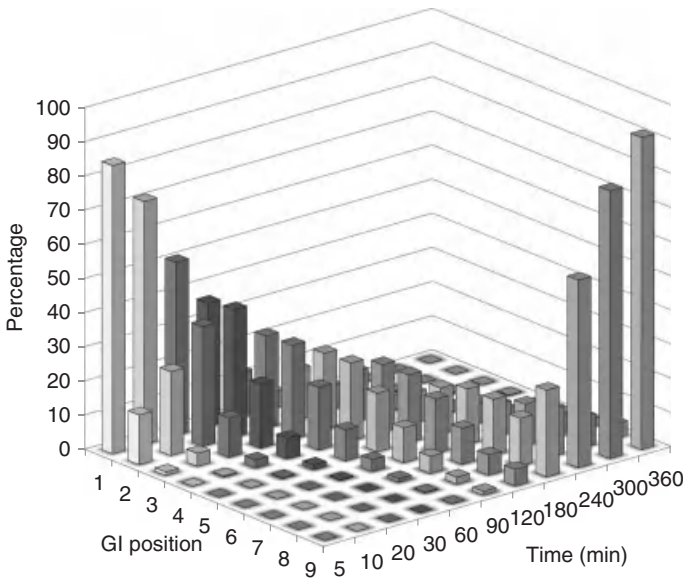

Figure 5.3 Particle distribution represented by the S1I7C1 model [16].

However, it should be stressed that the real small intestine is a continuous tube rather than a series of compartments with unlimited capacity. Therefore, this model is not a physiological model as in the same sense of the phys-iologically based pharmacokinetics model. In addition, when looking at the individual experimental data, the distribution of the colon exit time looks as it follows the zero-order kinetics. It is not clear how much advantage the S1I7CX

systems have when compared with the simpler models. As discussed in Section 13.6.3, the regional difference of permeability in the small intestine has been merely observed and the one-compartment approximation of the small intestine has been working well. In the case of permeability-limited absorption, the one-compartment model gives almost identical Fa% with the S1I7CX model (Section 5.3.3). In most drugs, it is arguable whether the model should be made complex at the cost of simplicity or not (Chapter 16). Nevertheless, the S1I7CX model is currently employed by many commercial programs as the *de facto* standard model.

5.1.5   Convection–Dispersion Model

The dispersion model describes the transit of drugs through the continuous intestinal tube by convection and dispersion [17].

$$\frac{\partial N_{\text{API,GI}}(k,t)}{\partial t} = \text{Disp}\frac{\partial^2 N_{\text{API,GI}}}{\partial^2 k} - \text{Vc}\frac{\partial N_{\text{API,GI}}}{\partial k} \tag{5.6}$$

$$\frac{\partial X_{\text{dissolv,GI}}(k,t)}{\partial t} = \text{Disp}\frac{\partial^2 X_{\text{dissolv,GI}}}{\partial^2 k} - \text{Vc}\frac{\partial X_{\text{dissolv,GI}}}{\partial k} \tag{5.7}$$

where Disp is the dispersion coefficient and Vc is the velocity of the intestinal fluid. Similar approach was taken by Willmann et al. [18, 19].

5.1.6   Tapered Tube Model

Considering the peristaltic and mucociliary movements of the small intestine, the transit of a drug through the small intestine should follow the zero-order kinetics, rather than the first-order kinetics that is employed in the S1I7CX model. The observed data for the colonic exit time in each individual patient looks as it follows the zero-order kinetics [9]. Therefore, in biopharmaceutical modeling, it might be appropriate to treat the small intestine as a tube with a movement like a belt conveyor (Fig. 5.4). As the fluid in the stomach is excreted (cf. this is a first-order kinetic process), the fluid is pushed along the tube of the small intestine. This band of the fluid then moves down the tube like by a belt conveyor. The distribution of the fluid would be widened as the diameter of the small intestine becomes narrower in the distal position.

To computationally simulate the drug transfer in the GI tract as discussed above, it is convenient to model the small intestine as a series of compartments with a limited volume capacity. The number of the compartments should be sufficient to approximate the tapered tube shape [e.g., 100 ellipse cylinders with the length and circumference of 3 cm and 10–6 cm (proximal to distal), respectively]. The stomach can be modeled as one compartment and the stomach fluid is excreted into the small intestine following the first-order kinetics. As the fluid in the stomach is excreted into the small intestine, owing to the limited fluid capacity of each compartment, the fluid fills the compartment one after the other in the proximal small intestine. The drug particles then move down the small intestine

Figure 5.4 Schematic representation of tapered tube model. The gray part indicates the distribution of a drug. The stomach is modeled as one compartment. The fluid excretion from the stomach is modeled by the first-order kinetics. As the fluid in the stomach is excreted into the small intestine (0–45 min), because of the limited fluid capacity of each compartment, the fluid fills the compartment one after the other in the proximal small intestine. The drug particles then moves down the small intestine following the zero-order kinetics (like by a belt conveyor).
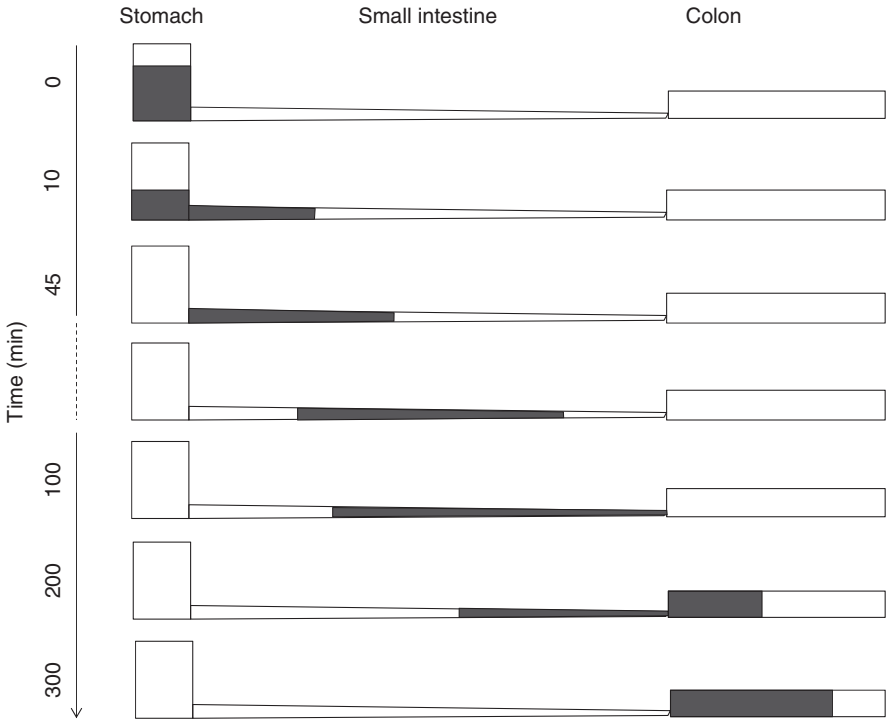
following the zero-order kinetics (like by a belt conveyor). The forefront of the drug particles moves to the next compartment ca. every 1 min, so that it takes ca. 100 min to exit into the colon. The zero-order flux at the small intestine–colon junction can be set to represent the colon exit time distribution with the mean exit time of 210 min and the back-end exit time to be ca. 300 min.

5.2   TIME-DEPENDENT CHANGES OF PHYSIOLOGICAL PARAMETERS

5.2.1   Gastric Emptying

Gastric empting is usually simulated as a first-order kinetic process. In the fed state, gastric emptying rate depends on the nutrition state (Sections 6.2.1.1 and 12.2.1).

Depending on the dose timing during the myoelectric motor complex (MMC) phase (Section 6.2), the excretion from the stomach can be multiphase, resulting in a multiple peak C_p time profile. This multiphase excretion can be simulated by programming a timed excretion with first-order kinetics. For example, in the MMC phase III, $T_{1/2}$ can be set to 10 min and the duration of MMC phase III can be set to ca. 2–15 min.

5.2.2 Water Mass Balance

The water content in the GI tract is determined by the balance of an ingested water volume, fluid secretion, and absorption. In the fasted state stomach, the fluid inflow is 2.1 ml/min (as zero order, saliva + gastric juice) and is transferred into the duodenum with a half-life of 10–15 min (as first order). Figure 5.5 shows the simulation of the stomach fluid volume when 250 ml of water is ingested. The steady state fluid volume is ca. 30 ml, and the steady state is quickly re-established after ingestion of water. This fluid volume change should be taken into account for biopharmaceutical modeling of free bases (Section 8.6).

In a similar way, the fluid volume change can be calculated for the small intestine and the colon. However, as the steady state is quickly established, the use of a constant volume would be a good approximation.
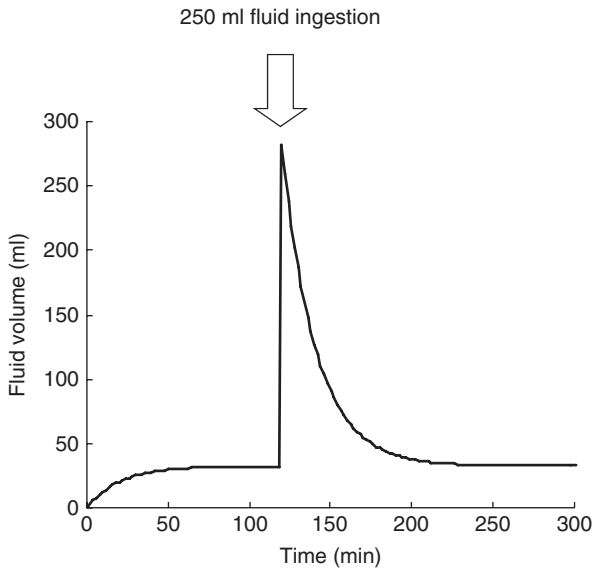

Figure 5.5 The simulated time course of the stomach volume after bonus administration of 250 ml of water. Secretion of saliva and gastric juice and gastric emptying were simulated as the zero-order (2.1 ml/min) and first-order ($T_{1/2} = 10$ min) kinetics, respectively.

Example   The steady state volume in the stomach with the secretion rate $=$ 2.1 ml and emptying half-life $=$ 10 min can be calculated as follows:

The mass balance at the steady state is

$$\text{Secretion per time} = \frac{\ln 2}{\text{Transfer } T_{1/2}} \cdot \text{Steady state volume}$$

By rearranging this equation and input the secretion rate and the emptying half-life,

$$\text{Steady state volume} = \text{Secretion per time} \times \frac{\text{Transfer } T_{1/2}}{\ln 2}$$

$$= 2.1 \frac{10}{0.693} = 30.3 \text{ ml}$$

5.2.3 Bile Concentration

After being secreted from the bile duct into the duodenum, the bile is diluted by the fluid coming from the stomach. As the fluid moves down the small intestine, water will be reabsorbed and the bile concentration will go up ca. twofold. At the end of the ileum, the bile acid is almost completely reabsorbed (Fig. 6.18). This dynamic change of bile concentration is suggested to be one of the reasons for the bimodal absorptions of some drugs (Section 13.6.3). The fluid composition changes more dynamically in the fed state than in the fasted state [20]. This change can be represented by assigning a different bile concentration to each small intestinal region.

5.3 INTEGRATION 1: ANALYTICAL SOLUTIONS

As the kinetic processes of oral absorption are expressed by sequential differential equations, integration of these equations is required to obtain observable values, such as the fraction of a dose absorbed (Fa) and plasma concentration (C_p) time profile. There are two methods to integrate the differential equations, analytical solution and numerical integration.

Traditionally, the quest for analytical solution(s) was the only way to apply the scientific theories for practical prediction. Some approximation is often applied to obtain an approximate analytical solution. When we obtained an analytical solution, we could say that we understood it.[3] However, analytical solution is obtainable only for very few specific cases (but these cases are often the most important and essential cases). Therefore, to solve a complex problem, computational numerical integration is required. As the computational speed increases,

---

[3]In addition, an analytical solution is less liable for calculation error. Analytical solution is often used to validate the numerical integration program.

numerical integration becomes more and more available for many scientists. Numerical integration is very powerful and enables us to have answers for many complicated cases for which analytical solution cannot be obtained.

In this book, as in the other textbooks of physics, analytical solutions for some essential cases are first discussed. Understanding of these essential cases is important for interpreting the results from numerical integration.

5.3.1 Dissolution Under Sink Condition

5.3.1.1 Monodispersed   Particles. The Nernst–Brunner equation for monodispersed spherical particles with $r_{p,ini} < 30$ μm in a sink condition[4] is obtained by combining surface area per particle (SA$_p$), particle number (N_p), mass transfer coefficient ($D_{eff}/L/Sh$, at < 30 μm, $L/Sh = h = r_{p,ini}$), and surface solubility ($S_{surface}$)

$$\frac{dX_{API,t}}{dt} = -SA_p \times N_p \times \frac{D_{eff}}{L/Sh} \times S_{surface}$$

$$= -4\pi r_p^2 \times \frac{X_{t=0}}{\left(\frac{4}{3}\pi r_{p,ini}^3\right)\rho_p} \times \frac{D_{eff}}{r_p} \times S_{surface}$$

$$= -\frac{3D_{eff}S_{surface}}{r_{p,ini}^2\rho_p} X_{API,t=0}^{2/3} X_{API,t}^{1/3}$$

$$= -k_{diss} X_{API,t=0}^{2/3} X_{API,t}^{1/3} \tag{5.8}$$

$$\left(k_{diss} = \frac{3D_{eff}S_{surface}}{r_{p,ini}^2\rho_p}\right) \tag{5.9}$$

By rearranging Equation 5.9,

$$X_t^{-1/3}\frac{dX_t}{dt} = -k_{diss} X_{API,t=0}^{2/3} \tag{5.10}$$

By integrating this equation and rearranging, we obtain

$$\text{Dissolved \%} = 1 - \left(1 - \frac{2}{3}k_{diss}T_{si}\right)^{3/2} \qquad r_{p,t=0} < 30 \text{ μm} \tag{5.11}$$

This is the exact analytical solution of the Nernst–Brunner equation for the dissolution of monodispersed particles with $r_{p,ini} < 30$ μm in a sink condition.

---

[4]When $C_{dissolv}/S_{dissolv} < 0.3$, it is called *sink condition*.

Similarly, for > 30 μm cases, assuming that h_{API} is constant ($= 30$ μm), we obtain

$$k_{diss} = \frac{3D_{eff}S_{surface}}{r_{p,ini}h_{API}\rho_p} \tag{5.12}$$

$$\text{Dissolved \%} = 1 - \left(1 - \frac{1}{3}k_{diss}T_{si}\right)^3 \qquad r_{p,t=0} > 30 \text{ μm} \tag{5.13}$$

This equation is not an exact analytical solution because, as the particles dissolve, the particle radius becomes less than 30 μm and the h_{API} is no longer a constant (Fig. 5.6).

When an approximation of $X_{t=0}^{2/3}X_t^{1/3} \approx X_t$ is employed,

$$\frac{dX_{API,t}}{dt} = -k_{diss}X_t = -k_{diss}X_{API,t} \tag{5.14}$$

This is a first-order kinetic equation. Therefore, by integrating Equation 5.14, we obtain an approximate analytical solution as

$$\text{Dissolved \%} = 1 - \exp(-k_{diss}t) \tag{5.15}$$

Figure 5.6 shows the comparison between the exact and approximate analytical solutions. Considering variations of *in vivo* data and various other errors for *in vivo* predictions (Section 16.1), the first-order approximation would be reasonable for *in vivo* oral absorption prediction. In addition, when Dissolved % $< 60–70\%$, the zero-order, first-order, and exact analytical solutions become similar.

5.3.1.2 Polydispersed Particles. As discussed in Section 3.2.3.2, polydispersed particles can be represented as the sum of monodispersed particles. Therefore, the Noyes–Whitney equation becomes

$$\frac{dX_{API,t}}{dt} = \sum_{PSB} f_{PSB} \frac{dX_{API,PSB,t}}{dt} = \sum_{PSB} -f_{PSB}SA_{p,PSB} \times N_{p,PSB} \times \frac{D_{eff}}{L/Sh} \times S_{surface} \tag{5.16}$$

Figure 5.7 shows the comparison between the dissolution profiles of monodispersed particles and polydispersed particles under a sink condition. At the initial stage of dissolution, the dissolution rate increases as the particle becomes dispersed (cf. Fig. 3.7). However, at the final stage of dissolution, the dissolution rate becomes slower when compared to that of the monodispersed particles, as the small particles have already been vanished, whereas the large particles remain dissolved (Fig. 5.8).
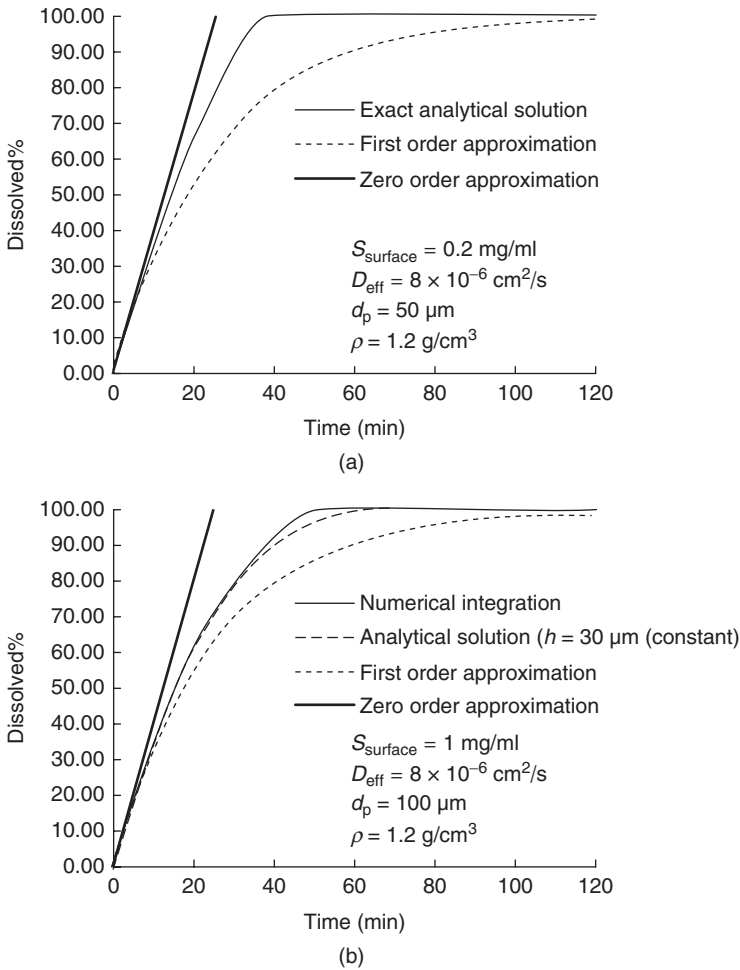
Figure 5.6 Comparison of numerical integration, analytical solution, and first-order approximation for dissolution simulation of monodispersed drug particles. (a) $d_{p,ini} <$ 60 μm and (b) $d_{p,ini} >$ 60 μm.

5.3.2   Fraction of a Dose Absorbed (Fa%)

The fraction of a dose absorbed (Fa%) is the ratio of the absorbed amount to the dosed amount. In this book, once drug molecules permeated the first biological barrier (e.g., apical membrane of the intestinal epithelial cells), the drug molecules were designated to be absorbed and Fa% is defined based on this definition. Usually, Fa% means the final Fa% after one dose of a drug passed through the GI tract.[5] However, Fa% is time dependent. For example, after dosing a drug,

[5] Similarly, the bioavailability (F or BA%) is usually the final value.
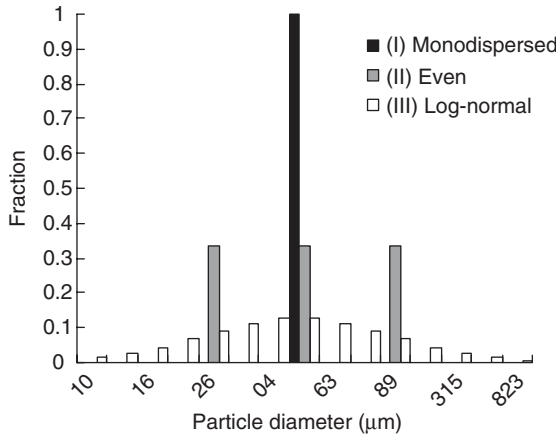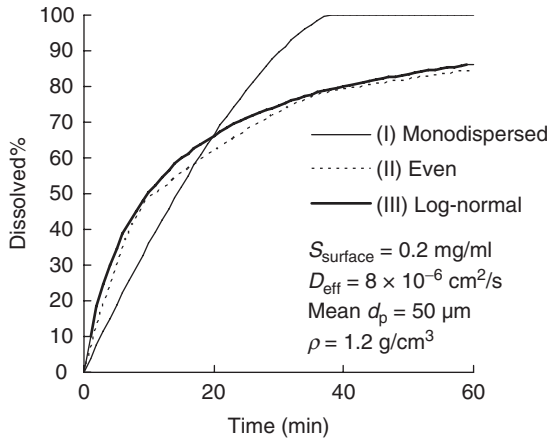
Figure 5.7 Dissolution of mono, 3 bins, and log-normal distribution particles. (a) Particle size distribution and (b) dissolution.

10% is absorbed until 1 h, 20% is absorbed until 2 h, and so on. Therefore, if the drug stays in the small intestine for infinite time, Fa% always becomes 100% regardless of the dissolution and permeation rates.

5.3.3 Approximate Fa% Analytical Solutions 1: Case-by-Case Solution

The central dogma of oral absorption consists of dissolution, nucleation, permeation, and GI transit, which are expressed as sequential differential equations. The derivations of some analytical solutions for Fa% are first discussed in this section. The numerical integration is then discussed in the next section.
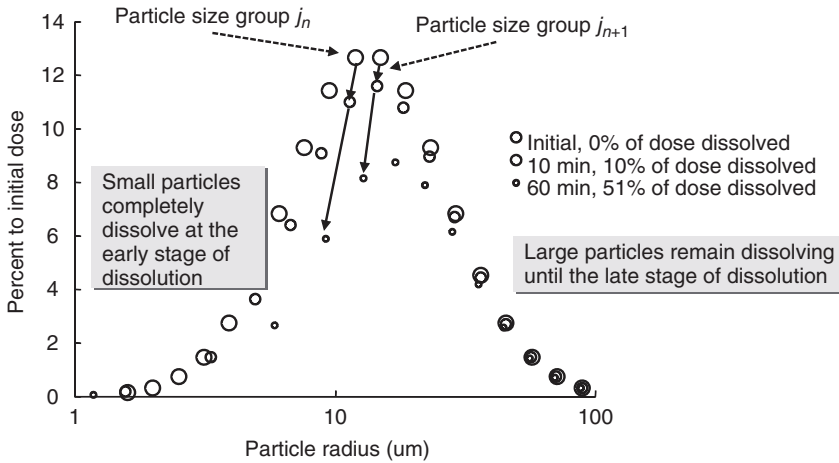
Figure 5.8   Particle size reduction during dissolution.

When the precipitation of a drug is not anticipated,[6] it is sufficient to consider dissolution, permeation, and GI transit. The one-compartment GI model (S0I1C0) can be used to derive approximate analytical solutions for Fa% calculation. When using the one-compartment GI model, Fa% can be calculated by solving the following sequence of differential equations from time $t = 0$ to $t = T_{si}$ (T_{si}: small intestine transit time).

$$\frac{dX_{API}}{dt} = -k_{diss}X_{API,t=0}^{1-a} X_{API}^{a} \left(1 - \frac{X_{dissolv}/V_{GI}}{S_{dissolv}} \right) \cdots (0 < a < 1) \quad (5.17)$$

$$\frac{dX_{dissov}}{dt} = -\frac{dX_{API}}{dt} - k_{perm} X_{dissolv} \quad (5.18)$$

$$\frac{dX_{perm}}{dt} = k_{perm} X_{dissolv} \quad (5.19)$$

As $X_{dissolv}$ appears in all equations, it is difficult to obtain an exact analytical solution for general cases.[7] First, approximate analytical solutions for three typical types of oral absorption, that is, the permeability-limited, dissolution-rate-limited, and solubility-permeability-limited cases are discussed (Section 1.2).

5.3.3.1 *Permeability-Limited Case.* When drug particles dissolve instantly and completely in the GI tract, the dissolution process becomes negligible and the

---

[6]Basically for undissociable and free acid drugs with a standard formulation.
[7]However, no existence of such an exact analytical solution has not been proved yet (so might exist but not found).

permeation process determines the Fa% of the drug. In this case, $X_{\text{dissolv}} = \text{Dose}$ at $t = 0$. Therefore, by solving Equation 5.19,

$$X_{\text{dissolv}} = \text{Dose} \cdot \exp(-k_{\text{perm}}T_{\text{si}}) \tag{5.20}$$

The fraction of the dissolved drug remaining unabsorbed at time T_{si} is then calculated as

$$\frac{X_{\text{dissolv}}}{\text{Dose}} = \exp(-k_{\text{perm}}T_{\text{si}}) \tag{5.21}$$

Considering the mass balance in the GI fluid, Fa for the permeability-limited cases (Fa_{PL}) is

$$\text{Fa}_{\text{PL}} = 1 - \frac{X_{\text{dissolv}}}{\text{Dose}} = \frac{X_{\text{perm}}}{\text{Dose}} = 1 - \exp(-k_{\text{perm}}T_{\text{si}}) = 1 - \exp(-\text{Pn}) \tag{5.22}$$

where X_{perm} is the permeated amount. As colonic absorption of drugs with low permeability is usually negligible ($< 20\%$), T_{si} can be set to the small intestine transit time. $k_{\text{perm}} \times T_{\text{si}}$ becomes a dimensionless number, the "permeation number (Pn)."[8,9] Even though this analytical solution is based on the one-compartment model, it is almost identical to the analytical solution for seven-compartment model [8] (Fig. 5.9) (Table 5.1).

$$\text{Fa}_{\text{PL}} = 1 - \exp(-k_{\text{perm}}T_{\text{si}}) \approx 1 - \left(1 + \frac{k_{\text{perm}}T_{\text{si}}}{7}\right)^{-7} \tag{5.23}$$

5.3.3.2 Solubility-Permeability-Limited Case.
In the solubility-permeability-limited case (SL), Fa can be calculated assuming that X_{dissolv} equals $S_{\text{dissolv}} \times V_{\text{GI}}$ and remains constant over time.

$$\frac{dX_{\text{dissolv}}}{dt} = -k_{\text{perm}}X_{\text{dissolv,const}} = -k_{\text{perm}}S_{\text{dissolv}}V_{\text{GI}} \tag{5.24}$$

(cf. $X_{\text{dissolv}} = C_{\text{dissolv}} \times V_{\text{GI}}$). By integrating this equation, the permeated amount until time T_{si} is calculated as

$$X_{\text{perm}} = 1 - X_{\text{dissolv}} = k_{\text{perm}}S_{\text{dissolv}}V_{\text{GI}}T_{\text{si}} \tag{5.25}$$

[8] As discussed later, dimensionless parameters of Do, Dn, and An ($= 1/2\text{Pn}$) were originally introduced using a plug flow model (Section 9.2). However, the derivation of these parameters using the plug flow model is difficult and its meaning is not explicitly understood from the derivation process. Therefore, in this section, the one-compartment model is used and these dimensionless parameters are discussed in a step-by-step manner.

[9] k_{perm} is basically a time-dependent value. But in most cases, k_{perm} is treated as a constant.
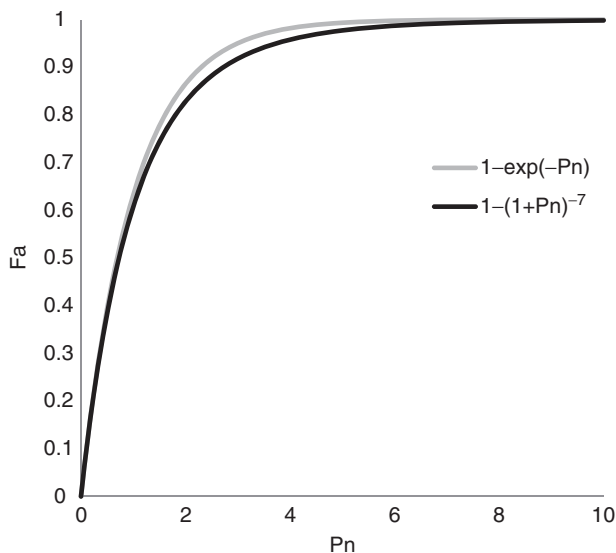
Figure 5.9 Analytical solutions for one- and seven-compartment models for a permeability-limited absorption case.

TABLE 5.1   Drug Range Used for the Investigation of Fa% Analytical Solution

Drug Parameter	Values
Dose (mg)	1, 3, 10, 30, 100, 300, 1000
$P_{eff}(\times 10^{-4} cm/s)$	0.03, 0.1, 0.3, 1, 3, 10
$D_{eff}(\times 10^{-6} cm^2/s)$	0.1, 0.3, 1, 3, 10
$S_{dissolv}$ (mg/ml)	0.001, 0.003, 0.01, 0.03, 0.1, 1
$d_p(= 2r_p)$ (μm)	1, 3, 10, 30, 100, 300

Therefore, Fa is calculated as

$$Fa_{SL} = \frac{X_{perm}}{Dose} = \frac{k_{perm}S_{dissolv}V_{GI}T_{si}}{Dose} = \frac{Pn}{Do}(\text{if } Fa > 1 \text{ then } Fa = 1) \qquad (5.26)$$

$$Do = \frac{Dose}{S_{dissolv}V_{GI}} \qquad (5.27)$$

As the colonic absorption of compounds with low solubility is usually negligible, T_{si} can be set to the small intestine transit time. As it is assumed that the dissolution rate is rapid and $C_{dissolv}$ immediately reaches $S_{dissolv}$ in this case,

Fa_{SL} is the theoretical maximum Fa value (except for supersaturable cases). Dose × Fa_{SL} is called the *maximum absorbable dose* (MAD) [21, 22].[10]

This Fa calculation is appropriate for undissociable and free acid drugs; however, it is not appropriate for free base compounds and the salts of acid and base drugs. In the latter cases, Fa% usually becomes significantly higher than Fa_{SL}. It should be emphasized that Fa_{PL} depends on k_{perm} and $S_{dissolv}$ (so it is called *solubility–permeability* limited).

The Do, which is the ratio of the dose to the maximum dissolved amount in the fluid is introduced in the Fa_{PL} equation. The Do is the most important dimensionless number that characterizes the biopharmaceutical profile of a drug.

5.3.3.3 *Dissolution-Rate-Limited Case.*

In the case of dissolution-rate-limited (DRL) absorption, the dissolved % equals Fa%. An approximate analytical solution can be obtained, assuming $C_{dissolv}$ equals 0 (the perfect sink condition) and first-order dissolution.

$$Fa_{DRL} = 1 - \exp(-k_{diss}T_{si}) = 1 - \exp(-Dn) \qquad (5.28)$$

where Dn is the dissolution number. As shown in Figure 5.6, the first-order approximation would be appropriate for many cases.

5.3.4 Approximate Fa% Analytical Solutions 2: Semi-General Equations

5.3.4.1 *Sequential First-Order Kinetics of Dissolution and Permeation.*

When Do < 1, the oral absorption of a drug can be represented as a sequential first-order process. In this case, an analytical solution for Fa (Fa_{sfo}) is

$$Fa_{sfo} = 1 - \frac{k_{perm}}{k_{perm} - k_{diss}} \exp(-k_{diss}T_{si}) + \frac{k_{diss}}{k_{perm} - k_{diss}} \exp(-k_{perm}T_{si})$$

$$= 1 - \frac{Pn}{Pn - Dn} \exp(-Dn) + \frac{Dn}{Pn - Dn} \exp(-Pn) \quad \frac{C_{dissolv}}{S_{dissolv}} < 1 \qquad (5.29)$$

Figure 5.10 shows the comparison of Fa_{sfo} and Fa numerically obtained with the S1I7C1 model (Fa_{NI}). Fa_{sfo} is only valid for Do < 1 cases. Fa_{sfo} resulted in overestimation of Fa in the case of compounds with low solubility (BCS class II and IV compounds) because of negligence of the effect of solubility limitation in the GI fluid. In the case of compounds with high solubility (BCS I and III, Do < 1), the correlation was appropriate. This is not surprising because the analytical solutions of permeation-limited cases for the S1I7C1 system are almost identical with that of the one-compartment model (Fig. 5.9). Even in the

[10]This calculation gives maximum achievable absorbed amount for undissociable compounds by increasing the dose or increasing the dissolution rate. However, for supersaturable cases such as a salt form API, supersaturated concentration could occur in the GI tract and Fa can exceed Fa_{SL}.
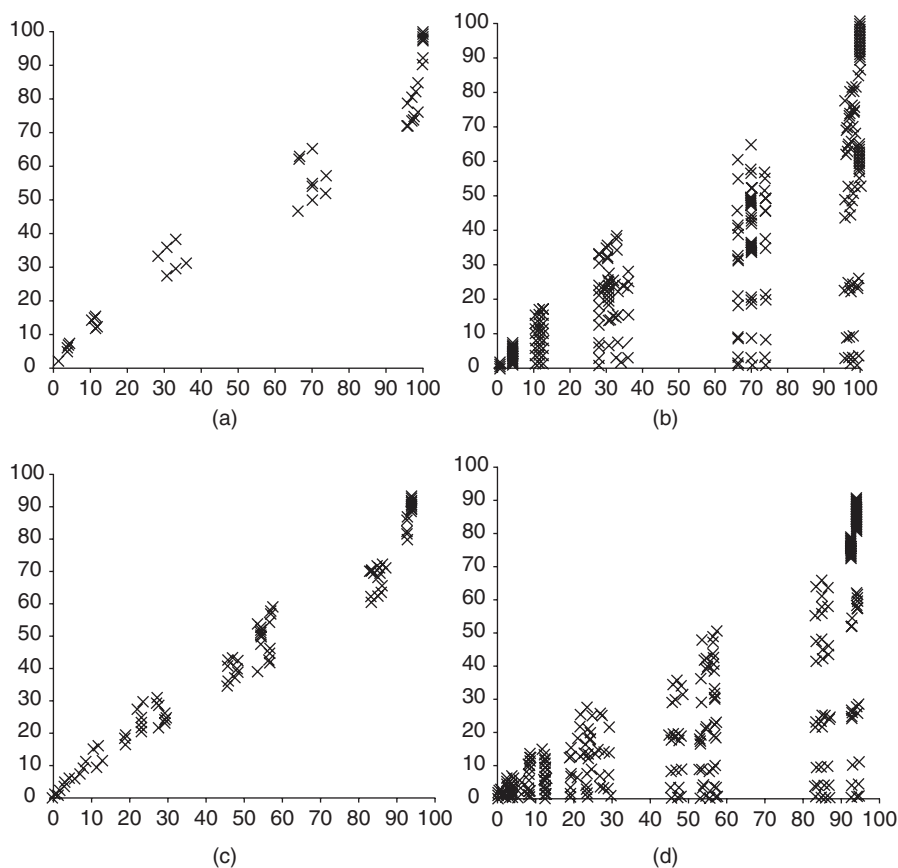
Figure 5.10 Fa calculated by sequential first-order approximation (Fa_{sfo}) versus numerical integration of the S1I7C1 system (Fa_{NI}). The ranges of the drug parameters are listed in Table 5.1. Panel a–d corresponds to BCS class I–IV, respectively.

case of BCS I, some compounds showed incomplete absorption because of a slow dissolution rate. A large particle size or a small diffusion coefficient can cause slow dissolution. As the permeabilies of BCS I drugs are high, oral absorption becomes dissolution rate limited and the first-order approximation is appropriate.

The GITA model is an extension of the sequential first-order kinetics to the seven-compartment model. Therefore, the GITA model should not be used for the solubility-permeability-limited cases.

5.3.4.2 Minimum Fa% Model. By taking the minimum Fa value[11] among the three rate-limiting cases (Fa_{PL}, Fa_{SL}, and Fa_{DRL}), we can obtain an approximate analytical solution for Fa ($Fa_{min\,limit}$). As shown in Figure 5.11, compared to Fa_{sfo}, the $Fa_{min\,limit}$ gives much closer results to Fa_{NI}, suggesting that the simplest

[11]Corresponds to the rate-limiting step approximation.
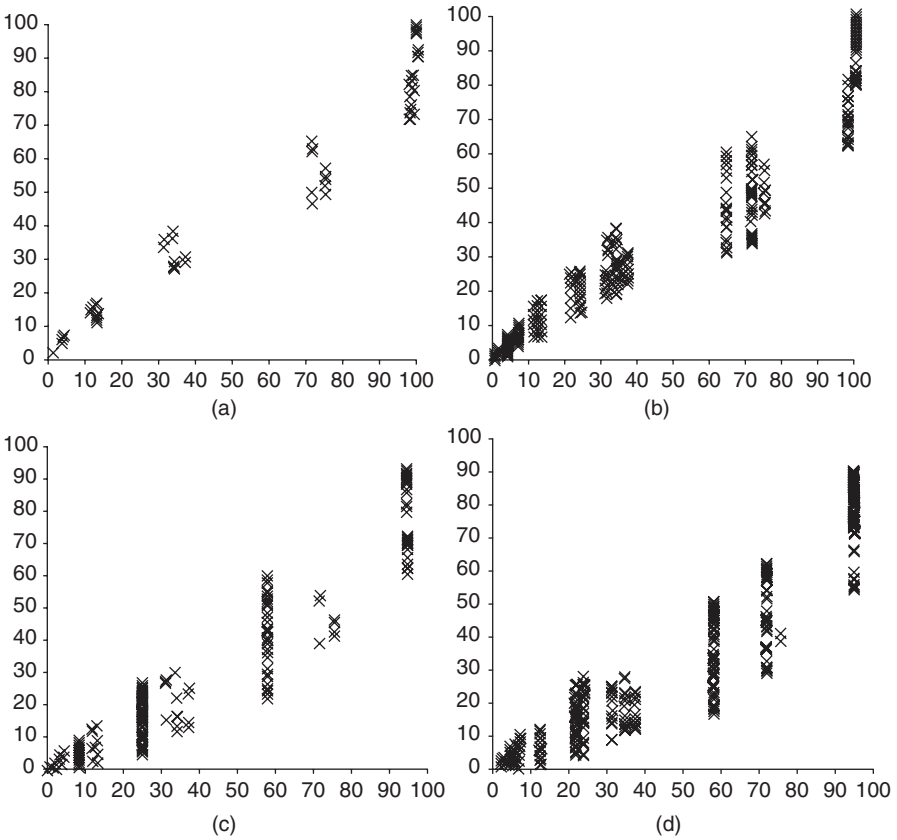
Figure 5.11   Fa calculated as the minimum value of limiting cases (Fa$_{min,limit}$) versus by numerical integration of the S1I7C1 system (Fa$_{NI}$). The ranges of the drug parameters are listed in Table 5.1.

Fa% calculation for each limiting case would be sufficient for most cases of drugs. However, for intermediate cases, the assumptions employed to derive the analytical solutions, that is, $X_{dissolv} = 0$ in Equation 5.29 for the dissolution-limited case or $C_{dissolv} = S_{dissolv}$ in Equation 5.26 for the solubility-permeability-limited case are not appropriate.

5.3.5   Approximate Fa% Analytical Solutions 3: Fa$_{SS}$ Equation

Recently, a general approximate Fa% analytical solution based on the steady state approximation ("Fa$_{SS}$ equation") was derived and compared with Fa$_{NI}$ [16, 23]. The Fa$_{SS}$ equation is simple; however, it still gives Fa% values similar to Fa$_{NI}$. To increase the transparency of calculation, the Fa$_{SS}$ equation should be used when it is appropriate.

5.3.5.1 *Application Range.* The Fa_{SS} equation is derived with assumptions that the stomach has little effect on Fa% and no supersaturation is induced during the oral absorption processes. Therefore, the Fa_{SS} equation is applicable for the following:

1. All BCS I and III drugs
2. BCS II and IV drugs that are
   (a) Undissociable
   (b) Free acid
   (c) Free base drugs dosed to the stomach with high pH.

5.3.5.2 *Derivation of Fa Number Equation.* To appropriately calculate the intermediate cases between the permeability, dissolution rate, and solubility-permeability-limited cases, it can be assumed that $X_{dissolv}$ becomes a steady value ($X_{dissolv,ss}$) when the dissolution rate and permeation rate balance. In the initial phase of oral absorption, $X_{API} \approx X_{API,t=0}(= Dose)$.[12] When we assume $S_{surface} = S_{dissolv}$ (valid for undissociable compounds and the low S_0 cases of dissociable compounds),

$$k_{diss}Dose\left(1 - \frac{X_{dissolv}/V_{GI}}{S_{dissolv}}\right) = k_{perm}X_{dissolv} \tag{5.30}$$

The left-hand side is the dissolution rate equation and the right-hand side is the permeation rate equation. These two equations are equaled because dissolve-in and permeate-out rates are balanced. By solving Equation 5.30 for $X_{dissolv,ss}$ at the initial time, normalizing by $S_{dissolv}$, and inserting into Equation 5.28, Fa with the steady state approximation (Fa_{SS}) can be calculated as [23]

$$Fa_{ss} = 1 - \exp\left(-\frac{1}{\frac{1}{k_{diss}} + \frac{Do}{k_{perm}}} \cdot T_{si}\right)$$

$$= 1 - \exp\left(-\frac{1}{\frac{1}{Dn} + \frac{Do}{Pn}}\right) \text{ If } Do < 1, Do = 1. \tag{5.31}$$

As limiting cases, Fa_{SS} smoothly connects to Fa_{PL}, Fa_{SL}, and Fa_{DRL} (cf. $x < 0.7$, $1 - \exp(x) \approx x$). The initial saturation number (Sn_{ini}), which indicates the degree of sink/nonsink conditions in the intestinal fluid, can be calculated as

$$Sn_{ini} = \frac{C_{dissolv,ss}}{S_{dissolv}} = \frac{1}{1 + \frac{k_{perm}}{Do \cdot k_{diss}}} = \frac{1}{1 + \frac{Pn}{Do \cdot Dn}} \quad Do > 1 \tag{5.32}$$

---

[12]More precisely, in the dissolution rate equation, the power on X_{API} is 1/3 for most cases. Therefore, we can approximate the dissolution process as zero-order kinetics (Fig. 5.6).
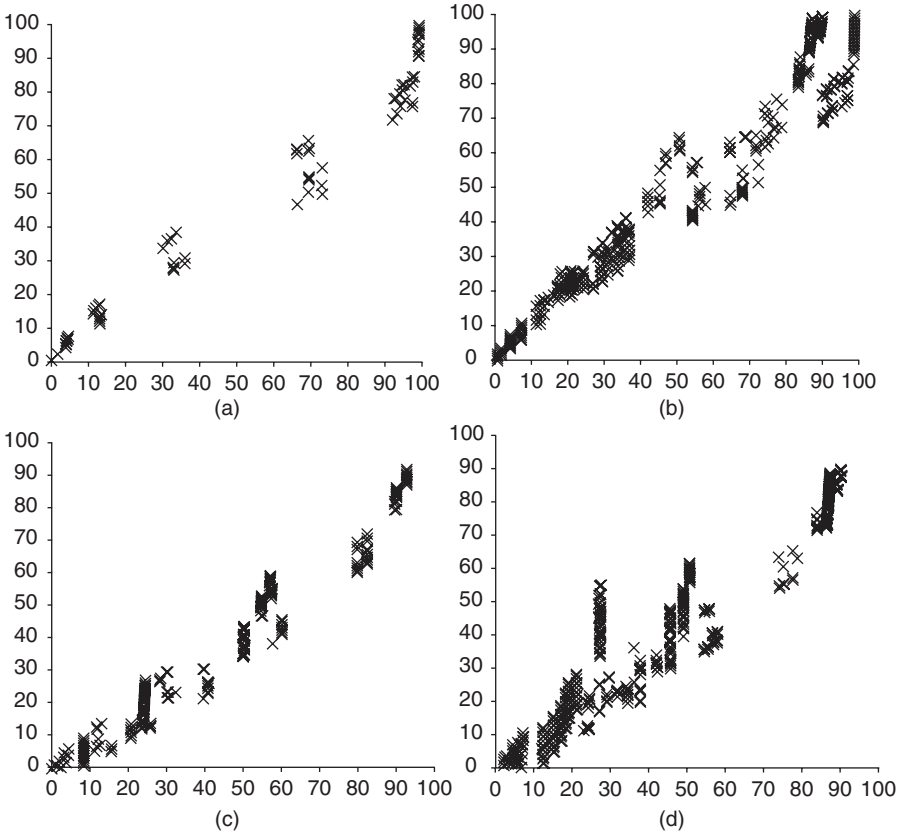
Figure 5.12 Fa calculated by the analytical solution with the steady state approximation (Fa_{SS}) versus by numerical integration of the S1I7C1 system (Fa_{NI}). The ranges of the drug parameters are listed in Table 5.1.

where $C_{dissolv,ss}$ is the steady state concentration in the intestinal fluid. When Sn_{ini} is close to 1, the drug concentration in the intestinal fluid is close to the saturated solubility, whereas when Sn_{ini} is close to 0, it is close to the sink condition.

As shown in Figure 5.12, even though the Fa_{SS} equation is simple, it gives Fa that is almost identical to Fa_{NI} that is calculated using a numerical integration of the S1I7C1 model.

5.3.5.3 *Refinement of the Fa_{SS} Equation.* Compared to Fa_{sfo} and $Fa_{min\,limit}$, the Fa_{SS} gives much closer results to Fa_{NI}. The remaining slight difference would be due to the steady state concentration assumption and the dispersion of particles along the GI tract. The following three deviation patterns were identified (Fig. 5.13):
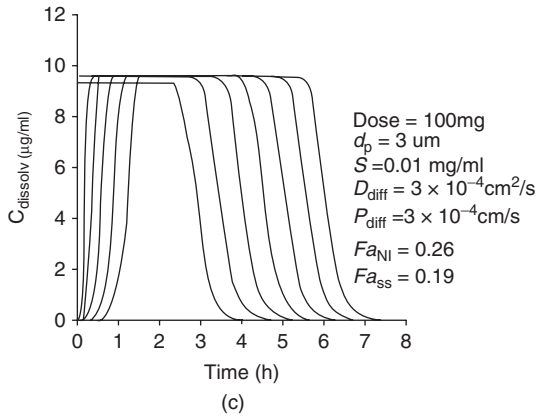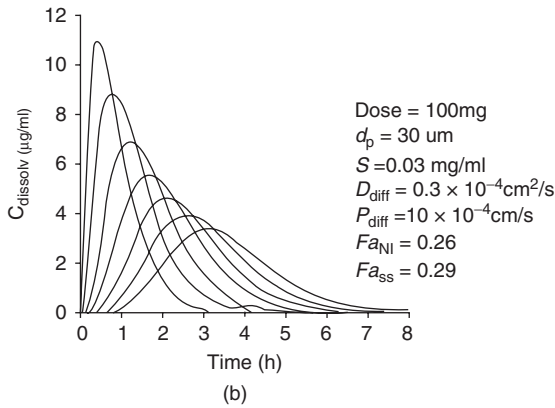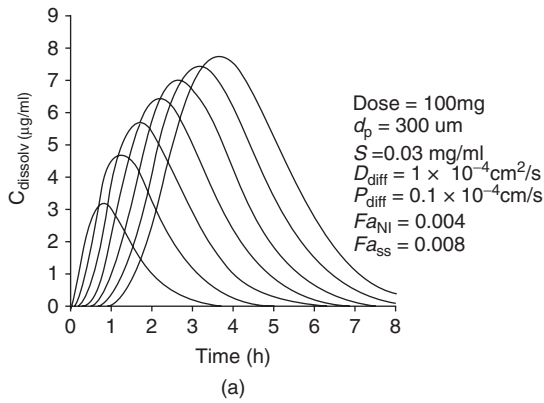
Figure 5.13 Typical case examples of deviation from the steady state approximation. (a) $C_{dissolv}$ does not reach the steady state during the GI transit, (b) the initial steady state concentration is not maintained, and (c) the steady state duration is longer than T_{si}. The drug parameters used for Fa calculation are indicated in the figures. The lines in the figure correspond to each small intestinal compartment (from the left to the right, compartment 1 to 7, proximal to distal, respectively).

(a) $C_{dissolv}$ does not reach the steady state during the GI transit

(b) The initial steady state concentration is not maintained because of the dissolution rate being reduced (particle size reduction occurred as particles dissolve)

(c) The steady state is maintained longer than T_{si} because of the particles remaining in the GI tract after T_{si} (remaining particle effect (RPE)).

Cases (a) and (b) are due to the steady state approximation, whereas case (c) is due to negligence of the dispersion of drug particles along the GI tract.

In the case of (a), $C_{dissolv} < S_{dissolv}$. Therefore, the sequential first-order kinetic model is appropriate. Appropriate Fa can be obtained by replacing Fa_{SS} with Fa_{sfo} when $Fa_{sfo} \times 1.15 < Fa_{ss}$. The coefficient 1.15 was introduced as a margin to ensure a definite sink condition. This treatment improved the correlation at Fa < 0.2 range.

To correct (b) and (c), the steady state reduction correction factor (CF_{SSR}) and the extended steady state duration number (Tn_{exss}) can be introduced as

$$Fa_{ss,corr} = 1 - \exp\left(-\frac{1}{\dfrac{1}{Dn} + \dfrac{Do}{Pn}} \cdot CF_{SSR} \cdot Tn_{exss}\right) \quad \text{If } Do < 1, Do = 1.$$

$$(5.33)$$

CF_{SSR} can be calculated considering the saturation number at time $T_{si}(Sn_{T_{si}})$. Fa is first calculated without any correction in Equation 5.31 (Fa'). Using Fa' to consider the reduction of Do and Dn during the oral absorption processes (i.e., replacing Do and Dn in Equation 5.31 with $Do(1 - Fa')$ and $Dn(1 - Fa')^{-2/3}$), and normalizing by Sn_{ini}, the steady state reduction number (SRn) can be obtained as (cf. $r_p/r_{p,t=0} \approx (1 - Fa')^{1/3}$, neglecting $X_{dissolv}$ at time T_{si}),

$$SRn = \frac{Sn_{T_{si}}}{Sn_{ini}} = \frac{1}{Sn_{ini}\left(1 + \dfrac{Pn}{Do \cdot Dn \cdot (1 - Fa')^{1/3}}\right)} \quad (5.34)$$

The mean and standard distribution of particle size are assumed to remain the same. CF_{SSR} is then calculated by taking the average as

$$CF_{SSR} = \frac{1}{2}(Sn_{ini} + Sn_{T_{si}}) = \frac{1}{2}Sn_{ini}(1 + SRn) \quad (5.35)$$

The CF_{SSR} corrects the declining of drug concentration from an initial steady state concentration. CF_{SSR} was found to be in the range of 0.54–1.0.

Tn_{exss} is determined by the amount of drug particles remaining in the GI tract. The portion of a drug exited from the small intestine until time t (EXT(t)) can
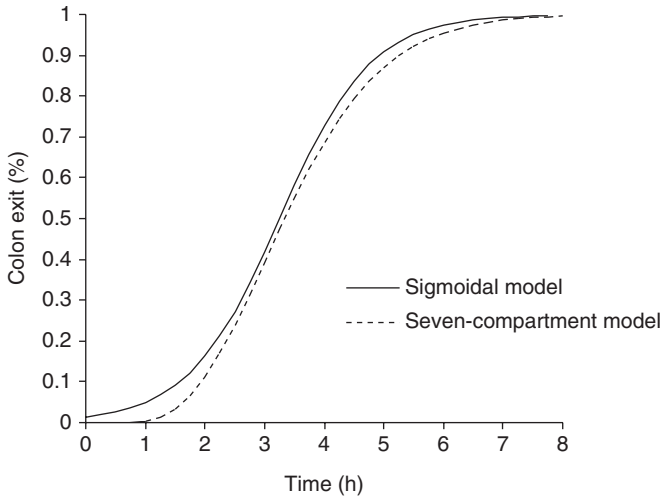
Figure 5.14 Colon exited fraction expressed by the sigmoidal curve (solid line) and the S1I7C1 system (dotted line). For the S1I7C1 system, $K_t = 7/T_{si} = 2$ (h^{-1}) and for the sigmoid curve, $k_t = 1.31$ (h^{-1}).

be expressed by the S1I7C1 model or a sigmoid curve as

$$EXT(t) = 1 - \exp(-K_t \cdot t) \left(\sum_{n=1}^{7} \frac{(K_t \cdot t)^{n-1}}{(n-1)!} \right) \approx \frac{1}{1 + \exp(-k_t(t - T_{si}))} \quad (5.36)$$

Figure 5.14 shows the analytical solution of the colon exited fraction by the S1I7C1 model (Eq. 5.36, middle part) and a sigmoid curve (Eq. 5.36, right-hand side, $k_t = 1.31$ h^{-1}). Using EXT(t) and approximation of Fa $\ll$ 1, the saturation number at T_{exss} can be calculated as

$$Sn_{T_{exss}} = \frac{1}{1 + \dfrac{Pn}{Do(1 - EXT(T_{exss})) \cdot Dn}} \quad (5.37)$$

$Do(1 - EXT(t))$ is the Do at time t considering the colon exit of the dosed drug particles. When $Sn_{T_{exss}}/Sn_{ini} < 1/2$, the particle number in the small intestine cannot maintain the steady state. Using a sigmoidal curve for EXT(t), rearranging $Sn_{T_{exss}}/Sn_{ini} = 1/2$ and normalizing by T_{si}, we obtain the Tn$_{exss}$:

$$Tn_{exss} = \frac{T_{exss}}{T_{si}} = 1 - \frac{1}{k_t \cdot T_{si}} \ln\left(\frac{1}{1 + \dfrac{Do \cdot Dn}{An}} \right) \qquad Do(1 - EXT(T_{exss})) > 1$$

$$(5.38)$$

The precondition of this equation is that $Do(1 - EXT(t))$ is larger than 1. The time at which the drug amount remains in the small intestine gives $Do(1 - EXT(t)) = 1(T_{Do1})$ and can be calculated by rearranging $Do(1 - EXT(T_{Do1})) = 1$ and normalizing with T_{si} as

$$Tn_{Do1} = \frac{T_{Do1}}{T_{si}} = 1 - \frac{1}{k_t \cdot T_{si}} \ln \left(\frac{1}{1 - \frac{1}{Do}} - 1 \right) \tag{5.39}$$

When $Tn_{Do1} > Tn_{exss}$, Tn_{exss} is replaced with Tn_{Do1}. Tn_{exss} was found to be in the range of $1.0-2.8$.

The correlation between Fa_{SS} and Fa_{NI} was improved by applying Fa_{sfo}, CF_{SSR}, and Tn_{exss} (Fig. 5.15). The remaining deviations may be due to the approximation employed in the correction factors and the dispersion of drug
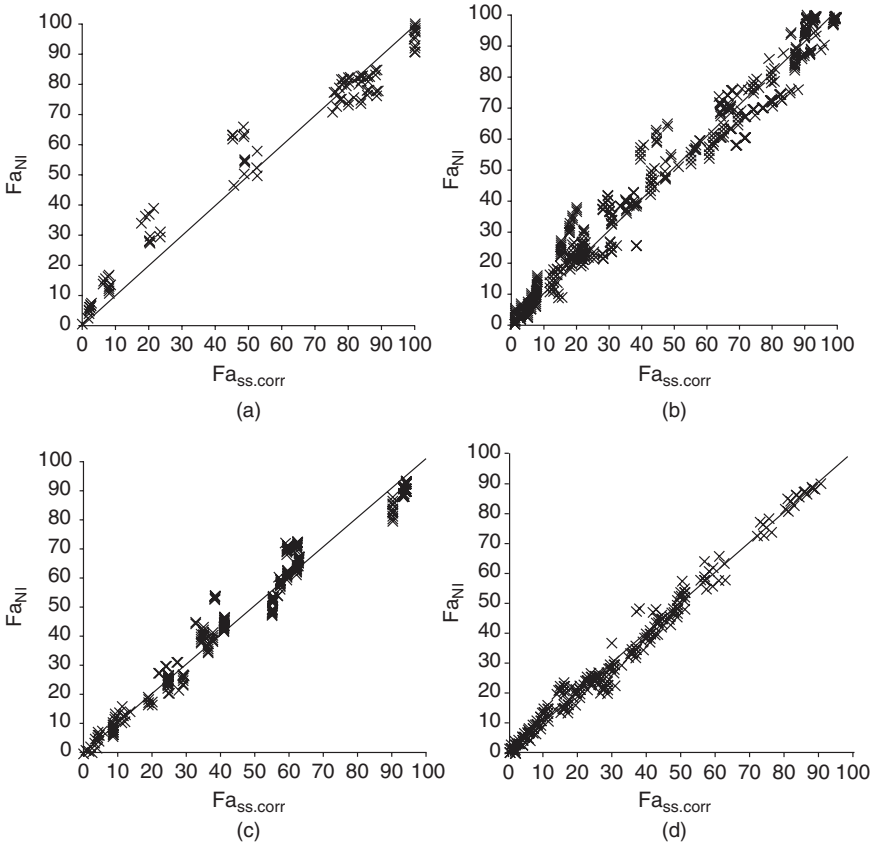

Figure 5.15 Fa calculated by corrected steady state approximation ($Fa_{SS\ corr}$) versus numerical integration of the S1I7C1 system (Fa_{NI}). (a) BCS I, (b) BCS II, (c) BCS III, and (d) BCS IV. The ranges of the drug parameters are listed in Table 5.1.

particles and dissolved drug in the small intestine, which are represented by the S1I7C1 model but not by the S0I1C0 model.

5.3.5.4 *Advantage of Fa$_{SS}$ Equation.* Considering the convenience and clarity of the Fa$_{SS}$ equation and that many compounds with low solubility are undissociable, Fa$_{SS}$ would be beneficial for practical drug discovery uses. Figure 5.12 suggests that the difference of the GI transit models (S0I1C0 vs S1I7C1) and integration method (approximate analytical vs numerical) has little effect on Fa% prediction. Sn can be used to indicate whether the oral absorption of the drug is dissolution limited (sink condition) or solubility–permeability limited.

Fa$_{SS}$ calculation is simple, easy, and available for everybody, whereas the S1I7CX model is difficult to calculate (need programing skill). The commercial software is not available as an open source. As scientific publications should be thoroughly validated by independent readers, Fa$_{SS}$ will be important as a transparent and traceable model.

5.3.5.5 *Limitation of Fa$_{SS}$ Equation.* It should be noted that Fa$_{SS}$ has several conditions for applicable drugs, that is, only applicable for undissociable drugs and free acidic compounds (and basic drugs dosed in a high stomach pH condition). Fa$_{SS}$ cannot handle the dynamic change of physiology along with the GI tract. It does not provide a sufficient accuracy (such as $\pm 20\%$) to be used for drug development.[13]

5.3.6 Interpretations of Fa Equations

The interpretation of analytical solutions is critically important when we think of the problems of oral absorption. The three categories discussed in the introduction section (Section 1.2) are based on this theoretical analysis. Table 5.2 shows the criteria for the three categories.

In the equations for the permeability-limited case (Fa$_{PL}$), the dose and particle size do not appear in the equation, suggesting that Fa does not depend on these

TABLE 5.2 Criteria to Diagnose the Regime of Oral Drug Absorption

Oral Absorption Category	Criteria	Fa
Dissolution rate limited (DRL)	Dn < Pn/Do (If Do < 1, Dn < Pn)	$1 - \exp(-Dn)$
Permeability limited (PL)	Do < 1, Pn < Dn	$1 - \exp(-Pn)$
Solubility-epithelial membrane permeability limited (SL-E)	Do > 1, Pn/Do < Dn, $P'_{ep} < P_{UWL}$	Pn/Do
Solubility-UWL permeability limited (SL-U)	Do > 1, Pn/Do < Dn, $P'_{ep} > P_{UWL}$	Pn/Do

[13]This does not mean that more complicated compartment models such as the S1I7C3 system can give this accuracy. Technically, a more complex model might have an ability to express the complexity of the oral absorption of a drug. However, given the uncertainty in the physiological and drug parameters, as well as the variations in the *in vivo* data, it is difficult to prove the superiority of more complicated systems over a simpler model. The Occam's razor principle should be considered.

parameters. Similarly, in the case of the dissolution-rate-limited case (Fa$_{DRL}$), the dose does not appear in the equation, whereas the particle size does (cf. $k_{diss} = 3D_{eff}S_{dissolv}/\rho_p r_{p,ini}^2$), suggesting that the dose strength does not affect Fa, whereas the particle size does. In the case of the solubility-permeability-limited case (Fa$_{SL}$), the dose and permeability appear in the equation, whereas particle size does not, suggesting that the dose and permeability[14,15] affect Fa, whereas the particle size does not.

5.3.7 Approximate Analytical Solution for Oral PK Model

The one-compartment first-order oral PK model is often used to analyze the PK profile. From Equation 5.31,

$$k_{abs} = \frac{1}{k_{diss}} + \frac{Do}{k_{perm}} \quad \text{If Do} < 1, \text{Do} = 1 \tag{5.40}$$

$$C_p(t) = \frac{Dose \cdot Fg \cdot Fh}{Vd} \cdot \frac{k_{abs}}{k_{abs} - k_{el}} (\exp(-k_{el}t) - \exp(-k_{abs}t)) t < T_{si} \tag{5.41}$$

$$C_p(t) = C_p(T_{si}) \exp(-k_{el}(t - T_{si})) \qquad t > T_{si} \tag{5.42}$$

Equations 5.41 and 5.42 are different from the most often used equation, as Fg Fh is used in the pre-exponential factor instead of F (Fig. 5.16).

5.4 INTEGRATION 2: NUMERICAL INTEGRATION

As discussed earlier, the approximate analytical solution based on the one-compartment GI model is simple, easy to understand, and practically useful for many cases. However, this simple model cannot be used when the effect of the stomach and the colon is not negligible.

For appropriate biopharmaceutical modeling, the GI tract should be divided into at least three compartments, the stomach, the small intestine and the colon, to reflect the significant difference of physiological conditions in these sections. Numerical integration is required to simulate the dynamic change of $C_{dissolv}$ and the regional differences of P_{eff} and $S_{dissolv}$ in the GI tract. In this section, the mathematical treatment to perform numerical integration using multicompartment model is discussed.

---

[14]It is sometimes misunderstood that the permeability of a drug does not affect Fa% in the case of solubility-permeability-limited cases. It is obvious from the analytical solution that the permeability does affect Fa%.

[15]Except in the SL-U cases with high dose (>5 mg/kg) and small particle size (<10 μm). In these cases, the particle drifting effect may increase P_{eff}.
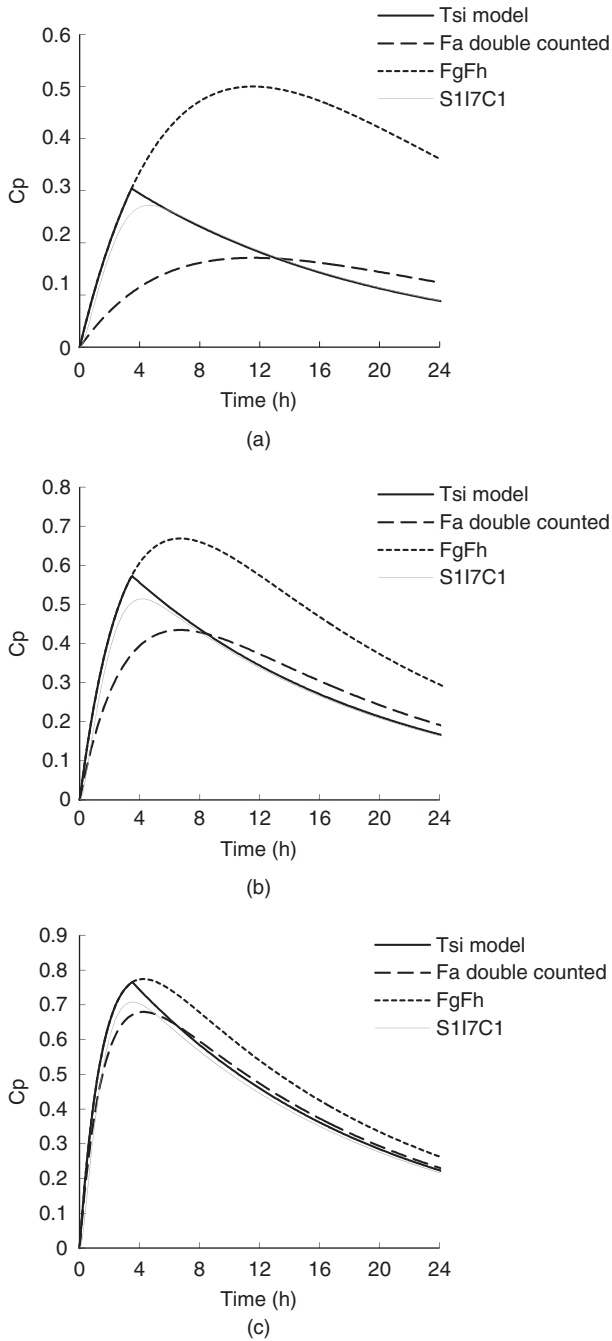
(a)

(b)

(c)

Figure 5.16 Comparison of Equations 5.41 and 5.42 (Tsi model) with the one-compartment model widely used in the literature (Fa double counted or Fa = 1 assumption (i.e., F = 1 × FgFh)), and numerical solution with the S1I7C1 model. (a) Fa = 0.34, (b) Fa = 0.65, and (c) Fa = 0.88.

5.4.1   Virtual Particle Bins

The use of virtual particle bins (VPBs) is the characteristic technical feature of computational biopharmaceutical modeling.

As discussed in Section 3.2.3, to represent the particle size distribution of API particles, a particle size bin (PSB) is assigned to each particle size. Furthermore, to represent the movement of each particle in the GI tract and the particle size reduction accompanied with dissolution, a PSB has to be further divided into VPBs. If the particle size distribution is represented by 20 PSBs and 100 VPBs are assigned to each PSB, a total of 2000 particle bins are required. As each particle group has one differential equation for dissolution, 2000 differential equations are required. However, with today's high speed computers, this number is not an issue. PSB and VPB also serves as the particle identification number.

Similarly, a PSB and a VPB can be assigned to the particles of newly formed API via nucleation (nuclei) as it is generated.

Each particle bin is associated with the data of its particle size, particle number, and the position of the particle in the GI tract (GI position: GIP). The physiological conditions that the VPB experiences, such as pH, bile-micelle concentration, and agitation strength, are used in the dissolution equation of each VPB.

$$\text{GIP(VPB)} = k, \quad k = \text{position in the GI tract} \tag{5.43}$$

$$\frac{dX_{\text{API(PSB,VPB)}}}{dt} = f\left(\text{pH}_{\text{GIP(VPB)}}, C_{\text{bile,GPI(VPB)}}, \varepsilon_{\text{GIP(VPB)}}, r_{\text{p(PSB,VPB)}},\right.$$

$$\left. N_{\text{API(PSB,VPB)}}, \text{others}\right) \tag{5.44}$$

5.4.2   The Mass Balance of Dissolved Drug Amount in Each GI Position

The mass balance of the dissolved drug in the GI fluid at a GI position (subscript k) can be expressed as

$$\frac{dX_{\text{dissolv},k}}{dt} = (K_{t,k-1} \cdot X_{\text{dissolv},k-1} - K_{t,k} \cdot X_{\text{dissolv},k})$$

$$+ \left(\sum_{\text{if GIP(PSB,VPB)}=k} \frac{dX_{\text{API(PSB,VPB)}}}{dt} + \sum_{\text{if GIP(PSB,VPB)}=k} \frac{dX_{\text{NFP(PSB,VPB)}}}{dt} \right)$$

$$- \frac{dX_{\text{perm},k}}{dt} \tag{5.45}$$

where $X_{\text{dissolv},k}$ is the dissolved drug amount at a position k (a compartment). The first parenthesis represents the flow-in of dissolved drug from the previous position and flow-out into the next position. The second parenthesis represents the dissolution and growth of both the dosed API particles (X_{API}) and the newly

formed precipitant particles (X_{NFP}). The dissolved (or precipitated) amount from a VPB is added to $X_{\text{dissolv},k}$ of the position where the particle bin is existing (i.e., GIP(VPB)). The last term represents the absorption of the dissolved drug molecules into the body. GIP represents the GI position of a particle bin at time t.

5.4.3   Controlled Release of Virtual Particle Bin

Biopharmaceutical modeling plays an important role in controlled release (CR) formulation development (Section 11.8). The development strategy of the CR formulation and the practical use of biopharmaceutical modeling are discussed in Section 11.8 in detail. Therefore, this section focuses on the computational algorithms to handle CR simulation.

CR can be categorized as prolonged release, timed release, and stimuli-triggered release. The release profile can simply be modeled by coupling a conditional binary function for each VPB with the dissolution equation.

$$CR(j) = (0 \text{ or } 1) \tag{5.46}$$

The binary function can be written by "if–then" syntax in the program. For pH triggered release,

"If pH(GIP(VPB)) < 5.5 then CR(VPB) = 1, else CR(VPB) = 0"

Similarly, for the GI position-specific release (such as colon targeting),

"If GIP(VPB) > 9 then CR(VPB) = 1, else CR(VPB) = 0"

For timed release,

"If t > 2 h then CR(VPB) = 1, else CR(VPB) = 0"

This can be expanded to any time-scheduled CR, for example, zero-order release and Weibull functional release.

Usually, the CR formulation is formulated as pellets, a tablet, or a capsule. The gastric empting patterns for these formulations are different from that of small particles (<0.5 mm) and depends on the MMC (Section 6.2). A timed gastric empting with the MMC phase III can be programmed by assigning the dosing timing during the MMC cycle (Section 5.2.1).

5.5   *IN VIVO* FA FROM PK DATA

Clinical Fa% data are required to validate biopharmaceutical modeling. However, there is no absolute method to obtain clinical Fa% from the clinical PK data. Usually, we have to put one or a few assumptions to calculate clinical Fa%. Therefore, it is preferable to compare the Fa% values if two or more methods are available.

5.5.1   Absolute Bioavailability and Fa

Absolute bioavailability (F or BA%) can be obtained from AUC ratio of i.v. and the other route (e.g., oral). Normalization by dose strength is often used assuming a linear PK profile. To avoid the effect of nonlinearity, the C_p levels from the i.v. and the other route should be set similar.

$$F = \frac{\text{AUC}_{\text{other}}/\text{Dose}_{\text{other}}}{\text{AUC}_{\text{i.v.}}/\text{Dose}_{\text{i.v.}}} \tag{5.47}$$

In the case of oral absorption, F is a composite parameter of the fraction of a dose absorbed (Fa), the fraction not metabolized in the gut wall (Fg), and the fraction not metabolized in the liver (Fh).

$$F = \text{Fa} \cdot \text{Fg} \cdot \text{Fh} \tag{5.48}$$

Therefore, to calculate Fa from F, Fh and Fg data are required. Fg can be roughly estimated from *in vitro* data or $\text{CL}_{\text{h,int}}$ (for CYP3A4 substrates) (Section 4.10). Fh can be calculated from the total clearance and urinary excretion percent (Ur%) after i.v. administration (assuming only the liver and kidney contribute the clearance).

$$\text{Fh} = 1 - \frac{\text{CL}_{\text{tot}}(1 - \text{Ur})}{Q_h} \tag{5.49}$$

This method is often used to estimate Fa% from i.v. and p.o. data. However, this method has some deviation from the authentic Fa% data obtained using radio-labeled drug [24].

5.5.2   Relative Bioavailability Between Solid and Solution Formulations

Relative bioavailability of a solid formulation against a solution formulation can be used as a surrogate for Fa% in the case of BCS class II drugs. As a BCS class II drug has a high permeability, Fa% would be 100% after solution administration.[16] High permeability can be assessed by *in vitro* membrane permeation assays (e.g., Caco-2) or simply from log P_{oct}, MW, and pK_a. Fa% can be calculated as the ratio of AUCs from a solid dosage form to a solution dosage form ($\text{AUC}_{\text{solid formulation}}$ and $\text{AUC}_{\text{solution}}$, respectively).

$$\text{Fa} = \frac{\text{AUC}_{\text{solid formlation}}}{\text{AUC}_{\text{solution}}} \tag{5.50}$$

---

[16]Absence of precipitation should be assessed by *in vitro* experiments using a biorelevant media.

In this equation, the effect of Fg and Fh on AUC is cancelled out. Therefore, Fa% obtained by this method is free from the uncertainty in these parameters.[17]

When the Do in the fed state is less than 1 (and dissolution is rapid), the AUC in the fed state can be used as a surrogate for $\text{AUC}_{\text{solution}}$. If the food has little or no effect on the AUC of a drug from a solubility-enhancing formulation such as emulsion and solid dispersion, it is highly probable that Fa% from the formulation is nearly 100%.

5.5.3   Relative Bioavailability Between Low and High Dose

In preclinical and clinical studies, a dose escalation study is usually performed. In many cases, at lower doses, the Do is less than 1 (or dosed as a solution formulation). If we assume that clearance and volume of distribution (V_{d}) of the drug is concentration independent, we can use this data to calculate Fa% for high permeability cases. In many cases, it is unlikely that the V_{d} becomes concentration dependent (except the case there is specific systemic binding site). However, CL could be concentration dependent especially at an extremely high dose. From the elimination half-life (k_{el}), the change in clearance can be estimated. By assuming V_{d} being constant, Fa can be calculated as [25]

$$\text{Fa} = \frac{\text{AUC}_{\text{high dose}} \cdot \text{CL}_{\text{high dose}}}{\text{AUC}_{\text{low dose}} \cdot \text{CL}_{\text{low dose}}} \cdot \frac{\text{Dose}_{\text{low}}}{\text{Dose}_{\text{high}}} = \frac{\text{AUC}_{\text{high dose}} \cdot k_{\text{el,high dose}}}{\text{AUC}_{\text{low}} \cdot k_{\text{el,low dose}}} \cdot \frac{\text{Dose}_{\text{low}}}{\text{Dose}_{\text{high}}}$$

$$(5.51)$$

where the subscripts high and low indicate the parameters obtained at high and low dose strengths, respectively.

5.5.4   Convolution and Deconvolution

Deconvolution is often used to calculate F as a time course function (i.e., $F(t)$), typically from i.v. and p.o. data. Various commercial programs as well as free programs are available to perform deconvolution. The Loo–Riegelman, Nelson–Wagner, and numerical deconvolution methods are most widely used. In many textbooks, the convolution equation is given as trivial, and the deconvolution is explained via Laplace transformation. However, the concept of convolution is actually not trivial and Laplace transformation is not easy to understand. In this section, the concept of convolution and deconvolution is briefly discussed in an illustrative manner. To enhance the understanding of the concept, the mathematical expression is simplified. The readers should refer to the original publication for accurate equations [26–29].

---

[17] Assessment of high/low permeability category by Caco-2 is more reliable than Fh and Fg estimation (so it is used even for the regulatory purposes).
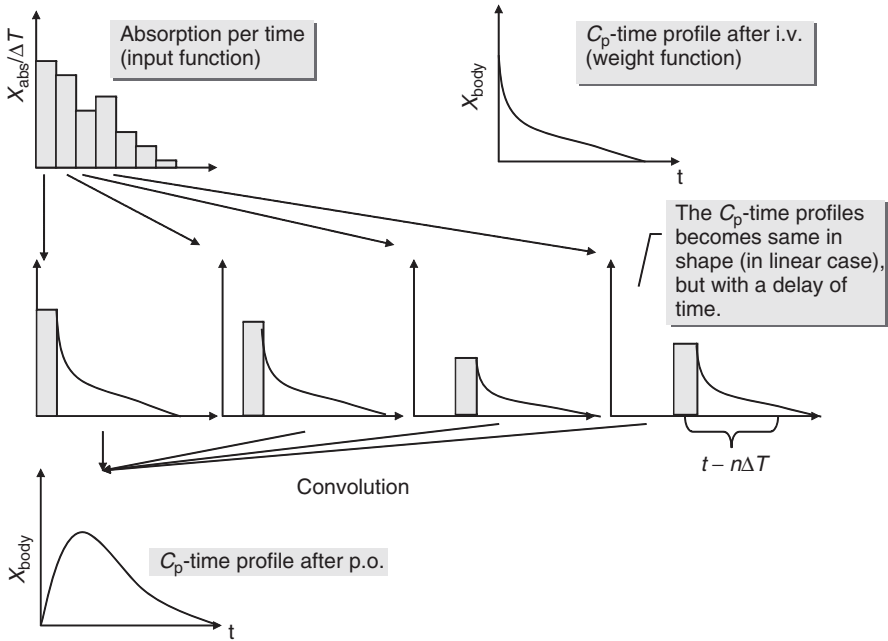
Figure 5.17   Schematic explanation of the convolution process.

5.5.4.1   Convolution. When the pharmacokinetics in the body is linear, the plasma concentration at time t after oral administration ($C_{p,p.o.}(t)$) can be written as convolution of input function (F) and weight function ($C_{p,i.v.}(t)$).

$$C_{p,p.o.}(t) = \frac{\text{Dose}_{p.o.}}{\text{Dose}_{i.v.}} \int_0^t F(\tau) C_{p,i.v.}(t - \tau)\, d\tau \qquad (5.52)$$

Figure 5.17 shows the schematic explanation of this convolution process. Equation 5.52 can be derived as follows. The oral absorption of a drug can be treated as the series of impulse inputs into the body. After an impulse input from the intestine, the elimination time course of the drug follows the same pattern as that of i.v. administration. The C_p time profile after ith impulse is

$$C_{p,p.o.,i}(t) V_d = \text{Dose}_{p.o.} F(i) \frac{C_{p,i.v.}(t - i\,\Delta T)}{C_{p,i.v.}(0)} \qquad (5.53)$$

where $\text{Dose}_{p.o.} F(i)$ represents the fraction of a dose input to the body by the ith impulse.

By integrating this equation,

$$V_d \sum_0^i C_{p,p.o.,i}(t - i\,\Delta T) = \frac{\text{Dose}_{p.o.}}{C_{p,i.v.}(0)} \sum_0^i F(i) C_{p,i.v.}(t - i\,\Delta T) \qquad (5.54)$$

As the plasma concentration after oral administration is the sum of the plasma concentration from the series of impulse inputs,[18] the plasma concentration at time t can be expressed as

$$C_{\text{p,p.o.}}(t) = \sum_{0}^{n} C_{\text{p,p.o.},i}(t - n\Delta T) \tag{5.55}$$

Therefore,

$$C_{\text{p,p.o.}}(t) = \frac{\text{Dose}_{\text{p.o.}}}{\text{Dose}_{\text{i.v.}}} \sum_{0}^{n} F(n) C_{\text{p,i.v.}}(t - n\Delta T) \tag{5.56}$$

$$\text{Dose}_{\text{i.v.}} = V_d C_{\text{p,i.v.}}(0) \tag{5.57}$$

By taking the limit, $i \to d\infty$, $\Delta T \to 0$, Equation 5.56 becomes Equation 5.52.

5.5.4.2 *Deconvolution.* The concept of deconvolution can be understood considering the mass balance of the drug amount in the body. When a C_p time profile is expressed by the one-compartment model and k_{el} and V_d are known from the i.v. data, the mass balance of the drug amount in the body at time t can be written as

$$V_d \frac{dC_p}{dt} = \frac{dX_{\text{abs}}}{dt} - k_{\text{el}} C_p V_d \tag{5.58}$$

By rearranging this equation,

$$\frac{dX_{\text{abs}}}{dt} = V_d \frac{dC_p}{dt} + k_{\text{el}} C_p V_d \tag{5.59}$$

Table 5.3 explains the stepwise deconvolution process based on this equation. In the first 1 min, the drug amount in the body (X_{body}) increased from 0 to 0.0198. At time $t = 0$ min, the elimination rate is 0. Therefore, the absorbed amount from 0 to 1 min is 0.0198. In the next 1 min, the net increase of X_{body} (left-hand side of Equation 5.58) can be calculated from the C_p time profile (In Table 5.3, it is 0.0192 (from 0.0198 to 0.0390). At time 1 min, the elimination rate is 0.0000988 ($= k_{\text{el}} \times C_p \times V_d$). Therefore, the drug amount supplied from the intestine into the plasma (dX_{abs}/t) is $0.0192 + 0.0000988$.

Another simple approach to understand the deconvolution would be reversing the convolution process by the stair case method [30]. As discussed in the convolution cases, the drug absorption from the intestine is represented as a series

---

[18]This is from the assumption of linear PK.

TABLE 5.3 Stepwise Deconvolution Process

Time, min	Observed C_p C_p (p.o.)	Deconvolution process			
		(1) $V_d \times dC_p$	(2) $k_{el} \times V_d \times C_p$	(1) + (2)	Fa (Deconvolution)
0	0.0000 (A)	0.0198 (C) = $V_d \times$ ((B) − (A))	0.0000 (D) = $V_d \times$ (A) $\times k_{el}$	0.0198(E) = (C)+ (D)	0.0198 (F)
1	0.0198 (B)	0.0193(H) = $V_d \times$ ((G) − (B))	0.0001(I) = $V_d \times$ (B) $\times k_{el}$	0.0194(J) = (H) + (I)	0.0391(K) = (F) + (J)
2	0.0390 (G)	0.0188(M) = $V_d \times$ ((L) − (G))	0.0002(N) = $V_d \times$ (G) $\times k_{el}$	0.0190 (O) = (M) + (N)	0.0581 (P) = (K) + (O)
3	0.0578 (L)	0.0183	0.0003	0.0186	0.0767

$k_{el} = 0.005, V_d = 1.$

of impulse input. To simplify the equation, the nth pulse input ($I(n)$) and $C_{p,i.v.}$ ratio at time t against time 0 are defined as

$$A(n) \equiv \frac{C_{p,i.v.}(n\Delta T)}{C_{p,i.v.}(0)}$$

$$I(n) \equiv \text{Dose}_{p.o.}(F(n\Delta T) - F((n-1)\Delta T)) \qquad (5.60)$$

The drug amount in the body at time $t = n\Delta T$ then becomes

$$X_{body}((n+1)\Delta T) = I(1)A(n+1) + I(2)A(n)$$
$$+ \cdots + I(n-1)A(1) + I(n)A(0) \qquad (5.61)$$

By rearranging this equation,

$$I(n) = \frac{X_{body,p.o.}((n+1)\Delta T) - (I(1)A(n+1) + I(2)A(n-1))}{+ \cdots + I(n-2)A(2) + I(n-1)A(1))}{A(0)} \qquad (5.62)$$

This is the reverse process of convolution. Starting with $n = 0$, $I(n)$ can be calculated in a step-by-step manner. In the stair case method, the i.v. pharmacokinetics is not model dependent and does not have to assume first-order kinetics. In reality, the experimental sampling time point is not equally distributed. Therefore, the time points between the experimental sampling time points have to be interpolated.

5.6   OTHER ADMINISTRATION ROUTES

5.6.1   Skin

In the case of skin permeation, the permeability coefficient can be described by the solubility–diffusion model, so that by the partition coefficient and the diffusion coefficient of a drug in the permeation barrier. Drugs permeate through the intercellular part of the stratum corneum (SC) that is mainly consist of ceramide (CER), cholesterol (CHO), and free fatty acid (FFA). These components organize a lamellar structure (cf. Fig. 6.28, the brick and mortar model). The octanol/water partition coefficient is most often used as a surrogate for the partition coefficient into the SC (K_{sc}) [31–33]. K_{sc} can be calculated as

$$\log K_{sc} = -0.024 + 0.59 \log P_{oct} \qquad (5.63)$$

The regression coefficient of $\log P_{oct}$ was 0.59, indicating that the skin membrane permeation barrier is more polar than octanol or a partial desolvation of the solute caused by the water associated with the ceramide polar head group. The

diffusion coefficient was found to decrease as the molecular weight and/or the hydrogen bond acidity/basicity increase. This finding is consistent with diffusion along a nonpolar pathway hindered by interaction with the immobilized polar head groups of the SC lipids.

REFERENCES

1. Takano, R., Sugano, K., Higashida, A., Hayashi, Y., Machida, M., Aso, Y., Yamashita, S. (2006). Oral absorption of poorly water-soluble drugs: computer simulation of fraction absorbed in humans from a miniscale dissolution test. *Pharm. Res*., 23, 1144–1156.

2. Takano, R., Furumoto, K., Shiraki, K., Takata, N., Hayashi, Y., Aso, Y., Yamashita, S. (2008). Rate-limiting steps of oral absorption for poorly water-soluble drugs in dogs; prediction from a miniscale dissolution test and a physiologically-based computer simulation. *Pharm. Res*., 25, 2334–2344.

3. Takano, R., Takata, N., Saitoh, R., Furumoto, K., Higo, S., Hayashi, Y., Machida, M., Aso, Y., Yamashita, S. (2010). Quantitative analysis of the effect of supersaturation on *in vivo* drug absorption. *Mol. Pharmaceutics*, 7, 1431–1440.

4. Sugano, K. (2011). Fraction of a dose absorbed estimation for structurally diverse low solubility compounds. *Int. J. Pharm*., 405, 79–89.

5. Dressman, J.B., Fleisher, D. (1986). Mixing-tank model for predicting dissolution rate control or oral absorption. *J. Pharm. Sci*., 75, 109–116.

6. Johnson, K.C. (2003). Dissolution and absorption modeling: model expansion to simulate the effects of precipitation, water absorption, longitudinally changing intestinal permeability, and controlled release on drug absorption. *Drug Dev. Ind. Pharm*., 29, 833–842.

7. Oh, D.M., Curl, R.L., Amidon, G.L. (1993). Estimating the fraction dose absorbed from suspensions of poorly soluble compounds in humans: a mathematical model. *Pharm. Res*., 10, 264–270.

8. Yu, L.X., Lipka, E., Crison, J.R., Amidon, G.L. (1996). Transport approaches to the biopharmaceutical design of oral drug delivery systems: prediction of intestinal absorption. *Adv. Drug Delivery Rev*., 19, 359–376.

9. Yu, L.X., Amidon, G.L. (1998). Characterization of small intestinal transit time distribution in humans. *Int. J. Pharm*., 171, 157–163.

10. Yu, L.X. (1999). An integrated model for determining causes of poor oral drug absorption. *Pharm. Res*., 16, 1883–1887.

11. Sawamoto, T., Haruta, S., Kurosaki, Y., Higaki, K., Kimura, T. (1997). Prediction of the plasma concentration profiles of orally administered drugs in rats on the basis of gastrointestinal transit kinetics and absorbability. *J. Pharm. Pharmacol*., 49, 450–457.

12. Haruta, S., Iwasaki, N., Ogawara, K.I., Higaki, K., Kimura, T. (1998). Absorption behavior of orally administered drugs in rats treated with propantheline. *J. Pharm. Sci*., 87, 1081–1085.

13. Fujioka, Y., Kadono, K., Fujie, Y., Metsugi, Y., Ogawara, K.I., Higaki, K., Kimura, T. (2007). Prediction of oral absorption of griseofulvin, a BCS class II drug, based on GITA model: Utilization of a more suitable medium for in-vitro dissolution study. *J. Controlled Release*, 119, 222–228.

14. Fujioka, Y., Metsugi, Y., Ogawara, K.I., Higaki, K., Kimura, T. (2008). Evaluation of *in vivo* dissolution behavior and GI transit of griseofulvin, a BCS class II drug. *Int. J. Pharm.*, 352, 36–43.

15. http://www.simcyp.com.

16. Sugano, K. (2009). Introduction to computational oral absorption simulation. *Expert Opin. Drug Metab. Toxicol.*, 5, 259–293.

17. Ni, P.F., Ho, N.F.H., Fox, J.L., Leuenberger, H., Higuchi, W.I. (1980). Theoretical model studies of intestinal drug absorption. V. Non-steady-state fluid flow and absorption. *Int. J. Pharm.*, 5, 33–47.

18. Willmann, S., Schmitt, W., Keldenich, J., Dressman, J.B. (2003). A physiologic model for simulating gastrointestinal flow and drug absorption in rats. *Pharm. Res.*, 20, 1766–1771.

19. Willmann, S., Schmitt, W., Keldenich, J., Lippert, J., Dressman, J.B. (2004). A physiological model for the estimation of the fraction dose absorbed in humans. *J. Med. Chem.*, 47, 4022–4031.

20. Clarysse, S., Psachoulias, D., Brouwers, J., Tack, J., Annaert, P., Duchateau, G., Reppas, C., Augustijns, P. (2009). Postprandial changes in solubilizing capacity of human intestinal fluids for BCS class II drugs. *Pharm. Res.*, 26, 1456–1466.

21. Johnson, K.C., Swindell, A.C. (1996). Guidance in the setting of drug particle size specifications to minimize variability in absorption. *Pharm. Res.*, 13, 1795–1798.

22. Avdeef, A., High-throughput solubility, permeability, and the MAD PAMPA model, in: B. Testa, S. Krämer, H. Wunderli-Allenspach, G. Folkers (Eds.) *Pharmacokinetic Profiling in Drug Research*, Wiley-VCH, Zurich, 2006. pp. 221–241.

23. Sugano, K. (2009). Fraction of dose absorbed calculation: comparison between analytical solution based on one compartment steady state approximation and dynamic seven compartment model. *CBI J.*, 9, 75–93.

24. Nomeir, A.A., Morrison, R., Prelusky, D., Korfmacher, W., Broske, L., Hesk, D., McNamara, P., Mei, H. (2009). Estimation of the extent of oral absorption in animals from oral and intravenous pharmacokinetic data in drug discovery. *J. Pharm. Sci.*, 98, 4027–4038.

25. Wagner, J.G. (1967). Method of estimating relative absorption of a drug in a series of clinical studies in which blood levels are measured after single and/or multiple doses. *J. Pharm. Sci.*, 56, 652–653.

26. Loo, J.C., Riegelman, S. (1968). New method for calculating the intrinsic absorption rate of drugs. *J. Pharm. Sci.*, 57, 918–928.

27. Wagner, J.G. (1974). Application of the Wagner-Nelson absorption method to the two-compartment open model. *J. Pharmacokinet Biopharm*, 2, 469–486.

28. Wagner, J.G. (1975). Application of the Loo-Riegelman absorption method. *J. Pharmacokinet Biopharm*, 3, 51–67.

29. Wagner, J.G., Nelson, E. (1963). Per cent absorbed time plots derived from blood level and/or urinary excretion data. *J. Pharm. Sci.*, 52, 610–611.

30. Vaughan, D.P., Dennis, M. (1978). Mathematical basis of point-area deconvolution method for determining in vivo input functions. *J. Pharm. Sci.*, 67, 663–665.

31. Pugh, W.J., Degim, I.T., Hadgraft, J. (2000). Epidermal permeability-penetrant structure relationships: 4, QSAR of permeant diffusion across human stratum corneum

in terms of molecular weight, H-bonding and electronic charge. *Int. J. Pharm.*, 197, 203–211.

32. Pugh, W.J., Roberts, M.S., Hadgraft, J. (1996). Epidermal permeability—penetrant structure relationships: 3. The effect o f hydrogen bonding interactions and molecular size on diffusion across the stratum corneum. *Int. J. Pharm.*, 138, 149–165.

33. Potts, R.O., Guy, R.H. (1992). Predicting skin permeability. *Pharm. Res.*, 9, 663–669.

CHAPTER 6

PHYSIOLOGY OF GASTROINTESTINAL TRACT AND OTHER ADMINISTRATION SITES IN HUMANS AND ANIMALS

"Animals, whom we have made our slaves, we do not like to consider our equal."

—Charles Darwin

It is critically important to use accurate physiological data in biopharmaceutical modeling. The GI physiology has been summarized in many excellent reviews [1–10]. The data presented in this chapter is recompiled from these reviews. Therefore, particular reference is not indicated for each data unless otherwise it is quoted from a specific reference.

6.1 MORPHOLOGY OF GASTROINTESTINAL TRACT

6.1.1 Length and Tube Radius

The tube radius of the small intestine (R_{GI}) is ca. 1.5–2 cm in humans, 0.5 cm in dogs, and 0.2 cm in rats. In monkeys, the intestinal radius ranges from 0.4 cm (cynomolgus monkey) [11] to 0.8 cm (rhesus monkey). In humans, the tube radius of the small intestine decreases while descending the small intestine, from ca. 1.7 cm in the upper intestine to ca. 1.0 at the end of the small intestine.

These differences cause the differences in the surface–volume ratio (SA_{GI}/V_{GI}) (Section 4.4). The permeation rate coefficient (k_{perm}) becomes larger as the intestinal radius becomes smaller, even when the effective intestinal

membrane permeability (P_{eff}) is the same (cf. $k_{perm} = 2/R_{GI} \times DF \times P_{eff}$). This species difference in the intestinal tube radius is canceled out by the difference in P_{eff} (caused by the differences in the fold and villi structures), resulting in similar k_{perm} and Fa% values between animals and humans in case of passive transcellular and UWL-limited permeation (Section 13.5.1).

The postmortem anatomical length of the human small intestine is ca. 680 cm. The living physiological length is ca. 282 cm. The length of the duodenum, jejunum, and ileum is 21, 105, and 156 cm, respectively.

In contrast to humans, the portion of ileum in the small intestine is very small in rats and dogs, ca. 2% and 4%, respectively (Table 6.1).

6.1.2 Surface Area

6.1.2.1 Small Intestine.
In humans, the surface area of the small intestine is expanded by the fold (plicae, ×3), villi (×10), and microvilli (×20) (Fig. 6.1; Table 6.2). On the basis of the smooth surface geometry, the surface area of the small intestine is ca. 3000 cm². The surface area is expanded to 10,000, 100,000, and 2,000,000 cm² by the fold, villi, and microvilli structures, respectively. However, drug particles are inhomogeneously distributed along the small intestine and the intestinal surface is not fully exposed to the drug. Dogs and rats lack the fold structure.

Figure 6.2 shows the structure of villi. Rats have shorter villi length than dogs and humans. As the effective intestinal membrane permeability (P_{eff}) is defined on the basis of the smooth tube surface, the morphological differences of the fold and the villi are one of the reasons for the species differences in P_{eff}. These morphological differences decrease P_{eff} threefold in dogs (except for paracellular permeants[1]) and sixfold in rats compared to that in humans. Monkeys have plicate and villi structure; however, the surface area information is not available. In monkeys, the P_{eff} values of several UWL-limited permeation drugs are ca. threefold lower than those in humans [11], suggesting that the surface area expansion by the plicate structure might be less significant in monkeys. Caco-2 cells do not have the fold and villi structures but have a microvilli structure.

TABLE 6.1 Percentage of Length of Small Intestinal Parts[a]

	Human, %	Dog, %	Rat, %
Duodenum	4	6	8
Jejunum	38	90	90
Ileum	58	4	2

[a]Reference 3.

[1]In one commercial software (as of 2011), the P_{eff} value of any drug in dogs is assumed to be threefold larger than that in humans regardless of the permeation pathway of the drug. However, this assumption is not valid for the transcellular and UWL-controlled cases, in which the P_{eff} in dogs is threefold lower than that in humans.
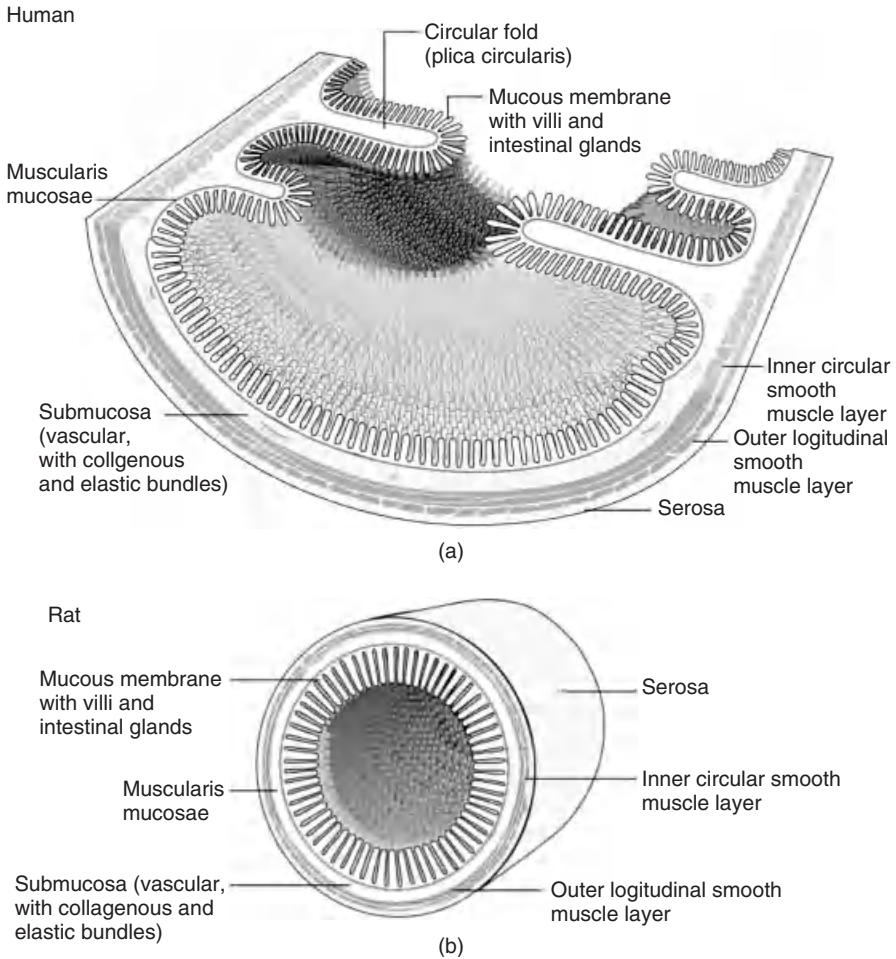
Figure 6.1   Structure of the small intestine in humans and rats. *Source:* Adapted from Reference 2 with permission.

TABLE 6.2   Surface Expansion by Plicae and Villi

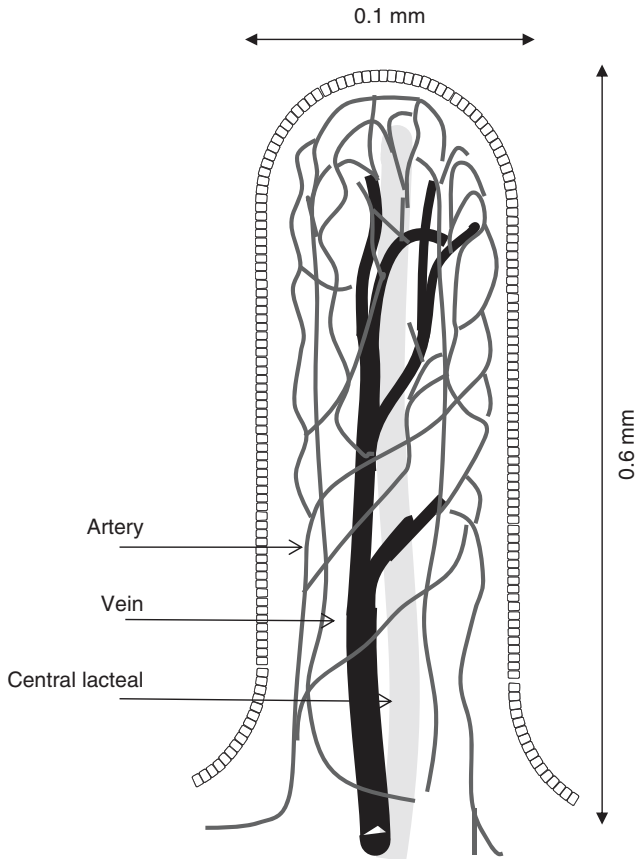|	Human	Dog	Rabbit	Rat
Plicae (PE; small intestine)	3	1	1	1
Villi (VE; small intestine)	10	10	5.7	5
Microvilli (small intestine)	20	25	24	20
DF (small intestine)	1.7	—	—	—
DF (colon)	5.3	—	—	—

Figure 6.2 Structure of the villi [12].

Therefore, the epithelial membrane permeability (P_{app}) in the Caco-2 models is ca. 30-fold smaller than the human P_{eff} value in case of epithelial-membrane-limited permeation.[2]

6.1.2.2 Colon. The effective permeability of a drug in the colon is usually lower than that in the small intestine due to the lack of both plicate and villi structures in the colon. The ratio of the available surface area is ca. 1:30 in humans (colon/small intestine).

In rats, both the small intestine and colon lack the plicate structure. The villi expansion was ca. fivefold in the rat intestine, whereas no villi exist in the

---

[2]This cannot be applied for the UWL permeation cases. The UWL thickness of the *in vitro* planner membrane system is 5- to 10-fold thicker than that of the *in vivo* intestine. The apparent permeability (P_{app}) of an *in vitro* assay, which is usually reported in the literature, is the composite parameter of the UWL permeability (P_{UWL}) and epithelial membrane permeability (P_{ep}) as $1/P_{app} = 1/P_{ep} + 1/P_{UWL}$.

colon. Using these morphological data, the ratio of colonic and intestinal P_{eff} becomes 1:5 for epithelial-membrane-limited permeation cases. This value is in good agreement with the experimental observations (Section 13.6.1). It would be worth noting that the observed P_{eff} ratio values were similar between passive transcellular and paracellular pathway permeations, suggesting that the relative P_{eff} ratio is mainly determined by the difference between the surface areas of the small intestine and colon, rather than by the difference between the pore size of paracellular pathway and the membrane fluidity [13].

6.1.3   Degree of Flatness

6.1.3.1   *Small Intestine.* To calculate the permeation rate coefficient (k_{perm}) of a drug from P_{eff}, either one of the two combinations of information is required, DF–R_{GI} or SA$_{\text{GI}}$–V_{GI} (Section 4.4).

$$k_{\text{perm}} = \text{DF} \cdot \frac{2}{R_{\text{GI}}} \cdot P_{\text{eff}} = \frac{\text{SA}_{\text{GI}}}{V_{\text{GI}}} \cdot P_{\text{eff}} \tag{6.1}$$

Neither the data on the surface area exposed to the dissolved drug (SA$_{\text{GI}}$) nor the direct measurement of DF is available in the literature. In this book and most of the commercial software, the DF–R_{GI} combination is used, as it is compatible with the GI compartment models. From the experimental P_{eff}, and Fa% data, DF of the human small intestine was estimated to be 1.7 (Fa $= 1 - \exp(-2\text{DF}/R_{\text{GI}} \times P_{\text{eff}} \times T_{\text{si}})$, R_{GI} (1.5 cm), and T_{si} (3.5 h); Section 8.4.1; Figure 8.2). This DF value denotes that the small intestine is like a deflated tube (Fig. 4.3). From the fluid volume in the intestine (130 ml) and the degree of flatness (1.7), SA$_{\text{GI}}$ is estimated to be ca. 300 cm^2 (2DF/R_{GI} = SA$_{\text{GI}}$/V_{GI}) in the fasted state.

6.1.3.2   *Colon.* Owing to the substantial residence time in the ascending colon and the limited free water volume in the transverse and descending colon, the primary region of interest with regard to drug/dosage form performance in the lower gut is the ascending colon [14].

Owing to the lack of the colon P_{eff} data in humans, we were not able to obtain DF value in humans from the Fa–P_{eff} relationship. However, the DF of the human ascending colon (DF$_{\text{AC}}$)[3] can be estimated from the relative Fa% of drugs with low permeability from the small intestine and the colon, using the following equation:

$$\frac{\text{Fa}_{\text{AC}}}{\text{Fa}_{\text{SI}}} = \frac{2\text{DF}_{\text{AC}}\big/R_{\text{GI,AC}}}{2\text{DF}_{\text{SI}}\big/R_{\text{GI,SI}}} \frac{P_{\text{eff,AC}}T_{\text{si}}}{P_{\text{eff,SI}}T_{\text{AC}}} \tag{6.2}$$

Considering the lack of villi and plicae in the colon (10- and 3-fold expansion, respectively), if we assume that the difference in the P_{eff} is due to its surface

---

[3]The subscripts AC and SI indicate the ascending colon and the small intestine, respectively.

area,[4] $P_{eff,AC}/P_{eff,SI}$ should be 1:30 in humans in case of epithelial membrane permeability. The radius of the small intestine and colon is 1.5 and 2.5 cm and the transit times are 3.5 and 13 h, respectively. The average of the observed relative Fa (Fa_{AC}/Fa_{SI}) for BCS class III compounds ($Fa_{oral}\% < 70\%$) was 0.29 ± 0.13 ($n = 10$) (including all charges (neutral, positive, and negative) and wide MW range (217–538)) [15]. When limited to the passive transcellular permeation of neutral compounds, which would not be affected by the possible difference of the paracellular pathway and pH, the observed Fa_{AC}/Fa_{SI} was 0.24 ($n = 2$). DF_{SI} is 1.7. From these data and Equation 6.2, DF_{AC} was estimated to be 5.3.

This high DF value in the colon compared to the small intestine may be due to the small fluid volume in the colon (15 ml) spread on the colonic wall (Section 6.3.1) [14].

6.1.4 Epithelial Cells

The intestinal epithelial membrane consists of intestinal epithelial cells tightly connected each other (Fig. 4.1). The tight junction restricts the lateral diffusion of the membrane components. The apical side has a microvilli structure. However, the surface area ratio of the apical and basolateral sides was measured to be ca. 1–3 [16], probably because the tight junction exists close to the apical side and the most part of the side face of the cell contacts the basolateral space.

Drug molecules can permeate across the layer of the epithelial membrane via the cellular membrane (transcellular) and the tight junction (paracellular). Transcellular permeation of most drugs occurs mainly by passive diffusion, but some drugs permeate the membrane mediated by a carrier protein(s) (transporter). In addition, drugs can be metabolized in the enterocyte (intestinal first-pass metabolism). Transporters and metabolic enzymes in the intestinal epithelial cells are discussed in Section 6.4.

6.1.4.1 Apical and Basolateral Lipid Bilayer Membranes.

Typical lipid components of biological membranes are shown in Figure 6.3. Phosphatidyl-choline (PC) and phosphatidylethanolamine (PE) are zwitterionic phospholipids with zero net charge at neutral pH. Phosphatidylserine (PS) has two negatively charged moieties (pK_a on the membrane, carboxylate ($pK_a = 5.5$) and phosphate ($pK_a < 1$)) and one positively charged moiety (amine ($pK_a = 11.3$)), with a net charge of -1. Phosphatidylinositol (PI) and phosphatidylglycerol (PG) have one negatively charged moiety (phosphate ($pK_a = 2.7$ (PI), 2.9 (PG))). The lipid bilayer of the intestinal epithelial cells contains significant amount of anionic phospholipids (Table 6.3) [17, 18]. The distribution of negatively charged lipid is nearly symmetrical in the intestinal brush border membrane, which is in contrast to the red blood cells (Table 6.4) [19, 20].

---

[4]This assumption is validated by the $P_{eff,AC}/P_{eff,SI}$ ratio in rats, which is ca. 0.2 as this value is in good agreement with the fivefold surface expansion by villi and plicae in the small intestine in rats (Table 13.1).

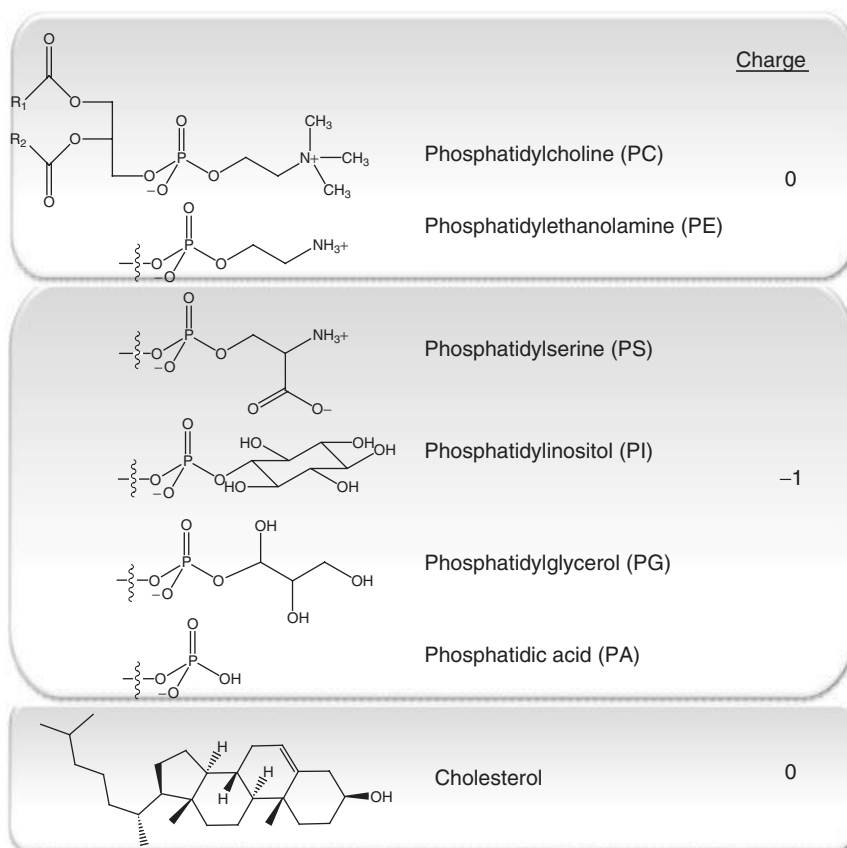**Figure 6.3**   Chemical structure of lipid bilayer components.

TABLE 6.3   Lipid Bilayer Component

Lipid	Brush Border Membrane (Rat)	Caco-2	Egg Lecithin	Soybean Lecithin
PC	20	53	73	24
PE	18	19	11	18
PS	6	17	—	—
PI	7	8	1	12
Sphingomyelin	7	3	—	—
CHO	37	—	—	—
Triglyceride	—	—	13	37

TABLE 6.4   Inner and Outer Leaflet Distribution of Lipid Component

Lipids	Rabbit Intestinal Brush Border		Red Blood Cell	
	Outer Layer, %	Inner Layer, %	Outer Layer, %	Inner Layer, %
PC	32	68	76	24
PE	34	66	20	80
PS	44	56	0	100
PI	40	60	—	—
Sphingomyelin	—	—	82	18

A lipid bilayer is a heterogeneous system that can be roughly divided into four regions (Fig. 6.4), although the boundary of each region is not explicit [21, 22].

- Low Density Head Group Region. This region ranges from the point where the membrane begins to perturbate the bulk water structure to the point where the water density and head group density are comparable. This region can be large because the perturbation of water molecules can extend over a long range.
- High Density Head Group Region. This region is ca. 7.5 Å wide. In this region, bulk water structure no longer exists. It has a high dielectric constant (ε = ca. 30) and high viscosity and is abundant in hydrogen bond acceptors.
- High Density Tail Region. This region is ca. 7 Å wide. It has a low dielectric constant and high viscosity. The hydrocarbon tail has a high density and is highly ordered. The region is considered to resemble a soft polymer.
- Low Density Tail Region. This region is ca. 11 Å wide (both halves of the bilayer). It has a low dielectric constant (ε = ca. 2) and low viscosity. This region is considered to resemble a low density alkane fluid, such as dodecane or hexadecane.
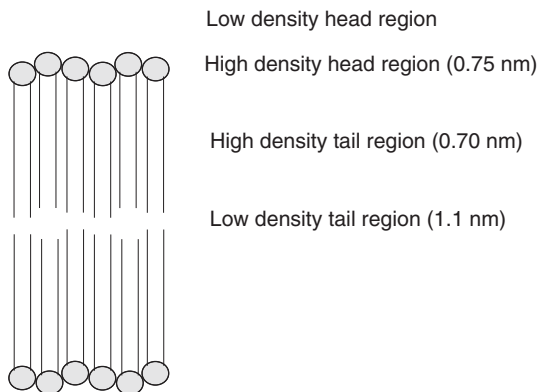

Figure 6.4   Regions of lipid bilayer.

Drug molecules diffuse through the lipid bilayer, depending on the physicochemical property of a drug, especially lipophilicity. Unlike the carrier-protein-mediated transport, passive diffusion is not structure specific. Therefore, the passive diffusion is, and will continue to be,[5] the main permeation mechanism for most drugs.

6.1.4.2   *Tight Junction.* The epithelial cells of the GI tract are tightly connected by cell adhesion proteins such as occludens [23]. The apparent pore radius of the tight junction is ca. 6 Å in humans and 9 Å in dogs [24–26]. The pore radius of the tight junction of Caco-2 cells has a large laboratory to laboratory variation [27], and therefore, it should be measured in each laboratory. In many cases, it is smaller than that in humans. The tight junction is negatively charged with 70 mV in humans [24] and 17 mV in Caco-2 cells (Fig. 6.5) [28, 29]. Owing to this negative charge, a positively charged molecule is more permeable than a negatively charged molecule (Fig. 4.14). Masaoka et al. [13] reported that the effective pore sizes of the paracellular pathway were similar between the small intestine and the colon.

Recent quantitative assessments suggested that paracellular permeation is more significant than it was originally thought for drug absorption [24, 30–33]. Many drugs such as H2 blockers and β-blockers permeate this pathway significantly. As shown in Figure 4.14, in the case of basic drugs of MW up to 350, this route can contribute an Fa% more than 30%, which is sufficient to launch on the market.

6.1.4.3   *Mucous Layer.* The mucous layer exists adjacent to the epithelial cells (Fig. 6.6). Figure 6.7 shows the structure of the mucous layer [34]. The mucous layer is thought to maintain the UWL and microclimate pH. The mucous
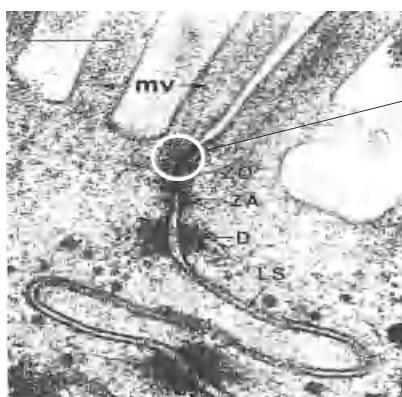
Figure 6.5   Tight junction. *Source*: Adapted from Reference 28 with permission.

---

[5]It is difficult to design a dual substrate for both an absorptive transporter and an pharmacological target, as the substrate specificity of the former tends to be narrow and selective.
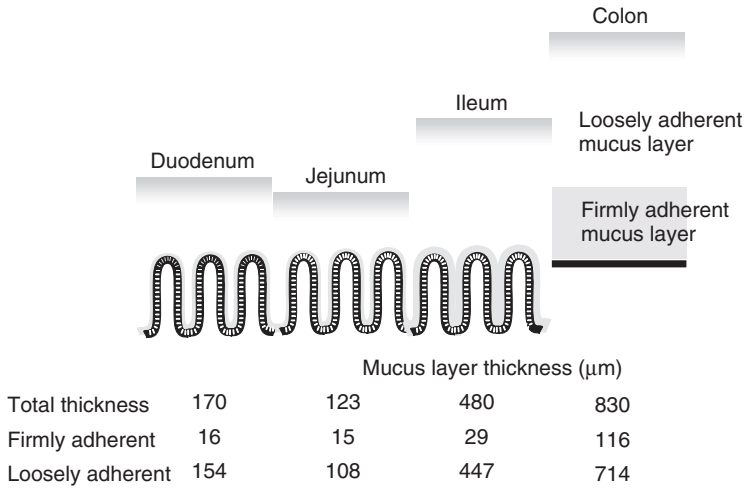
Mucus layer thickness (μm)			
Total thickness	170	123	480	830
Firmly adherent	16	15	29	116
Loosely adherent	154	108	447	714

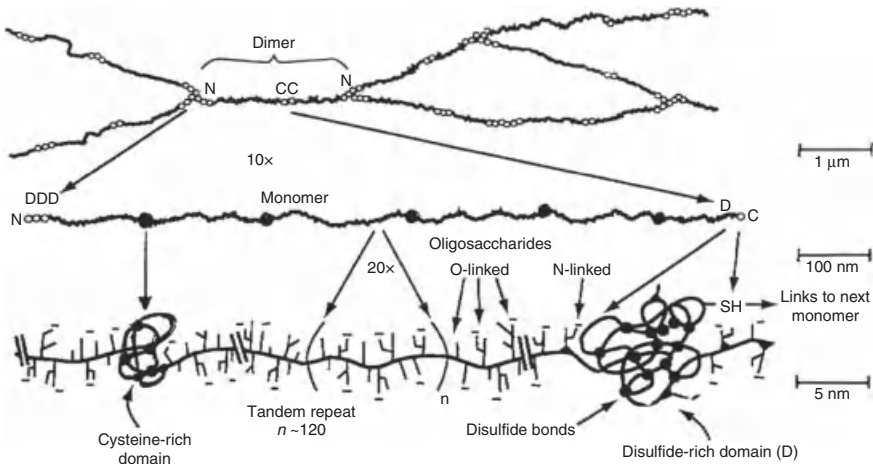**Figure 6.6** A schematic figure showing the thickness of the mucous gel layers *in vivo* [36].

Figure 6.7 Structure of the mucous layer. *Source:* Adapted from Reference 34 with permission.

layer is divided into two regions, the firmly adhered and loosely bound regions [35, 36]. The loosely bound mucus can be wiped away by the luminal fluid flow. In places where intestinal chyme wipes away the mucous blanket, the glycocalyx (0.5 μm thick) forms the final barrier that can prevent pathogens and drug delivery particles from adhering to the epithelial cell surface. The secretion of mucus is rapid, and the mucous layer grows ca. 1 μm/s in the rat small intestine [36].

The mucin fibers that form mucous gel are long flexible strings densely coated with short glycans, most of which are functionalized with a carboxyl or sulfate

group. The mesh size of the mucous layer is thought to be at least greater than 0.4 μm. Therefore, nanoparticles can penetrate to the mucous layer [34]. Many studies showed that even microscale particles were found in the mucous layer [37–41].

6.2 MOVEMENT OF THE GASTROINTESTINAL TRACT

6.2.1 Transit Time

6.2.1.1 *Gastric Emptying Time (GET).* The gastric emptying pattern largely depends on the contents of the stomach and the size of the formulation [42]. For liquids and small particles, the $T_{1/2}$ of the content in the fasted state in humans is ca. 10 min. In the fed state, the $T_{1/2}$ of the content is ca. 1 h. This difference causes a typical reduction in C_{max} and delay in T_{max} of a drug in the fed state. The relationship between the caloric density of the food and the gastric emptying rate is shown in Table 6.5 and Figure 6.8 [43]. Factors such as posture, pain, and disease conditions affect gastric emptying time (GET) [44].

On the other hand, the GET of solid objects larger than ca. 0.5 mm is associated with phase II or III of migrating motor complex (MMC), which is observed in the fasted state. When an object with this size range is administered in the fed state, only after MMC has resumed, gastric emptying of these objects occurs [5].

In dogs and monkeys, the GET of a solution in the fasted state is similar to that in humans [45]. However, the GET in the fed state is longer in dogs than that in humans [46]. In pigs, the mean time for 50% emptying of the liquid in the fasted state is approximately 1.4 h [42].

6.2.1.2 *Small Intestinal Transit Time.* The small intestinal transit time (SITT) is ca. 3.5 h for both the fasted and fed states in humans. In contrast to the stomach emptying time, the intestinal transit time is not largely affected by the size of the formulation [42]. However, it is significantly shortened to 1.7–2.4 h when a tablet is administered 45 min before food intake because of a strong housekeeping wave [47].

In dogs and monkeys, the SITT was suggested be shorter than that in humans (3.5 vs 2 h, respectively) [45].

TABLE 6.5   **The Caloric Density of Food and the Gastric Emptying Rate**[a]

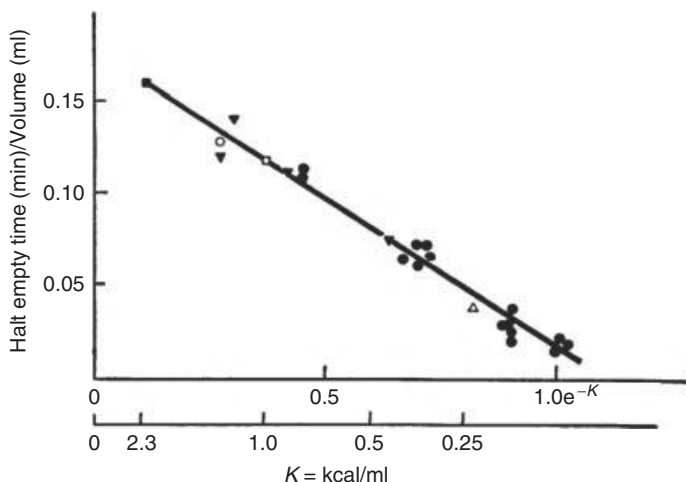|	Meal Volume, ml			
Caloric Load, kcal	200	400	600	800
200	56	41	42	38
300	74	59	60	56
400	92	77	78	74

[a] Reference 5.

Figure 6.8   Gastric emptying time and caloric density of the food. *Source*: Adapted from Reference 43 with permission.

6.2.1.3 Colon Transit Time.
The ascending colon transit time in humans was reported to be ca. 13 h and not significantly different depending on the formulation size [48].

6.2.2 Migrating Motor Complex

In the fasted state, the MMC controls the motility pattern (Fig. 6.9) [49]. The MMC cleanses the stomach and the small intestine acting as "the housekeeper wave." The MMC consists of at least three distinct phases (Tables 6.6 and 6.7) with a combined total average duration of about 100 min:

  phase I (ca. 60 min)—less than three pressure waves per 10 min;
  phase II (ca. 30 min)—period of irregular contractions;
  phase III (ca. 2–15 min)—regular rhythmic contractions at high frequency.

There is also a phase IV, a brief period of transitional motor activity from the intense phase III to the quiescent phase I.

The propagation velocity in the duodenum, the proximal jejunum, and the distal ileum is 10, 7, and 1 cm/min, respectively. Only half of them propagate beyond the middle jejunum, and only 10% reaches the distal ileum.

When food is taken in, the MMC activity is lost and fed state motility is reached (Fig. 6.10). The partial secretion of bile in the fasted state is related to the MMC (Section 6.6.1).

Dogs have an MMC pattern similar to that in humans. However, as the gastric emptying of food is slower than that in humans, the MMC phase III also resumes
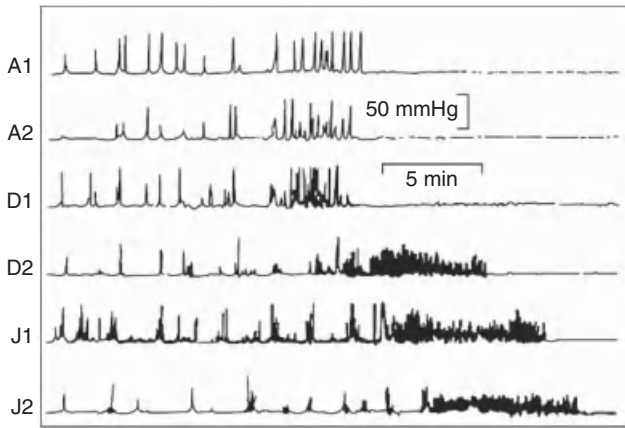
(a)
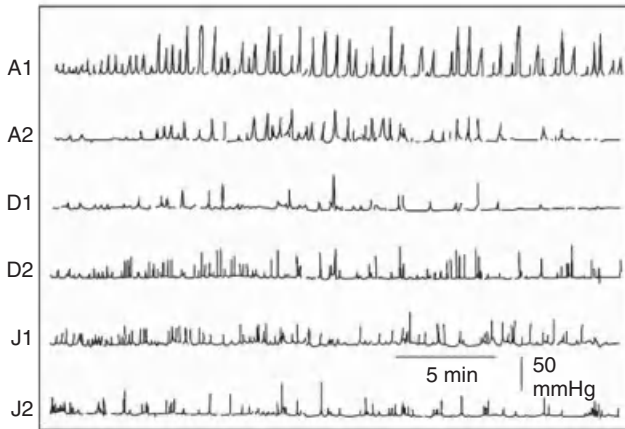
(b)

Figure 6.9 Intraluminal pressure recordings in the (a) fasted and (b) fed states of a healthy volunteer. *Source*: Adapted from Reference 49 with permission.

TABLE 6.6   Return of MMC Phase III After Meal[a]

Species		Time for MMC Phase III to Resume, min
Human	285 kcal, liquid	156 ± 54 (SD)
	500 kcal, solid	288 ± 90 (SD)
Dog	30 kcal/kg solid	324 ± 23 (SE)
	60 kcal/kg solid	561 ± 31 (SE)
	90 kcal/kg solid	799 ± 33 (SE)

[a] Reference 46.

TABLE 6.7   Mean Flow Rate in Various Intestinal Segments in Humans[a]

| MMC Phase | Mean Flow Rate, ml/min, mean $\pm$ SD | | |
	Jejunum	Ileum	Terminal Ileum
I–II	0.58 ± 0.12	0.17 ± 0.03	0.33 ± 0.01
III	1.28 ± 0.18	0.50 ± 0.13	0.65 ± 0.01
Mean phase (I–III)	0.73 ± 0.11	0.33 ± 0.09	0.43 ± 0.06
Fed state	3.00 ± 0.67	2.35 ± 0.28	2.09 ± 0.16

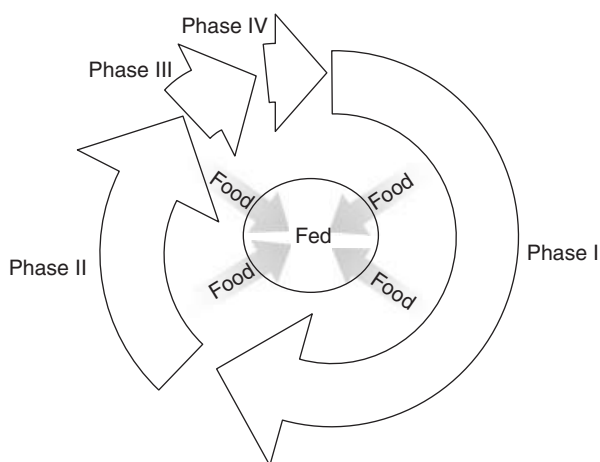[a] Reference 51.

Figure 6.10   MMC cycles.

more slowly [46]. Rats have indistinct MMC pattern and shorter MMC cycle time (20–30 min) [50].

6.2.3   Agitation

6.2.3.1   Mixing Pattern. The mixing pattern in the stomach is not homogeneous. Using computational fluid dynamic (CFD) simulation, Pal et al. [52] investigated the role of antral contraction wave (ACW) activity of gastric fluid motions, pressure, and mixing. Gastric mixing was found to be limited to the antrum where occluding ACW generates strong gastric fluid motions (Fig. 6.11). Dillard et al. [53] investigated the mixing pattern at the pylorus and superior duodenum. It was found that the asymmetric geometry of the pyloric orifice in concert with intermittent gastric outflow and luminal constriction is likely to enhance homogenization of gastric effluent with duodenal secretion.

    There are two types of large-scale intestinal wall movements in the unanesthetized state, the periodic segmental contraction and the periodic peristaltic
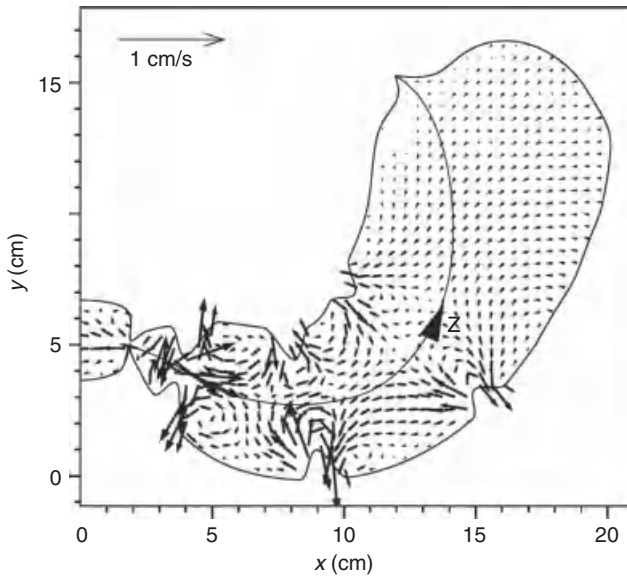
Figure 6.11   Mixing patterns in the stomach. *Source*: Adapted from Reference 52 with permission.

movement (Fig. 6.12), the former was suggested to be the main contributor for mixing, whereas the latter moves the chyme toward the distal position. The periodic segmental contraction and peristaltic movement of the intestine would knead and mix the intestinal fluid effectively in spite of the low Reynolds number in the intestine with little turbulent flow (= little eddy diffusion and dissipation). In

Figure 6.12   Segmental contraction and the periodic peristaltic movement. *Source*: Adapted from Reference 55 with permission.

Figure 6.13 Baker's transformation. *Source*: Adapted from Reference 55 with permission.

other words, the fluid mixing pattern can be chaotic even without turbulence (periodic laminar mixing is also called *chaotic mixing* [54] and is rela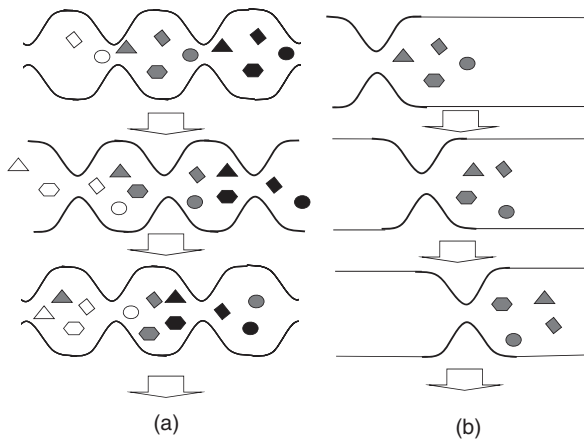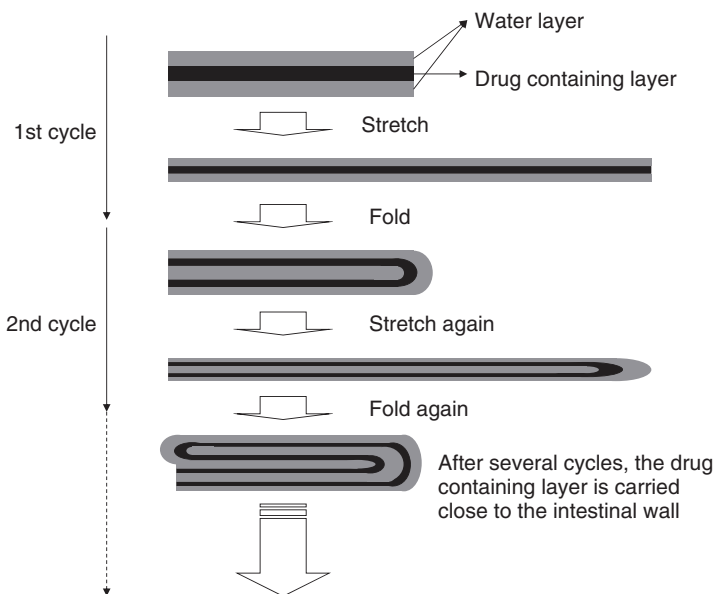ted to Baker's transformation (Fig. 6.13)). This mixing pattern brings the drug and nutrient molecules close to the intestinal wall, hence reducing the UWL thickness adjacent to the intestinal membrane. Theoretical estimation of the effect of laminar mixing on the UWL thickness would be the subject of future investigation.

The villous mobility (mainly vertical shrinking) [56, 57], which is present in humans and dogs but not in rats, was suggested to be not effective to reduce the UWL thickness [58]. This is in good agreement with the Reynolds number of villi being much less than 1 (much smaller than the *Re* for the intestinal tube scale). The microfluidics induced by the villous motility would be laminar and no mixing would occur. At $Re \ll 1$, viscosity significantly surmounts the inertia of fluid velocity and the fluid is stagnant on the wall, that is, the fluid moves together with the villi wall dragged by viscosity. The vertical shrinking movement would not produce a knead-and-mix pattern.

There were several experimental attempts to characterize the flow regime of the intestine. Janssen et al. [59] reported that some elements of turbulence were observed when the intestinal fluid had a viscosity close to water, whereas it was absent when the intestinal fluid had higher viscosity such as in the fed state chyme.

6.2.3.2 *Agitation Strength.* The effective agitation strength in the GI tract was assessed by comparing the *in vitro* and *in vivo* drug release profiles for a

TABLE 6.8   Agitation Strength and Destructive Force[a]

	Humans		Dogs		Monkeys		Rats	
	Fasted	Fed	Fasted	Fed	Fasted	Fed	Fasted	Fed
Agitation strength (as rpm in compendium paddle speed)								
	10	—	100	—	10–50	—	10 ~ 50	—
Destructive force, N								
Stomach	1.5	1.9	3.2	3.2	—	—	—	—
Small intestine	1.2	—	1.2	—	—	—	—	—

[a]References 45, 60–63, and 65–68.

matrix-type erosive dosage form. The compendium dissolution test was used as the *in vitro* disintegration and dissolution tests, and the paddle rotation speed that gives a release profile equivalent to *in vivo* release was considered as the representative agitation strength (Table 6.8). For humans, a paddle rotation speed of 10–30 rpm [60–63] was found to be representative, whereas it was more than 100 rpm and 10–50 rpm in dogs and monkeys, respectively [45]. A paddle speed of 50 rpm in the compendium dissolution test equals to 0.004 m^2/s^3 (energy input per time) [64].

The destruction force is not equal to the agitation strength, as the contact with the intestinal wall can influence the destruction force. In humans in the fasted state, the destruction force is 1.5 and 1.9 N in the stomach and intestine, respectively [65]. In dogs, the destruction force in the stomach is 3.2 N, which is higher than that in humans. The highest destruction force would be observed when the formulation passes through the antrum.

6.2.3.3 *Unstirred Water Layer on the Intestinal Wall.* The existence of the UWL in the intestine *in vivo* is often argued. From the fluid dynamic theory, the existence of the UWL is 100% sure. When the intestinal wall moves, the fluid adjacent to the wall also moves in a synchronized manner towed by the viscosity of the fluid. In addition, the eddy of turbulence cannot reach the intestinal wall. Therefore, by the action of the viscosity of the fluid, even though the intestinal fluid is agitated by the movement of the intestinal wall, the UWL cannot be completely removed. The question is how much diffusion resistance is maintained by the UWL.[6] In this book, based on the following discussion, 300 μm is used as the best guess value for UWL thickness.

There had been a controversy in the literature about the UWL thickness (h_{UWL}) in the small intestine. Previously, the UWL thickness was estimated to be ca. 700 μm from the rat small intestinal perfusion experiments under anesthetized conditions [69]. On the other hand, in conscious humans, it was estimated to be

---

[6]The concept of the "thickness of UWL" is based on the film model. The h_{UWL} is an operational term because the well-mixed phase and the UWL are not well defined. Therefore, the so-called UWL thickness corresponds to the effective diffusion resistance of the boundary layer, which has the dimension of length.

30–130 μm (based on the smooth tube surface) [70, 71]. When corrected for the fold (plicae) structure (threefold), the actual thickness of the UWL was found to be 90–400 μm. This is in good agreement with the mucous layer thickness of 100–200 μm on the villi tip obtained by a direct measurement (Fig. 6.6). Recently, the UWL thickness was retrospectively estimated from human Fa% of several model drugs whose oral absorption is solubility-UWL limited [72]. To neglect the particle drifting effect, Dose <5 mg/kg and $d_p > 10$ μm were selected (cilostazol, irbesartan, phenytion, and spironolactone). The estimated UWL thickness was 332 μm. This value is very close to the experimentally estimated value by Lennernäs (384 μm based on glucose P_{eff} at the infusion rate of 1.5 ml/min (after plicae effect correction)) [71] and the computationally simulated value by Wang et al. (Fig. 6.14) [73]. The lower values reported in the literature (40 μm based on the smooth tube surface) were obtained from an infusion study with the flow rate of 7.5–20 ml/min [70]. These high perfusion rates might cause an artifactual reduction in the UWL thickness, as the normal flow rate in the proximal small intestine has been reported to be 0.6–4.2 ml/min in humans, including both fasted and fed states [74].

The UWL thickness values in rats, dogs, and monkeys are not well known. In dogs, the UWL was estimated to be 35 and 50 μm at the perfusion rates of 26 and 5 ml/min, respectively [70]. Considering the difference in the intestinal diameter, these flow rates in dogs are also very high. From the absorption flux data of glucose (threefold lower in dogs compared to humans) [75] and the difference in the fold structure (dogs do not have the fold structure), the UWL thickness of dogs is suggested to be similar to that in humans.

In rats, the UWL thickness is suggested to be similar to that in humans, based on the similar discussion for dogs [75]. In monkeys, due to the lack of information about the plicae expansion, it is difficult to estimate the UWL thickness. On the basis of the effective permeability of antipyrine and assuming that the plicae
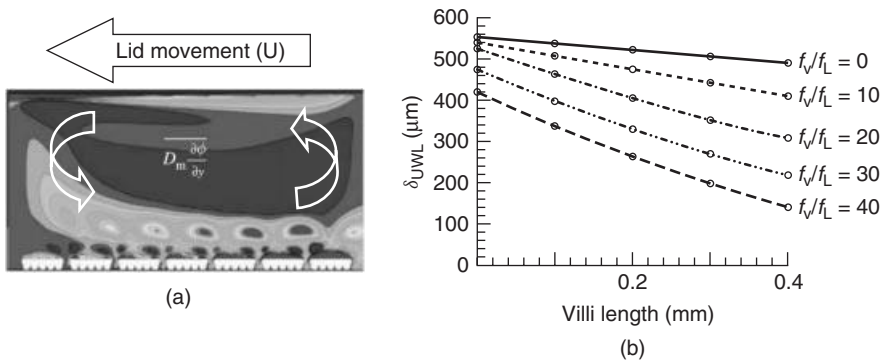

Figure 6.14 UWL simulation results. (a) Vertical diffusional mass transfer. The gray concentration corresponds to the UWL. (b) The effect of villi length and oscillation frequency on the UWL thickness. f_v/f_L is the frequency ratio of cavity eddy and the villi oscillation. *Source*: Adapted from Reference 73 with permission.

expansion was not as large as that in humans, the UWL thickness of monkeys is suggested to be similar to that in humans [11].

The thickness of the UWL is theoretically estimated to be greater than 1 cm in humans if the flow pattern is a straight laminar flow (the Graetz problem (Section 3.2.4.3)). Therefore, the *in vivo* UWL (ca. 300 µm) is very thin, suggesting that the intestinal fluid is effectively agitated. Therefore, the flow pattern should not be a straight laminar flow in the conscious human. At the same time, the Reynolds number calculated for the intestinal tube, tablet, and drug particles suggests that the flow patterns around these objects in the intestine could be only weakly turbulent. As discussed above, "periodical laminar mixing" could be an additional mechanism for the effective mixing in the GI tract (Fig. 6.12).

Figure 6.14 shows the CFD simulation results for the flow and mass transfer patterns in the small intestine reported by Wang et al. [73]. To simulate the macro- and microscale phenomena simultaneously, a two-dimensional multiscale lattice Boltzmann model was used. The flow pattern was modeled as a lid-driven cavity flow with oscillating villi at the lower surface. The cavity characteristics were set to roughly consistent with the macroscales of the human jejunum: cavity length and height $L \times H = 6\text{mm} \times 3$ mm and lid velocity $U = 2$ mm/s. Figure 6.14 shows the visual pattern of the mass transfer in the cavity. Convective flux is overall larger than diffusive flux everywhere except in the diffusion-dominated UWL adjacent to the villi surfaces. The estimated UWL thickness is in the range of 200–500 µm.

In contrast to the conscious *in vivo* situation, the UWL under anesthetized state was suggested to be much thicker [75].

In the colon, due to solidified chyme (high viscosity), significantly thick mucous layer, and lesser mobility, the UWL thickness would be significantly thicker than that in the small intestine.

6.3 FLUID CHARACTER OF THE GASTROINTESTINAL TRACT

6.3.1 Volume

6.3.1.1 Stomach. The resting fluid volume in the stomach is ca. 30 ml in humans. The stomach secretes the stomach fluid at the rate of 1.2 ml/min (zero-order rate). In addition, 0.9 ml saliva flows into the stomach per minute. The gastric emptying rate follows the first-order rate of 0.0693 min^{-1}. The balance of flow-ins and flow-out determines the steady-state resting volume to be ca. 30 ml (Section 2.10).

6.3.1.2 Small Intestine. There had been a controversy about the intestinal fluid volume in the literature.[7] Currently, the average fluid volume in the fasted

---

[7]In some reports, $V_{GI} = 600$ ml was used with the surface area of 800 cm^2, that is, $SA_{GI}/V_{GI} = 1.3$, which is equal to the cylindrical tube shape. Compared to the current most credible values of $V_{GI} = 130$ ml and $SA_{GI}/V_{GI} = 2.3$, the previous V_{GI} is larger and the previous SA_{GI}/V_{GI} is smaller. These

human small intestine is estimated to be ca. 130 ml, but it has a large variation. The following evidence support this value:

- direct measurements by MRI in conscious states (107 and 10–100 ml) [76, 77];
- direct measurement in postmortem state (207 ml) [4];
- indirect estimation from the dose–Fa% profiles of four SL-E compounds (130 ml) [72];
- indirect estimation from the intubations study of the precipitation–absorption study (130 ml) [78];
- K_i value and dose–CYP inhibition relationship of cimetidine (ca. 190 ml)[8] [79, 80].

These fluid volume values are in good agreement with the deflated tube shape and the surface–volume ratio of 2.4–2.6 (i.e., degree of flatness (DF) = 1.7).

The intestinal fluid is heterogeneously distributed across the small intestine as four to five water pockets (Fig. 6.15) [76]. Therefore, it was suggested that the dosage form is not always soaked in the intestinal fluid during the GI transit. In the fasted state, when 28 capsules were ingested by multiple human subjects, only 50% of the capsules were completely soaked in the intestinal fluid.

It is difficult to estimate the fluid volume in the fed state, as a large portion of the fluid is bound to the food and might not be available for drug dissolution. From the retrospective analysis using the fed/fasted AUC ratio of SL-E drugs, the effective fluid volume was estimated to be 1.2-fold larger than that in the fasted state [81].

The intestinal fluid volume tended to be higher in men than in women (ca. twofold) [82].

6.3.1.3   Colon. The fluid volume in the human ascending colon is ca.15 ml in both fasted and fed states [83]. Most of the cavity is filled with 200 ml of gas, which is roughly equal to the geometric capacity of the ascending colon.

6.3.2   Bulk Fluid pH and Buffer Concentration

The ranges of pH values for various animal species are shown in Table 6.9.

---

errors worked in opposite directions and were coincidently canceled out, resulting in semiquantitative Fa% prediction for solubility-permeability-limited cases. However, with V_{GI} = 600 ml, the inflation point in the dose–AUC curve would be upshifted (Fig. 10.1). In addition, with SA_{GI}/V_{GI} = 1.3, for permeability-limited cases, human Fa% is underestimated by ca. twofold from the experimental P_{eff} values in humans (Fig. 8.2).

[8] In the original paper, the fluid volume was estimated to be 1900 ml based on the assumption that the cytosol and luminal free drug concentration is equal. However, the cytosol free drug concentration should be significantly smaller. When the concentration gradient across the apical and basolateral sides is taken into account, the V_{GI} can be estimated to be 190 ml.
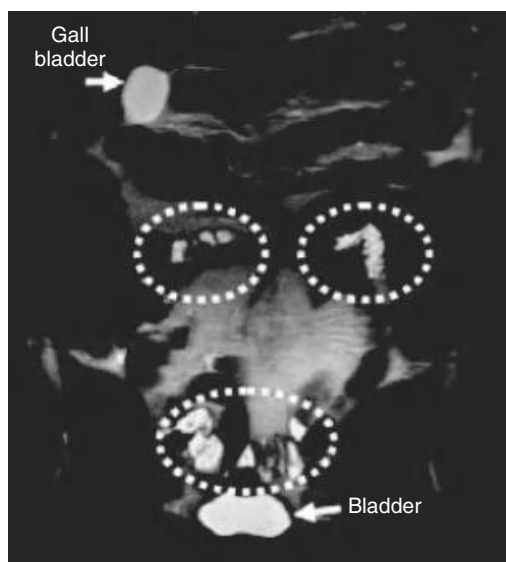
Figure 6.15   Magnetic resonance images showing the identification and segmentation of intestinal fluid pockets in the fasted state. *Source*: Adapted from Reference 76 with permission.

TABLE 6.9   Gastrointestinal Fluid pH and Bile Concentration[a]

	Humans		Dogs		Monkeys		Rats[b]	
	Fasted	Fed	Fasted	Fed	Fasted	Fed	Fasted	Fed
Fluid volume, ml								
Stomach	30	—	—	—	—	—	0.5	1.1
Small intestine	130	156	—	—	—	—	1.5	3.8
Colon	15	17	—	—	—	—	0.6	2.2
Bulk pH								
Stomach anterior	1.5–5.0	6	1.5–5.5	—	4.7–5.0	—	3.9	3.2
Stomach posterior	5.0–7.0	—	1.5–3.4	—	2.3–2.8	—	—	—
Duodenum	6.0–7.0	—	6.2	—	5.6–6.0	—	5.89	5.00
Jejunum	7.0–7.4	—	6.2–7.3	—	5.8–6.0	—	6.13	5.10
Ileum	5.7–5.9	—	7.5	—	6.0–6.7	—	5.93	5.94
Cecum	5.5–7.5	—	6.4	—	4.9–5.1	—	6.58	5.90
Colon[c]	7.8	6	6.5	—	5.0–5.9	—	5.88–6.23	5.51–5.77
Rectum/feces	—	—	6.2	—	5.5	—	—	—
Bile								
Stomach	~0	~0	—	—	—	—	—	—
Small intestine	3	15	5	—	—	—	20	—
Colon[c]	0.11	0.59	—	—	—	—	—	—

[a] References 3 and 14.
[b] Rat data from References 89 and 90.
[c] Human colon values from Reference 83.

6.3.2.1 *Stomach.*

In humans, in the fasted state, the pH in the stomach after the administration of 250 ml of water is 1.2–7.4 (median 1.7). In the fed state, the pH in the stomach increases to about 7 and gradually decreases to the normal range within 1.5 h [46]. The concentrations of Cl^- and Na^+ ions in the stomach are 102 and 68 mM, respectively [84]. The stomach pH is slightly higher in females than in males (2.2 vs 2.8) [82].

In dogs, the gastric pH is highly variable due to lower basal secretion of HCl (0.1 mEq/h) than in humans (2–5 mEq/h). Therefore, a pretreatment to control the stomach pH is often used [85, 86]. Pentagastrin injection has been most often used to achieve a low pH. An H2 blocker is often used to keep the stomach pH neutral [87]. When a pH modulator is used, it is important to avoid drug–drug interaction in the metabolic and excretion processes. In the fed state, the pH initially increases to ca. 4; however, it immediately drops to ca. 1.2 [88].

In monkeys, the stomach pH is similar to that in humans [45]. In rats, the stomach pH is 3–5 [1].

6.3.2.2 *Small Intestine.*

In humans in the fasted state, the pH values of the bulk fluid in the duodenum and jejunum are 6.2–7.0 and 6.8, respectively. In the fed state, the pH is slightly lower than that in the fasted state, that is, 5.9.

The buffer concentration is also an important factor that determines the solid surface pH of a drug (Section 2.3.3). The main buffer species in the intestine is sodium carbonate. The concentration of carbonate in the human intestine was reported to be 6.7 mM in the fasted state. The concentrations of Cl^- and Na^+ ions in the jejunum are 126 and 142 mM, respectively [84].

6.3.2.3 *Colon.*

The pH in the human ascending colon is 7.8 and 6.0 in the fasted and fed states, respectively [83]. The mean buffer capacity is 21.4 and 37.7 mmol/l/ΔpH in the fasted and fed states, respectively.

6.3.3 Microclimate pH

The microclimate pH is the pH at the epithelial membrane surface. This pH is lower than that of the luminal bulk fluid. In biopharmaceutical modeling, the microclimate pH should be used when calculating the membrane permeability of a drug, whereas the bulk fluid pH should be used when calculating the solubility and dissolution rate in the bulk fluid.

6.3.3.1 *Small Intestine.*

The acid microclimate pH exists adjacent to the epithelial membrane surface [91]. The pH is ca. 0.5 units lower than the average bulk fluid and is ca. 6.0–6.5. This microclimate pH is maintained constant by the Na^+/H^+ antiporter. A perturbation of the bulk fluid pH from 3 to 10 did not alter the microclimate pH (Fig. 6.16) [92]. The microclimate pH affects the passive diffusion of acid and base drugs as suggested by the pH partition theory. In addition, this microclimate pH is also important for PEP-T1 and OATP transporters, as the pH gradient between the microclimate pH and cytosol pH is the
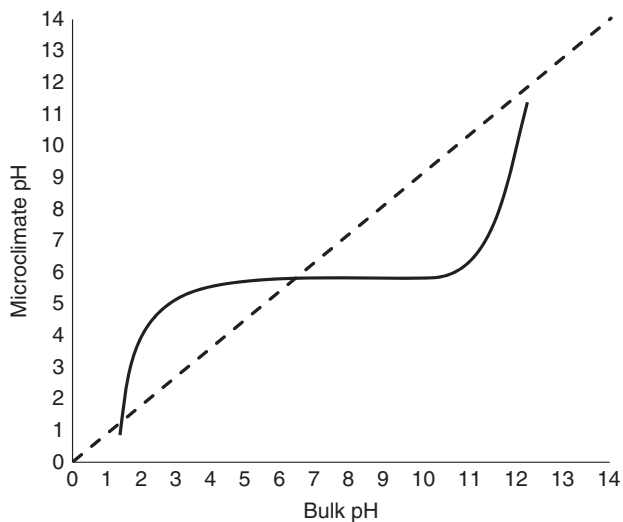
Figure 6.16   Relationship between bulk phase and microclimate pHs. Microclimate pH showed little change when the bulk pH was changed between 3.0 and 10.0. Beyond this range, there was a precipitous drop or rise in microclimate pH [92].

energy source for these transporters. Because the microclimate pH is maintained constant against pH perturbation in the bulk fluid, the membrane permeability of a drug should be insensitive to the change in the bulk pH [93, 94], for example, changes caused by food intake.

6.3.3.2   Colon.   The acid microclimate pH is also maintained in the colon [95, 96]. In humans and rats, the microclimate pH was 6.4–6.7 when the luminal pH was changed from 6.1 to 7.6.

6.3.4   Bile Micelles

Bile micelles not only increase the solubility and dissolution rate of a drug but also decrease the unbound drug fraction and the effective permeability [97–103]. The concentration of bile micelles has large species differences and fed/fasted state differences. The structures of a bile acid is shown in Figure 6.17. The surface of
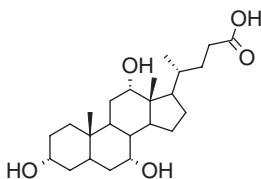

Figure 6.17   Chemical structure of bile acid.

the bile micelles is negatively charged because of the presence of sulfate (SO_3^-) or carboxylate (COO^-) group. Therefore, both lipophilicity and the charge of a drug affect bile-micelle binding. Another interesting feature of bile acids is that all hydroxyl groups are located on the same face of the cholesterol plane. This could result in a somewhat different behavior of bile acids (such as no distinct critical micelle concentration) from the regular surfactants.

6.3.4.1   Stomach. The bile concentration in the stomach is almost negligible. However, there is a small portion of surfactant that is enough to work as wetting agent [105].

6.3.4.2   Small Intestine. In humans, the average bile salt concentration in the jejunum is ca. 3 mM in the fasted state and ca. 5–15 mM in the fed state. However, the bile concentration shows a great deal of individual variation (Fig. 6.18) [104]. The bile salt/phospholipid ratio is ca. 4:1. In the fed state, the concentration and the composition of the drug-solubilizing component in the intestinal fluid changes as the digestion of food progresses. In Table 7.2, the snapshots of the intestinal fluid mimicking each digestion state are summarized. As water absorption occurs, the bile-micelles are concentrated. Therefore, the bile-micelle concentration might be slightly higher in the jejunum than in the duodenum [89, 106] (Fig. 6.19). Most of the bile acid is reabsorbed in the ileum mainly by a bile acid transporter, namely, ASBT (apical sodium-dependent bile acid transporter;
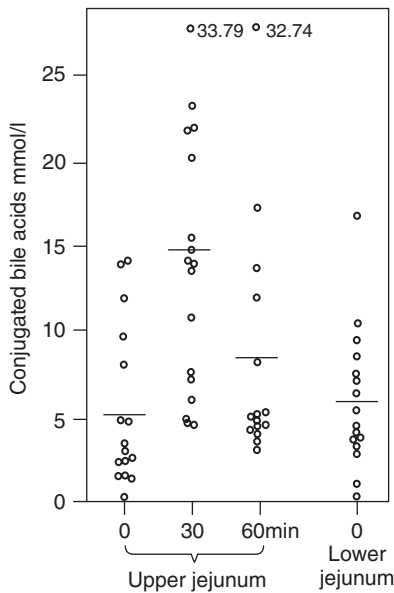

Figure 6.18   Bile concentration in humans in the fasted and fed states. *Source*: Adapted from Reference 104 with permission.

SLC10A2), which is critical for enterohepatic circulation of bile acids by mediating its absorption at the apical membranes of enterocytes [107]. This reduces the concentration of bile-micelles at the end of ileum and increases the unbound fraction of a drug, resulting in an increase in both the effective permeability in the ileum and bimodal absorption [108] (Section 13.6.3).

The bile-micelle concentration in the fed state depends on the food components [109]. The secretion of bile-micelles into the duodenum is stimulated by the lipids [110]. The long-chain triglycerides (LCTs) induce higher bile acid secretion than medium-chain triglycerides (MCTs). MCTs do not induce gallbladder contraction, whereas LCTs do [110]. On the other hand, carbohydrates do not stimulate bile secretion but increase the agitation in the GI tract [111].
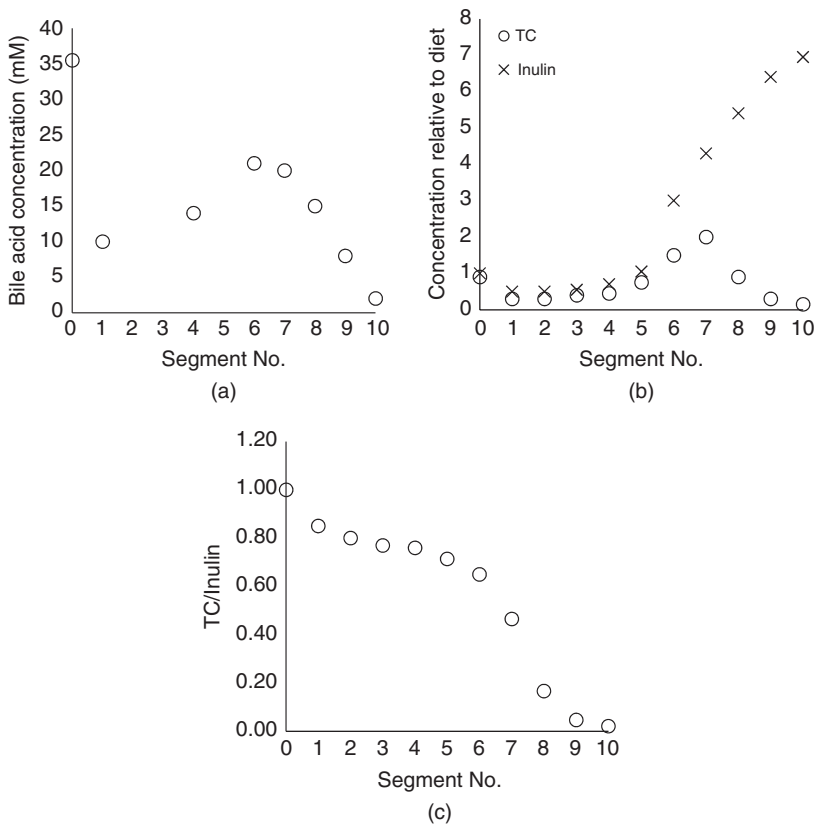
Figure 6.19 Regional bile concentration down the length of the small intestine of rats. (a) The concentration of conjugated bile acid in rats. Rats were allowed to eat ad lib. The time zero point is the bile acid concentration in the hepatic bile. (b) and (c) Taurocholic acid (TC) and inulin concentrations relative to diet. Rats were prepared surgically by ligation of the common hepatic duct; after recovery (24 h), these animals were intragastrically fed with a liquid diet containing (TC)-^{14}C (10 μmol/ml) and inulin-^{3}H. *Source*: Replotted from Reference 89.

In dogs, bile acid concentrations in the fasted and fed states were reported to be 4.9 (2.4–9.39 mM, $N = 3$) and 15.9 mM (12.8–18.0 mM, $N = 3$), respectively [112].

Rats lack the gallbladder and the bile continuously flows into the GI tract. The average bile salt concentration in the jejunum is ca. 15–20 mM [89].

6.3.4.3   Colon. As most of the bile is reabsorbed at the end of ileum, the bile concentration is very small in the colon [83]. Mean total bile acid concentration is 0.12 and 0.59 mM in the fasted and fed states, respectively.

6.3.5   Enzymes and Bacteria

Pepsin can degrade some drugs with amide and ester groups. In the fasted human stomach, the pepsin concentration ranges between 0.1 and 1.3 mg/ml. In the fed stomach, the pepsin concentration ranges from 0.26 to 1.72 mg/ml [5].

Lipase also plays important roles in the oral absorption of a drug from a lipid-based formulation (Section 11.3). Lipase activity in the fed stomach is from 11.4 to 43.9 U/ml [5]. Some drugs and formulations are degraded by the bacteria in the GI tract, for example, sulfasalazine (Table 6.10).

6.3.6   Viscosity, Osmolality, and Surface Tension

Osmolality can affect the disintegration of a formulation ([5] and references therein). Gastric osmolality in the fasted state is in the range of 29–276 mOsm/kg. After a meal, the median value in the stomach was found to be 559 mOsm/kg after 30 min and 217 mOsm/kg after 210 min. In the upper small intestine, osmolality values range from 124 to 278 mOsm/kg in the fasted state and 250 to 367 mOsm/kg in the fed state.

Viscosity of the intestinal fluid has not been reported. The viscosity of water at 37°C is 0.691 cP, while typical meals have viscosities in the range of 10 to 100,000 cP.

Surface tension of the fluid affects the wetting speed of drugs and excipients. The lower the surface tension, the higher the wetting speed. The surface tension of water is 70 mN/m at 37°C. Gastric surface tension values in the fasted and fed states range from about 41 to 46 and 30 to 31 mN/m, respectively [5]. In

TABLE 6.10   Bacterial Population in the Lower Bowel in Humans

	Distal Ileum	Cecum	Feces
Enterobacteria	3.3	6.2	7.4
Enterococci	2.2	3.6	5.6
Clostridia	<2	3.0	5.4
Lactobacilli	<2	6.4	6.5
Bacteroides	5.7	7.8	9.8
Gram-positive nonsporing anaerobes	5.8	8.4	10

the upper small intestine, surface tension values range from 28 to 46 mN/m in the fasted state and from 27 to 37 mN/m in the fed state. Surface tension in the colon is significantly lower than that of water, 39 and 43 mN/m in the fasted and fed states, respectively.

6.4   TRANSPORTERS AND DRUG-METABOLIZING ENZYMES IN THE INTESTINE

6.4.1   Absorptive Drug Transporters

6.4.1.1   PEP-T1. As an absorptive influx transporter, PEP-T1 is well known to contribute to oral absorption of some drugs, especially antibiotics.

In humans, the mRNA level of PEP-T1 is similar between the duodenum and ileum, but almost null in the colon [107, 113]. The mRNA level of PEP-T1 is similar between humans and rats [114].

6.4.1.2   OATP. OATP is an influx transporter located on the apical membrane. Fexofenadine is one of the most well-characterized OATP substrates. In humans, the mRNA level of OATP is similar in the duodenum, ileum, and colon [113].

6.4.2   Efflux Drug Transporters

6.4.2.1   P-gp. P-gp is an efflux transporter located on the apical membrane. P-gp is a 170-kd transmembrane glycosylated protein and the gene product of MDR1. P-gp has a few binding sites for substrates [115].

A proposed efflux mechanism of P-gp is shown in Figure 4.20 (the vacuum cleaner mechanism). A substrate first partitions into the lipid bilayer and then enters the cavity of the enzyme from a portal opening into the lipid bilayer.

In humans, the P-gp expression level is ca. 1.5-fold higher in the ileum than in the jejunum [116] (Fig. 6.20). This trend is also found in the functional activity level [117] and mRNA level [118]. The interindividual variation of the P-gp expression level is within twofold, which is smaller than that for CYP3A4 (>10-fold) [116].

The apparent K_m values of P-gp showed significant species differences, whereas efflux ratio has lesser species differences [119]. In addition, the degree and tendency of these species differences was different between cyclosporine and diltiazem. These results suggest that the effect of P-gp on oral absorption in humans cannot be simply quantitatively extrapolated from that in animals.

6.4.3   Drug-Metabolizing Enzymes

6.4.3.1   CYP3A4. CYP3A4 is the dominant CYP species in the intestinal wall (Fig. 6.21) [120]. The total amount of CYP3A in the intestinal wall is about 1% of that in the liver. However, intestinal CYP3A could significantly reduce the bioavailability of a drug.
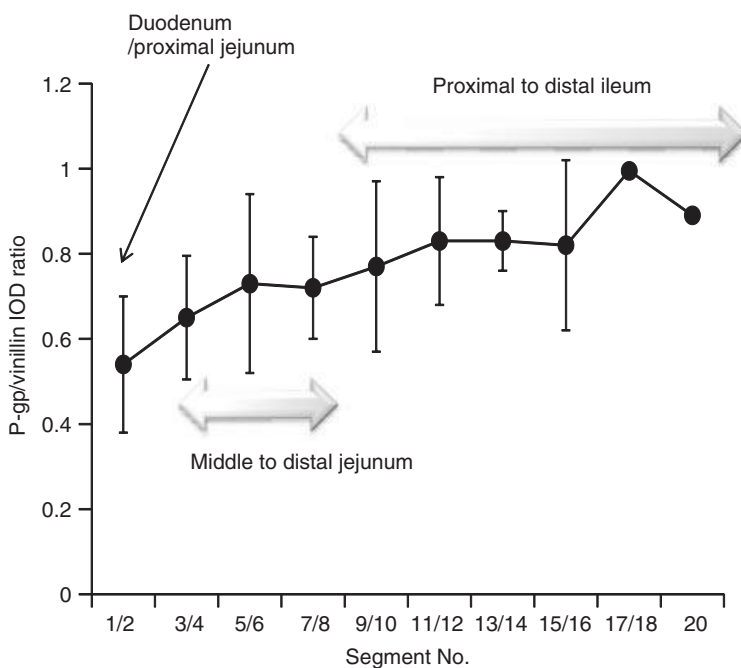
Figure 6.20   6.20 P-gp expression level along the GI tract. P-gp content (P-gp/villin integrated optical density (IOD) ratio, normalized to the maximum value) for each segment of the human small intestine are shown. Segment 1/2, duodenum/proximal jejunum; segments 3/4, 5/6, and 7/8, middle to distal jejunum; and 9/10-20, proximal to distal ileum. Segments 1/2-13/14, $n = 4$; 15/16, $n = 3$; 17/18, $n = 2$; and 20, $n = 1$. *Source*: Replotted from Reference 116.
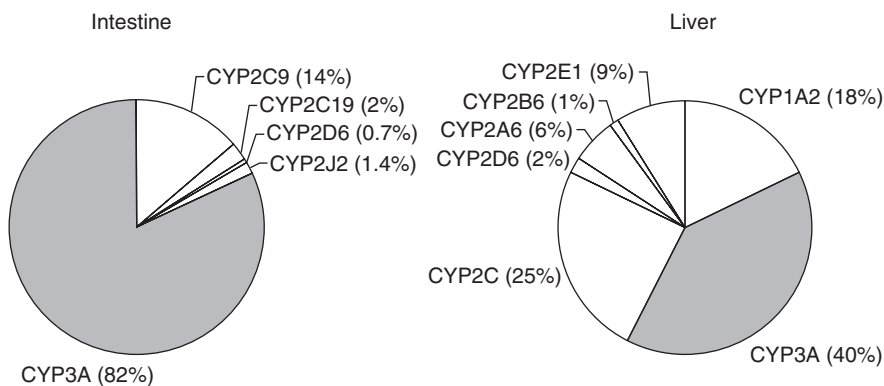

Figure 6.21   CYP in the small intestine and liver [120].

The mRNA expression level of CYP3A4 is much higher in the small intestine than that in the colon, ca. 100:1 [118]. A higher bioavailability from the colon compared to oral administration was observed for CYP3A4 substrates, such as atrovastatin and nisoldipine [15].

Significant species differences have been reported in the metabolic enzymes in the intestinal wall. CYP3A4 activity is much higher in monkeys than in humans [11].

6.4.3.2 *Glucuronyl Transferase and Sulfotransferase.* Glucuronyl trans-ferases catalyze the conjugation of glucuronic acid onto the phenol, hydroxyl, and carboxylic acid groups of a drug. Glucuronyl transferases activity is similar in the duodenum, jejunum, and ilium, but significantly lower in the colon [121]. Sulfonyl transferases catalyze sulfonation of phenol and hydroxyl groups of a drug, such as terbutaline and fenoterol [122–124].

6.5   INTESTINAL AND LIVER BLOOD FLOW

6.5.1   Absorption Sites Connected to Portal Vein

Drug absorption into the portal circulation can occur down the length of the GI tract to the superior rectal vein. Absorption from the lower region of the rectum (middle and inferior rectal veins) bypasses the portal circulation [125].

6.5.2   Villous Blood Flow (Q_{villi})

The villous blood flow (Q_{villi}) is used to calculate the extent of intestinal first-pass metabolism by the Q_{gut} model (Section 4.10). The blood supply to the small intestine is provided by the superior mesenteric artery (Fig. 6.22). The mucosal blood flow is about 80% of the total mesenteric flow of 37.2 l/h, about 60% of which then pours into the epithelial cells of the villi. Therefore, the villous blood flow rate is about 18 l/h (4.3 ml/min/kg) [127]. This rate is significantly higher than the maximum permeation clearance, $SA_{GI} \times P_{eff} = 300$ cm$^2 \times 5 \times 10^{-4}$cm/s $= 0.13$ ml/min/kg. Therefore, it is unlikely that the blood flow would become a rate-limiting step of intestinal wall permeation. Food intake increases the blood flow by ca. 100% as the chyme reaches each site (Fig. 6.23).

6.5.3   Hepatic Blood Flow (Q_h)

The hepatic blood flow rate (Q_h) is used to calculate Fh. Q_h is ca. 21, 84, 31, and 44 ml/min/kg for humans, rats, dogs, and monkeys, respectively [128]. Food intake increases the hepatic blood flow by 34% [129]. The hepatic blood flow shows a circadian rhythm (Fig. 6.24) [130]. Pharmacokinetics of high clearance drugs, for example, propranolol, isosorbide-5-mononitrate, and nifedipine [131–133], were shown to be dependent on the time of day at which they were administered.
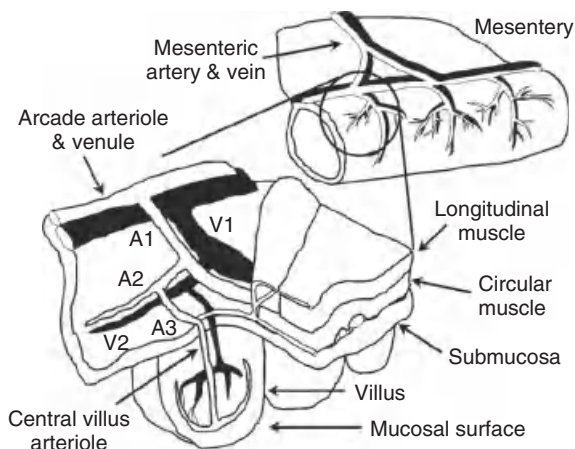
Figure 6.22   Intestinal blood flow. Outline of the intestinal microvasculature emphasizing the mucosal blood supply with the inflow (A1), transitional (A2), and premucosal (A3) arteriolar structure as well as outflow (V1) and transitional (V2) venules. *Source*: Adapted from Reference 126 with permission.

6.6   PHYSIOLOGY RELATED TO ENTEROHEPATIC RECIRCULATION

Physiology of the liver related to the enterohepatic recirculation is discussed in this section. The first-pass drug metabolism in the liver significantly affects the bioavailability of many drugs. However, it is not covered in this book, as it would be beyond the scope of this book.

6.6.1   Bile Secretion

After an overnight fast, the gallbladder volume is 17–25 ml [134]. In the fasted state, ca. 30% of the secreted bile directly excretes into the duodenum and ca. 70% accumulates in the gallbladder. The average bile secretion from the liver is 500–600 ml/d in humans [135]. The gallbladder fills to its maximum capacity (40–70 ml) in approximately 6 h [136]. More than 90% water is reabsorbed in the gallbladder.

The gallbladder is not static during the fasted state. Secretion of bile into the duodenum occurs periodically as part of the MMC. During the interdigestive period, the volume of the gallbladder decreases to up to 30–35%, starting in the first half of MMC phase II.

On the sight, smell, or ingestion of food, the bile stored in the gallbladder is released into the duodenum. Food intake causes the gallbladder to be emptied up to 75%. After ingestion of a meal, fats, and proteins, endogenous neurohormones such as cholecystokinin (CCK) and secretin are released by the endocrine cells of the small intestine. CCK, acting on the CCK-A type receptors of smooth muscle fibers, contracts the gallbladder and relaxes the sphincter of Oddi [136].
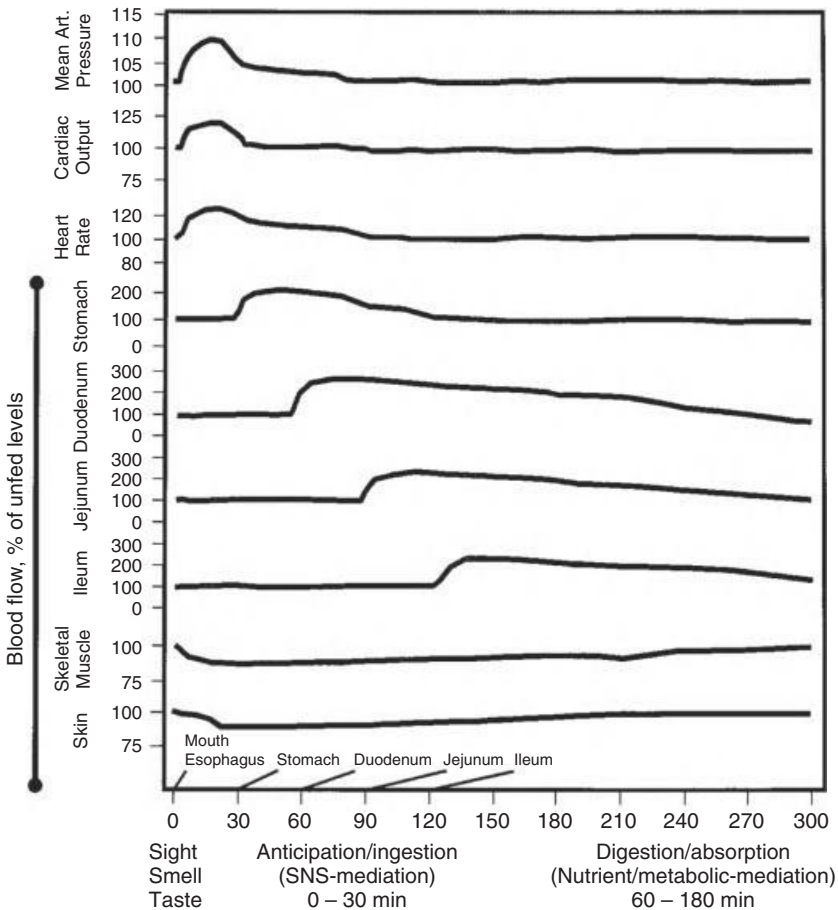
Figure 6.23 Effect of food on the gastrointestinal blood flow. Blood flow increases in specific organs as digestive chyme reaches that organ. Indications along the time axis mark the point at which the chyme reaches the stomach, duodenum, jejunum, and ileum to initiate the metabolically mediated digestion and absorption stages of postprandial hyperemia. *Source*: Adapted from Reference 126 with permission.

6.6.2   Mass Transfer into/from the Hepatocyte

6.6.2.1   Sinusoidal Membrane (Blood to Hepatocyte). Mass transfer of drugs from the circulation into the hepatocyte has been intensively investigated. The majority of small lipophilic compounds enter the hepatocyte via the sinusoidal membrane by simple passive diffusion (Fig. 6.25). However, some hydrophilic drugs, such as pravastatin, can enter the hepatocyte by carrier-mediated transport across the sinusoidal membrane [125] (cf. many hydrophilic drugs are usually excreted into the urine via the kidney). The role of plasma protein binding on the uptake of highly protein-bound drugs has been
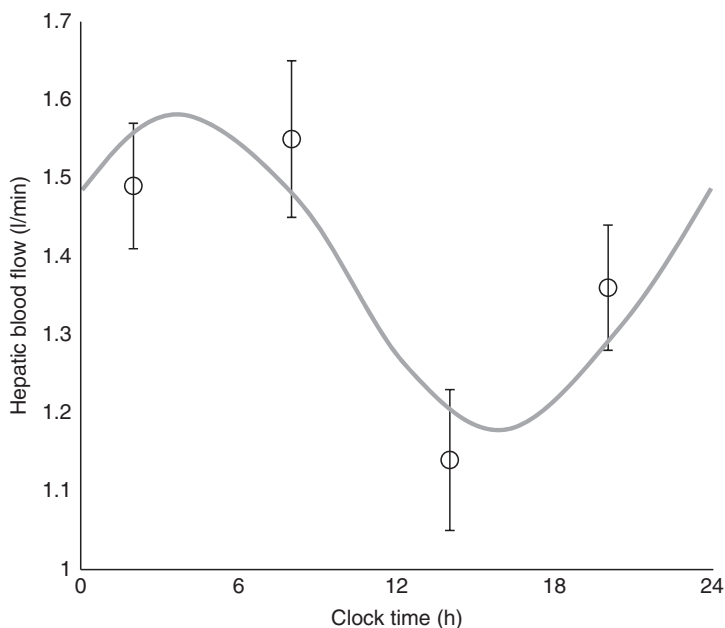
Figure 6.24 Circadian rhythm in hepatic blood flow in humans estimated from indocyanine green clearance. Data were fitted by a cosine function with a period of 24 h. Values are shown as mean and SE ($n = 10$). *Source*: Replotted from Reference 130.

a controversial issue. Recent studies in this area have provided evidence that uptake may occur from both the unbound and protein-bound fractions [125].

6.6.2.2   *Canalicular Membrane (Hepatocyte to Bile Duct).* Hepatobiliary elimination requires active efflux transporters to move drugs from hepatocytes into the canalicular space [137]. As the volume of biliary fluid is very small, biliary excretion becomes significant only when the drug concentration in the bile is higher than that in the plasma. The bile/plasma concentration ratio is most commonly between 10 and 1000.

Biliary elimination of anionic compounds is mediated by MRP2, whereas bile salts are excreted by a bile salt export pump (BSEP). P-glycoprotein, the multidrug resistance (MDR) gene product, is exclusively located on the canalicular membrane of hepatocytes [125].

6.7   NASAL

The morphology of the nasal cavity has large species differences (Table 6.11; Fig. 6.26). Rats and dogs have significantly larger surface area/body weight than humans. Drugs applied to the mucous lining of the nasal cavity move toward the nasopharynx, eventually entering into the GI tract. This mechanism is called
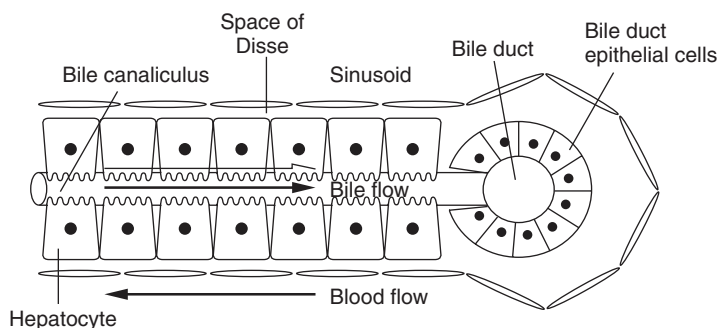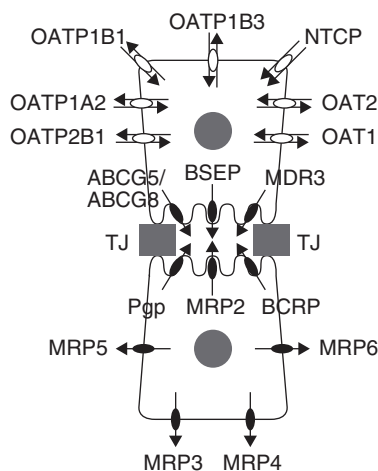
Figure 6.25 Microanatomy of the hepatobiliary tract. (a) At the cellular level, hepatocytes are organized in cords and bathed by sinusoidal blood from the basolateral side; the canalicular membranes form the bile canaliculi. Bile flows in the opposite direction to blood and drains into bile ducts and (b) Transport proteins involved in the uptake and excretion of drugs. Adjacent hepatocytes form tight junctions (TJs) to seal the canalicular domain from the basolateral domain. *Source*: Adapted from Reference 136 with permission.

TABLE 6.11   Nasal Cavity

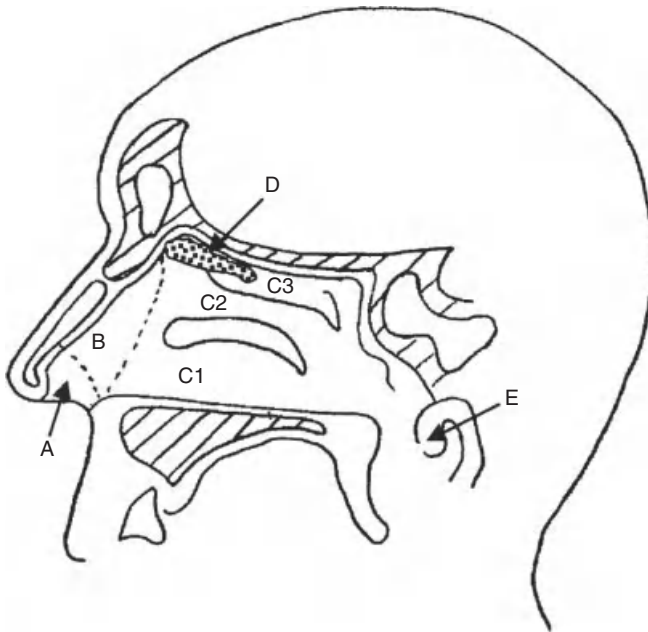|	Body Weight, kg	Length, cm	Surface Area, cm^2	Fluid Volume, ml	MMC $T_{1/2}$, min	Surface Area/Body Weight, cm^2/ kg
Rat	0.25	2.3	10.4–14	0.013	5	49
rabbit	3	4.7	61.9	0.058	10	21
Dog (beagle)	10	10	220.7	0.207	20	22
Rhesus monkey	7	5.3	61.6	0.058	10	9
Man	70	7–8	160–181	0.15	15	2

Figure 6.26   Nasal cavity. The (a) nasal vestibule; (b) atrium; (c) respiratory area: inferior turbinate (C1), middle turbinate (C2), and superior turbinate (C3); (d) the olfactory region; and (e) nasopharynx. *Source*: Adapted from Reference 139 with permission.

mucociliary clearance. Substances administered intranasally are rapidly cleared from the human nose, with a clearance half-life of approximately 21 min [138]. The mucous blanket is approximately 5 μm thick (Fig. 6.27). Together with the limited volume that can be administered, the nasal administration presents formulation challenges for poorly soluble drugs. Owing to the direct access to the circulation, the hepatic first-pass metabolism is avoided.

6.8   PULMONARY

6.8.1   Fluid in the Lung

The large absorptive surface at the air interface in the lung is covered by an extremely small volume of fluid (10–20 ml) [140]. The alveolar surface is coated with a liquid layer of 0.2 μm. This fluid is rich in surfactants, comprising approximately 90% lipids and 10% proteins. Within the lipid fraction, the most abundant component is 1,2-dipalmitoyl phosphatidylcholine (ca. 45%). The blood flow lies just beneath the absorptive surface.

6.8.2   Mucociliary Clearance

Ciliated epithelial cells cover 30–65% of the airway epithelial cells in the human respiratory tract. Each ciliated cell has about 200 cilia of 5–6 μm [141]. As the
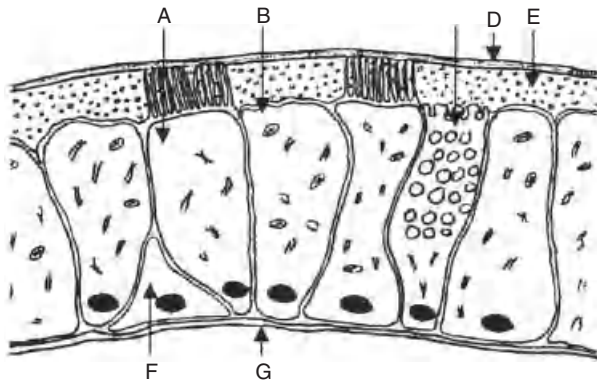
Figure 6.27 Cell types of the nasal epithelium showing ciliated cell (A), nonciliated cell (B), goblet cell (C), gel mucous layer (D), sol layer (E), basal cell (F), and basement membrane (G). *Source*: Adapted from Reference 139 with permission.

airway becomes smaller, the distribution of ciliary epithelial cells decreases from 53% in the trachea to 45% in the first airway generation to 15% in the fifth airway generation. The mucociliary clearance rate is about 10 mm/min in the trachea.

6.8.3   Absorption into the Circulation

Aerosol particles in the alveolar space and terminal airway can be removed by absorptive or nonabsorptive processes [141]. Drug absorption from the lungs occurs primarily across the alveolar epithelium. The human lungs contain about 3×10^8 alveoli and have a total surface area of 130 m^2. Each alveolus contains 100 alveolar macrophages, which typically phagocytose 50–70% of particles within 2 h. As the geometric diameters of the particles increase above about 5 μm, removal by phagocytosis becomes less efficient. The adhesion of particles to alveolar macrophages is mediated through electrostatic interaction or receptor mediation, and particles are then internalized through surface cavitation or vacuole and pseudopod formation. Depending on the nature of the particles, internalization is followed by further metabolization or digestion by peptidases in the case of proteins.

6.9   SKIN

The transdermal permeation of most drugs is limited by the stratum corneum (SC) [142, 143]. The thickness of the SC is different at each body part, about 15 μm in the abdominal skin and 10 μm in the dorsal skin. The pH near the surface of the skin is about 5. The structure of the SC is represented by the brick and mortar model, in which keratin-filled cells (corneocytes, brick) are embedded within intercellular lipids (mortar) (Fig. 6.28). The intercellular lipids
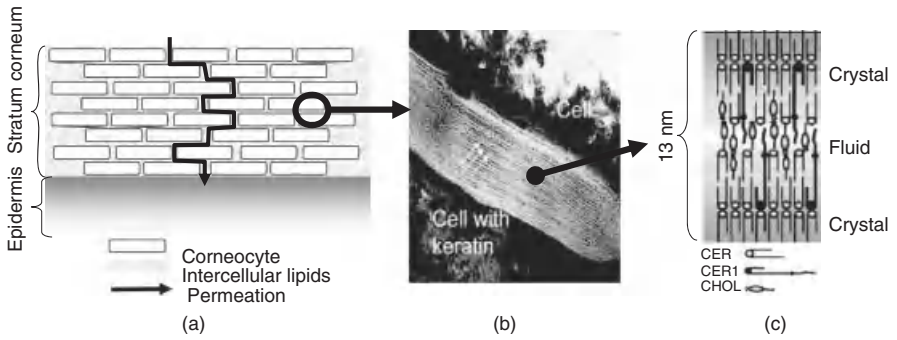
Figure 6.28 Schematic of the stratum corneum. *Source*: Adapted from Reference 142 with permission.
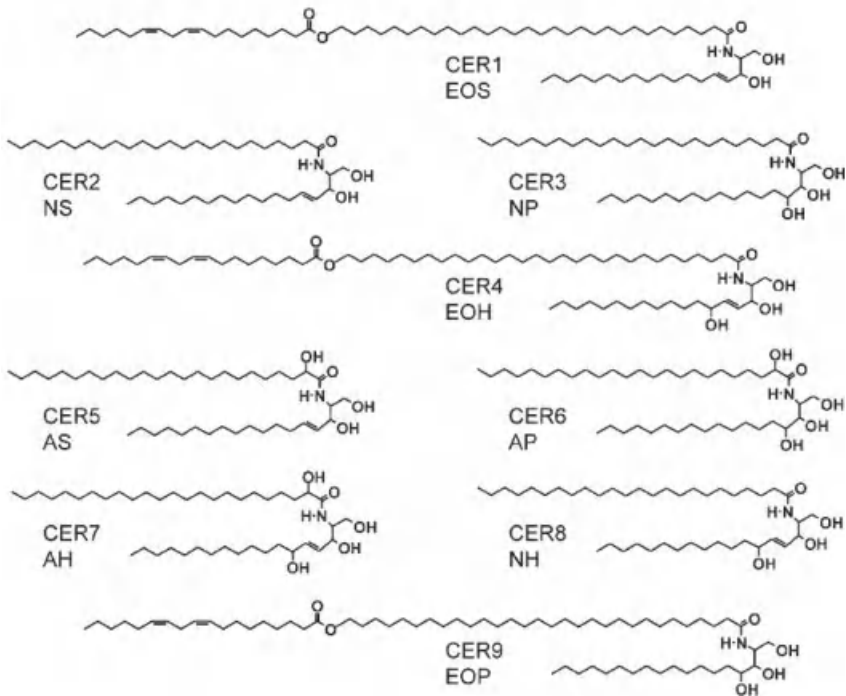

Figure 6.29 Chemical structure of the stratum corneum components. *Source:* Adapted from Reference 45 with permission.

form a lamellar structure, which orients parallel to the corneocyte surface. The primary transport pathway for most drugs traversing the SC is the intercellular lamellar lipid region. The path length relative to the thickness of the SC is about 13 due to the tortuous pathway.

The intercellular lipids are mainly composed of free fatty acids (FFAs, 10–15%), cholesterol (25%), sterol esters (5%), and ceramides (50%). The phase behavior of the lamellar lipid is different from that of the lipid bilayer that is mainly composed of phospholipids. In the SC, a crystalline part is predominantly present, while most probably a subpopulation of lipids form a more fluidic part (Fig. 6.29) [144].

REFERENCES

1. Kararli, T.T. (1995). Comparison of the gastrointestinal anatomy, physiology, and biochemistry of humans and commonly used laboratory animals. *Biopharm. Drug Dispos.*, 16, 351–380.

2. DeSesso, J.M., Jacobson, C.F. (2001). Anatomical and physiological parameters affecting gastrointestinal absorption in humans and rats. *Food Chem. Toxicol.*, 39, 209–228.

3. DeSesso, J.M., Williams, A.L. (2008). Contrasting the gastrointestinal tracts of mammals: factors that influence absorption. *Annu. Rep. Med. Chem.*, 43, 353–371.

4. McConnell, E.L., Fadda, H.M., Basit, A.W. (2008). Gut instincts: explorations in intestinal physiology and drug delivery. *Int. J. Pharm.*, 364, 213–226.

5. Mudie, D.M., Amidon, G.L., Amidon, G.E. (2010). Physiological parameters for oral delivery and in vitro testing. *Mol. Pharm.*, 7(5), 1388–1405.

6. Davies, B., Morris, T. (1993). Physiological parameters in laboratory animals and humans. *Pharm. Res.*, 10, 1093–1095.

7. Dressman, J.B., Amidon, G.L., Reppas, C., Shah, V.P. (1998). Dissolution testing as a prognostic tool for oral drug absorption: immediate release dosage forms. *Pharm. Res.*, 15, 11–22.

8. Horter, D., Dressman, J.B. (2001). Influence of physicochemical properties on dissolution of drugs in the gastrointestinal tract. *Adv. Drug Deliv. Rev.*, 46, 75–87.

9. Sutton, S.C. (2004). Companion animal physiology and dosage form performance. *Adv. Drug Deliv. Rev.*, 56, 1383–1398.

10. Martinez, M., Amidon, G., Clarke, L., Jones, W.W., Mitra, A., Riviere, J. (2002). Applying the biopharmaceutics classification system to veterinary pharmaceutical products. Part II. Physiological considerations. *Adv. Drug Deliv. Rev.*, 54, 825–850.

11. Takahashi, M., Washio, T., Suzuki, N., Igeta, K., Yamashita, S. (2010). Investigation of the intestinal permeability and first-pass metabolism of drugs in cynomolgus monkeys using single-pass intestinal perfusion. *Biol. Pharm. Bull.*, 33, 111–116.

12. Lin, J.H., Chiba, M., Baillie, T.A. (1999). Is the role of the small intestine in first-pass metabolism overemphasized? *Pharmacol. Rev.*, 51, 135–158.

13. Masaoka, Y., Tanaka, Y., Kataoka, M., Sakuma, S., Yamashita, S. (2006). Site of drug absorption after oral administration: assessment of membrane permeability and luminal concentration of drugs in each segment of gastrointestinal tract. *Eur. J. Pharm. Sci.*, 29, 240–250.

14. Diakidou, A., Vertzoni, M., Goumas, K., Soderlind, E., Abrahamsson, B., Dress-man, J., Reppas, C. (2009). Characterization of the contents of ascending colon to which drugs are exposed after oral administration to healthy adults. *Pharm. Res*., 26, 2141–2151.

15. Tannergren, C., Bergendal, A., Lennernas, H., Abrahamsson, B. (2009). Toward an increased understanding of the barriers to colonic drug absorption in humans: impli-cations for early controlled release candidate assessment. *Mol. Pharm*., 6, 60–73.

16. Trotter, P.J., Storch, J. (1991). Fatty acid uptake and metabolism in a human intesti-nal cell line (Caco-2): comparison of apical and basolateral incubation. *J. Lipid Res*., 32, 293–304.

17. Proulx, P. (1991). Structure-function relationships in intestinal brush border mem-branes. *Biochim. Biophys. Acta*, 1071, 255–271.

18. Dias, V.C., Wallace, J.L., Parsons, H.G. (1992). Modulation of cellular phospholipid fatty acids and leukotriene B4 synthesis in the human intestinal cell (CaCo-2). *Gut*, 33, 622–627.

19. Lipka, G., Op den Kamp, J.A., Hauser, H. (1991). Lipid asymmetry in rabbit small intestinal brush border membrane as probed by an intrinsic phospholipid exchange protein. *Biochemistry*, 30, 11828–11836.

20. Verkleij, A.J., Zwaal, R.F., Roelofsen, B., Comfurius, P., Kastelijn, D., van Dee-nen, L.L. (1973). The asymmetric distribution of phospholipids in the human red cell membrane. A combined study using phospholipases and freeze-etch electron microscopy. *Biochim. Biophys. Acta*, 323, 178–193.

21. Marrink, S.J., Berendsen, H.J.C. (1996) Permeation process of small molecules across lipid membranes studied by molecular dynamics simulations. *J. Phys. Chem*., 100, 16729–16738.

22. Marrink, S.-J., Berendsen, H.J.C. (1994). Simulation of water transport through a lipid membrane. *J. Phys. Chem*., 98, 4155–4168.

23. Anderson, J.M. (2001). Molecular structure of tight junctions and their role in epithe-lial transport. *News Physiol. Sci*., 16, 126–130.

24. Sugano, K., Takata, N., Machida, M., Saitoh, K., Terada, K. (2002). Prediction of passive intestinal absorption using bio-mimetic artificial membrane permeation assay and the paracellular pathway model. *Int. J. Pharm*., 241, 241–251.

25. Sugano, K. (2009). Theoretical investigation of passive intestinal membrane perme-ability using Monte Carlo method to generate drug like molecule population. *Int. J. Pharm*., 373, 55–61.

26. He, Y., Murby, S., Warhurst, G., Gifford, L., Walker, D., Ayrton, J., Eastmond, R., Rowland, M. (1998). Species differences in size discrimination in the paracellular pathway refrected by oral bioavailability of poly(ethylene glycol) and D-peptides. *J. Pharm. Sci*., 87, 626–633.

27. Avdeef, A. (2010). Leakiness and size exclusion of paracellular channels in cultured epithelial cell monolayers-interlaboratory comparison. *Pharm. Res*., 27, 480–489.

28. Adson, A., Ruab, T.J., Burton, P.S., Barsuhn, C.L., Hilgers, A.R., Audus, K.L., Ho, N.F.H. (1994). Quantitative approaches to delineate paracellular diffusion in cultured epithelial cell monolayers. *J. Pharm. Sci*., 83, 1529–1530.

29. Adson, A., Burton, P.S., Ruab, T.J., Barsuhn, C.L., Audus, L., Ho, N.F.H. (1995). Passive diffusion of weak organic electolytes across Caco-2 cell monolayers: uncou-pling the contributions of hydrodynamic, transcellular and paracellular barriers. *Pharm. Res*., 84, 1197–1203.

30. Pade, V., Stavchansky, S. (1997). Estimation of the relative contribution of the transcellular and paracellular pathway to the transport of passively absorbed drugs in the Caco-2 cell culture model. *Pharm. Res*., 14, 1210–1215.

31. Sugano, K., Nabuchi, Y., Machida, M., Aso, Y. (2003). Prediction of human intestinal permeability using artificial membrane permeability. *Int. J. Pharm*., 257, 245–251.

32. Avdeef, A., Tam, K.Y. (2010). How well can the Caco-2/Madin-darby canine kidney models predict effective human jejunal permeability? *J. Med. Chem*., 53, 3566–3584.

33. Tam, K.Y., Avdeef, A., Tsinman, O., Sun, N. (2010). The permeation of amphoteric drugs through artificial membranes–an in combo absorption model based on paracellular and transmembrane permeability. *J. Med. Chem*., 53, 392–401.

34. Cone, R.A. (2009). Barrier properties of mucus. *Adv. Drug Delivery Rev*., 61, 75–85.

35. Allen, A., Flemstroem, G. (2005). Gastroduodenal mucus bicarbonate barrier: protection against acid and pepsin. *Am. J. Physiol*., 288, C1–C19.

36. Atuma, C., Strugala, V., Allen, A., Holm, L. (2001). The adherent gastrointestinal mucus gel layer: thickness and physical state in vivo. *Am. J. Physiol*., 280, G922–G929.

37. Doyle-McCullough, M., Smyth, S.H., Moyes, S.M., Carr, K.E. (2007). Factors influencing intestinal microparticle uptake in vivo. *Int. J. Pharm*., 335, 79–89.

38. Hodges, G.M., Carr, E.A., Hazzard, R.A., Carr, K.E. (1995). Uptake and translocation of microparticles in small intestine. Morphology and quantification of particle distribution. *Dig. Dis. Sci*., 40, 967–975.

39. Limpanussorn, J., Simon, L., Dayan, A.D. (1998). Transepithelial transport of large particles in rat: a new model for the quantitative study of particle uptake. *J. Pharm. Pharmacol*., 50, 753–760.

40. Norris, D.A., Puri, N., Sinko, P.J. (1998). The effect of physical barriers and properties on the oral absorption of particulates. *Adv. Drug Delivery Rev*., 34, 135–154.

41. Smyth, S.H., Feldhaus, S., Schumacher, U., Carr, K.E. (2008). Uptake of inert microparticles in normal and immune deficient mice. *Int. J. Pharm*., 346, 109–118.

42. Davis, S.S., Hardy, J.G., Fara, J.W. (1986). Transit of pharmaceutical dosage forms through the small intestine. *Gut*, 27, 886–892.

43. Hunt, J.N., Stubbs, D.F. (1975). The volume and energy content of meals as determinants of gastric emptying. *J. Physiol*., 245, 209–225.

44. Nimmo, W.S. (1976). Drugs, diseases and altered gastric emptying. *Clin. Pharmacokinet*., 1, 189–203.

45. Ikegami, K., Tagawa, K., Narisawa, S., Osawa, T. (2003). Suitability of the cynomolgus monkey as an animal model for drug absorption studies of oral dosage forms from the viewpoint of gastrointestinal physiology. *Biol. Pharm. Bull*., 26, 1442–1447.

46. Dressman, J. (1986). Comparison of canin and human gastrointestinal physiology. *Pharm. Res*., 3, 123–130.

47. Fadda, H.M., McConnell, E.L., Short, M.D., Basit, A.W. (2009). Meal-Induced Acceleration of Tablet Transit Through the Human Small Intestine. *Pharm. Res*., 26, 356–360.

48. Watts, P.J., Barrowb, L., Steedb, K.P., Wilsonb, C.G., Spillerc, R.C., Meliaa, C.D., Davies, M.C. (1992). The transit rate of different-sized model dosage forms through the human colon and the effects of a lactulose-induced catharsis. *Int. J. Pharm.*, 87, 215–221.

49. Hansen, M.B. (2002). Small intestinal manometry. *Physiol. Res.*, 51, 541–556.

50. Takahashi, T. (2007). Effects of food intake on interdigestive migrating motor complex (MMC). *Neurogastroenterology*, 10, 76–77.

51. Steffen, D., Physiological parameters relevant to dissolution testing, in: J. Dressman and J. Krämer (Eds.) Pharmaceutical Dissolution Testing, Informa Healthcare, Florida, 2005, pp. 127–191.

52. Pal, A., Indireshkumar, K., Schwizer, W., Abrahamsson, B., Fried, M., Brasseur James, G. (2004). Gastric flow and mixing studied using computer simulation. *Proc. Biol. Sci.*, 271, 2587–2594.

53. Dillard, S., Krishnan, S., Udaykumar, H.S. (2007). Mechanics of flow and mixing at antroduodenal junction. *World J. Gastroenterol.*, 13, 1365–1371.

54. Funakoshi, M. (2008). Chaotic mixing and mixing efficiency in a short time. *Fluid Dyn. Res.*, 40, 1–33.

55. Sugano, K. (2010). Aqueous boundary layers related to oral absorption of a drug: from dissolution of a drug to carrier mediated transport and intestinal wall metabolism. *Mol. Pharm.*, 7, 1362–1373.

56. Womack, W.A., Barrowman, J.A., Graham, W.H., Benoit, J.N., Kvietys, P.R., Granger, D.N. (1987). Quantitative assessment of villous motility. *Am. J. Physiol.*, 252, G250–G256.

57. Strocchi, A., Levitt, M.D. (1993). Role of villous surface area in absorption. Science versus religion. *Dig. Dis. Sci.*, 38, 385–387.

58. Mailman, D., Womack, W.A., Kvietys, P.R., Granger, D.N. (1990). Villous motility and unstirred water layers in canine intestine. *Am. J. Physiol.*, 258, G238–G246.

59. Janssen, P.W.M., Lentle, R.G., Asvarujanon, P., Chambers, P., Stafford, K.J., Hemar, Y. (2007). Characterization of flow and mixing regimes within the ileum of the brushtail possum using residence time distribution analysis with simultaneous spatio-temporal mapping. *J. Physiol.*, 582, 1239–1248.

60. Katori, N., Aoyagi, N., Terao, T. (1995). Estimation of agitation intensity in the GI tract in humans and dogs based on in vitro/in vivo correlation. *Pharm. Res.*, 12, 237–243.

61. Rostami-Hodjegan, A., Shiran, M.R., Tucker, G.T., Conway, B.R., Irwin, W.J., Shaw, L.R., Grattan, T.J. (2002). A new rapidly absorbed paracetamol tablet containing sodium bicarbonate. II. Dissolution studies and in vitro/in vivo correlation. *Drug Dev. Ind. Pharm.*, 28, 533–543.

62. Parojcic, J., Vasiljevic, D., Ibric, S., Djuric, Z. (2008). Tablet disintegration and drug dissolution in viscous media: paracetamol IR tablets. *Int. J. Pharm.*, 355, 93–99.

63. D'Arcy, D.M., Healy, A.M., Corrigan, O.I. (2009). Towards determining appropriate hydrodynamic conditions for in vitro in vivo correlations using computational fluid dynamics. *Eur. J. Pharm. Sci.*, 37, 291–299.

64. Crail, D.J., Tunis, A., Dansereau, R. (2004). Is the use of a 200ml vessel suitable for dissolution of low dose drug products? *Int. J. Pharm.*, 269, 203–209.

65. Kamba, M., Seta, Y., Kusai, A., Nishimura, K. (2002). Comparison of the mechanical destructive force in the small intestine of dog and human. *Int. J. Pharm.*, 237, 139–149.

66. Kamba, M., Seta, Y., Kusai, A., Ikeda, M., Nishimura, K. (2000). A unique dosage form to evaluate the mechanical destructive force in the gastrointestinal tract. *Int. J. Pharm.*, 208, 61–70.

67. Kamba, M., Seta, Y., Kusai, A., Nishimura, K. (2001). Evaluation of the mechanical destructive force in the stomach of dog. *Int. J. Pharm.*, 228, 209–217.

68. Kamba, M., Seta, Y., Takeda, N., Hamaura, T., Kusai, A., Nakane, H., Nishimura, K. (2003). Measurement of agitation force in dissolution test and mechanical destructive force in disintegration test. *Int. J. Pharm.*, 250, 99–109.

69. Chiou, W.L. (1994). Effect of 'unstirred' water layer in the intestine on the rate and extent of absorption after oral administration. *Biopharm. Drug Dispos.*, 15, 709–717.

70. Levitt, M.D., Furne, J.K., Strocchi, A., Anderson, B.W., Levitt, D.G. (1990). Physiological measurements of luminal stirring in the dog and human small bowel. *J. Clin. Invest.*, 86, 1540–1547.

71. Lennernäs, H. (2007). Intestinal permeability and its relevance for absorption and elimination. *Xenobiotica*, 37, 1015–1051.

72. Sugano, K. (2011). Fraction of a dose absorbed estimation for structurally diverse low solubility compounds. *Int. J. Pharm.*, 405, 79–89.

73. Wang, Y., Brasseur, J.G., Banco, G.G., Webb, A.G., Ailiani, A.C., Neuberger, T. (2010). A multiscale lattice Boltzmann model of macro- to micro-scale transport, with applications to gut function. *Philos. Trans. R. Soc. London, Ser. A*, 368, 2863–2880.

74. Knutson, T., Fridblom, P., Ahlstrom, H., Magnusson, A., Tannergren, C., Lennernas, H. (2008). Increased understanding of intestinal drug permeability determined by the LOC-I-GUT approach using multislice computed tomography. *Mol. Pharm.*, 6, 2–10.

75. Pappenheimer, J.R. (1998). Scaling of dimensions of small intestines in non-ruminant eutherian mammals and its significance for absorptive mechanisms. *Comp. Biochem. Physiol., A Mol. Integr. Physiol.*, 121, 45–58.

76. Schiller, C., Frohlich, C.P., Giessmann, T., Siegmund, W., Monnikes, H., Hosten, N., Weitschies, W. (2005). Intestinal fluid volumes and transit of dosage forms as assessed by magnetic resonance imaging. *Aliment. Pharmacol. Ther.*, 22, 971–979.

77. Marciani, L., Cox Eleanor, F., Hoad Caroline, L., Pritchard, S., Totman John, J., Foley, S., Mistry, A., Evans, S., Gowland Penny, A., Spiller Robin, C. (2010). Postprandial changes in small bowel water content in healthy subjects and patients with irritable bowel syndrome. *Gastroenterology*, 138, 469–477, e461.

78. Sutton, S.C. (2009). Role of physiological intestinal water in oral absorption. *AAPS J.*, 11, 277–285.

79. Tachibana, T., Kato, M., Watanabe, T., Mitsui, T., Sugiyama, Y. (2009). Method for predicting the risk of drug-drug interactions involving inhibition of intestinal CYP3A4 and P-glycoprotein. *Xenobiotica*, 39, 430–443.

80. Sugano, K., Shirasaka, Y., Yamashita, S., Velicky, M., Bradley, D.F., Tam, K.Y., Dryfe, R.A. (2011). Estimation of Michaelis-Menten constant of efflux transporter considering asymmetric permeability. Fraction of a dose absorbed estimation for

structurally diverse low solubility compounds. In situ artificial membrane permeation assay under hydrodynamic control: permeability-pH profiles of warfarin and verapamil. *Int. J. Pharm*., 8, 8.

81. Sugano, K., Kataoka, M., Mathews, Cd.C., Yamashita, S. (2010). Prediction of food effect by bile micelles on oral drug absorption considering free fraction in intestinal fluid. *Eur. J. Pharm. Sci*., 40, 118–124.

82. Freire, A.C., Basit, A.W., Choudhary, R., Piong, C.W., Merchant, H.A. (2011). Does sex matter? The influence of gender on gastrointestinal physiology and drug delivery. *Int. J. Pharm*., 415, 15–28.

83. Diakidou, A., Vertzoni, M., Goumas, K., Soederlind, E., Abrahamsson, B., Dressman, J., Reppas, C. (2009). Characterization of the contents of ascending colon to which drugs are exposed after oral administration to healthy adults. *Pharm. Res*., 26, 2141–2151.

84. Lindahl, A., Ungell, A.-L., Knutson, L., Lennernaes, H. (1997). Characterization of fluids from the stomach and proximal jejunum in men and women. *Pharm. Res*., 14, 497–502.

85. Yamada, I., Goda, T., Kawata, M., Ogawa, K. (1990). Use of gastric acidity-controlled beagle dogs in bioavailability studies of cinnarizine. *Yakugaku Zasshi*, 110, 280–285.

86. Polentarutti, B., Albery, T., Dressman, J., Abrahamsson, B. (2010). Modification of gastric pH in the fasted dog. *J. Pharm. Pharmacol*., 62, 462–469.

87. Akimoto, M., Nagahata, N., Furuya, A., Fukushima, K., Higuchi, S., Suwa, T. (2000). Gastric pH profiles of beagle dogs and their use as an alternative to human testing. *Eur. J. Pharm. Biopharm*., 49, 99–102.

88. Sagawa, K., Li, F., Liese, R., Sutton, S.C. (2009). Fed and fasted gastric pH and gastric residence time in conscious beagle dogs. *J. Pharm. Sci*., 98, 2494–2500.

89. Dietschy, J.M. (1968). Mechanisms for the intestinal absorption of bile acids. *J. Lipid Res*., 9, 297–309.

90. McConnell, E.L., Basit, A.W., Murdan, S. (2008). Measurements of rat and mouse gastrointestinal pH, fluid and lymphoid tissue, and implications for in-vivo experiments. *J. Pharm. Pharmacol*., 60, 63–70.

91. Said, H.M., Blair, J.A., Lucas, M.L., Hilburn, M.E. (1986). Intestinal surface acid microclimate in vitro and in vivo in the rat. *J. Lab. Clin. Med*., 107, 420–424.

92. Shiau, Y.F., Fernandez, P., Jackson, M.J., McMonagle, S. (1985). Mechanisms maintaining a low-pH microclimate in the intestine. *Am. J. Physiol*., 248, G608–G617.

93. Lee, K.J., Johnson, N., Castelo, J., Sinko, P.J., Grass, G., Holme, K., Lee, Y.H. (2005). Effect of experimental pH on the in vitro permeability in intact rabbit intestines and Caco-2 monolayer. *Eur J Pharm Sci*., 25, 193–200.

94. Hoegerle, M.L., Winne, D. (1983). Drug absorption by the rat jejunum perfused in situ. Dissociation from the pH-partition theory and role of microclimate-pH and unstirred layer. *Naunyn Schmiedebergs Arch. Pharmacol*., 322, 249–255.

95. McNeil, N.I., Ling, K.L., Wager, J. (1987). Mucosal surface pH of the large intestine of the rat and of normal and inflamed large intestine in man. *Gut*, 28, 707–713.

96. Genz, A.K., v Engelhardt, W., Busche, R. (1999). Maintenance and regulation of the pH microclimate at the luminal surface of the distal colon of guinea-pig. *J. Physiol*., 517(Pt.2), 507–519.

97. Yamaguchi, T., Ikeda, C., Sekine, Y. (1986). Intestinal absorption of a b-adrenergic blocking agent nadolol. I. Comparison of absorption behavior of nadolol with those of other b-blocking agents in rats. *Chem. Pharm. Bull*., 34, 3362–3369.

98. Yamaguchi, T., Ikeda, C., Sekine, Y. (1986). Intestinal absorption of a b-adrenergic blocking agent nadolol. II. Mechanism of the inhibitory effect on the intestinal absorption of nadolol by sodium cholate in rats. *Chem. Pharm. Bull*., 34, 3836–3843.

99. Yamaguchi, T., Oida, T., Ikeda, C., Sekine, Y. (1986). Intestinal absorption of a b-adrenergic blocking agent nadolol. III. Nuclear magnetic resonance spectroscopic study on nadolol-sodium cholate micellar complex and intestinal absorption of nadolol derivatives in rats. *Chem. Pharm. Bull*., 34, 4259–4264.

100. Amidon, G.E., Higuchi, W.I., Ho, N.F.H. (1982). Theoretical and experimental studies of transport of micelle-solubilized solutes. *J. Pharm. Sci*., 71, 77–84.

101. Ingels, F., Beck, B., Oth, M., Augustijns, P. (2004). Effect of simulated intestinal fluid on drug permeability estimation across Caco-2 monolayers. *Int. J. Pharm*., 274, 221–232.

102. Poelma, F.G.J., Breaes, R., Tukker, J.J. (1990). Intestinal absorption of drugs. III. The influence of taurocholate on the disappearance kinetics of hydrophilic and lipophilic drugs from the small intestine of the rat. *Pharm. Res*., 7, 392–397.

103. Poelma, F.G.J., Breas, R., Tukker, J.J., Crommelin, D.J.A. (1991). Intestinal absorption of drugs. The influence of mixed micelles on the disappearance kinetics of drugs from the small intestine of the rat. *J. Pharm. Pharmacol*., 43, 317–324.

104. Tangerman, A., van Schaik, A., van der Hoek, E.W. (1986). Analysis of conjugated and unconjugated bile acids in serum and jejunal fluid of normal subjects. *Clin. Chim. Acta*, 159, 123–132.

105. Kalantzi, L., Goumas, K., Kalioras, V., Abrahamsson, B., Dressman, J.B., Reppas, C. (2006). Characterization of the human upper gastrointestinal contents under conditions simulating bioavailability/bioequivalence studies. *Pharm. Res*., 23, 165–176.

106. Perez de la Cruz Moreno, M., Oth, M., Deferme, S., Lammert, F., Tack, J., Dressman, J., Augustijns, P. (2006). Characterization of fasted-state human intestinal fluids collected from duodenum and jejunum. *J. Pharm. Pharmacol*., 58, 1079–1089.

107. Meier, Y., Eloranta, J.J., Darimont, J., Ismair, M.G., Hiller, C., Fried, M., Kullak-Ublick, G.A., Vavricka, S.R. (2007). Regional distribution of solute carrier mRNA expression along the human intestinal tract. *Drug Metab. Dispos*., 35, 590–594.

108. Lennernaes, H., Regaardh, C.G. (1993). Evidence for an interaction between the b-blocker pafenolol and bile salts in the intestinal lumen of the rat leading to dose-dependent oral absorption and double peaks in the plasma concentration-time profile. *Pharm. Res*., 10, 879–883.

109. Ladas, S.D., Isaacs, P.E., Murphy, G.M., Sladen, G.E. (1984). Comparison of the effects of medium and long chain triglyceride containing liquid meals on gall bladder and small intestinal function in normal man. *Gut*., 25, 405–411.

110. Hopman, W.P., Jansen, J.B., Rosenbusch, G., Lamers, C.B. (1984). Effect of equimolar amounts of long-chain triglycerides and medium-chain triglycerides on plasma cholecystokinin and gallbladder contraction. *Am. J. Clin. Nutr*., 39, 356–359.

111. Scholz, A., Abrahamsson, B., Diebold, S.M., Kostewicz, E., Polentarutti, B.I., Ungell, A.-L., Dressman, J.B. (2002). Influence of hydrodynamics and particle size on the absorption of felodipine in labradors. *Pharm. Res*., 19, 42–46.

112. Kalantzi, L., Persson, E., Polentarutti, B., Abrahamsson, B., Goumas, K., Dressman, J.B., Reppas, C. (2006). Canine intestinal contents vs. simulated media for the assessment of solubility of two weak bases in the human small intestinal contents. *Pharm. Res*., 23, 1373–1381.

113. Englund, G., Rorsman, F., Roennblom, A., Karlbom, U., Lazorova, L., Grasjoe, J., Kindmark, A., Artursson, P. (2006). Regional levels of drug transporters along the human intestinal tract: co-expression of ABC and SLC transporters and comparison with Caco-2 cells. *Eur. J. Pharm. Sci*., 29, 269–277.

114. Cao, Xea. (2006). Why is it challenging to predict intestinal drug absorption and oral bioavailability in human using rat model. *Pharm. Res*., 23, 1675–1686.

115. Aller, S.G., Yu, J., Ward, A., Weng, Y., Chittaboina, S., Zhuo, R., Harrell, P.M., Trinh, Y.T., Zhang, Q., Urbatsch, I.L., Chang, G. (2009). Structure of P-glycoprotein reveals a molecular basis for poly-specific drug binding. *Science (Washington, DC)*, 323, 1718–1722.

116. Mouly, S., Paine, M.F. (2003). P-glycoprotein increases from proximal to distal regions of human small intestine. *Pharm. Res*., 20, 1595–1599.

117. Makhey, V.D., Guo, A., Norris, D.A., Hu, P., Yan, J., Sinko, P.J. (1998). Characterization of the regional intestinal kinetics of drug efflux in rat and human intestine and in Caco-2 cells. *Pharm. Res*., 15, 1160–1167.

118. Thorn, M., Finnstrom, N., Lundgren, S., Rane, A., Loof, L. (2005). Cytochromes P450 and MDR1 mRNA expression along the human gastrointestinal tract. *Br. J. Clin. Pharmacol*., 60, 54–60.

119. Katoh, M., Suzuyama, N., Takeuchi, T., Yoshitomi, S., Asahi, S., Yokoi, T. (2006). Kinetic analyses for species differences in P-glycoprotein-mediated drug transport. *J. Pharm. Sci*., 95, 2673–2683.

120. Paine, M.F., Hart, H.L., Ludington, S.S., Haining, R.L., Rettie, A.E., Zeldin, D.C. (2006). The human intestinal cytochrome P450 "pie". *Drug Metab. Dispos*., 34, 880–886.

121. Beaumont, K., The importance of gut wall metabolism in determining drug bioavailability, in: H. van de Waterbeemd, H. Lennernäs, P. Artursson (Eds.) Drug Bioavailability: Estimation of Solubility, Permeability, Absorption and Bioavailability, Wiley-VCH Verlag GmbH & Co. KGaA, New York, 2003, pp. 311–328.

122. Borgstrom, L., Nyberg, L., Jonsson, S., Lindberg, C., Paulson, J. (1989). Pharmacokinetic evaluation in man of terbutaline given as separate enantiomers and as the racemate. *Br. J. Clin. Pharmacol*., 27, 49–56.

123. Hochhaus, G., Mollmann, H. (1992). Pharmacokinetic/pharmacodynamic characteristics of the beta-2-agonists terbutaline, salbutamol and fenoterol. *Int. J. Clin. Pharmacol. Ther. Toxicol*., 30, 342–362.

124. Mizuma, T., Kawashima, K., Sakai, S., Sakaguchi, S., Hayashi, M. (2005). Differentiation of organ availability by sequential and simultaneous analyses: intestinal conjugative metabolism impacts on intestinal availability in humans. *J. Pharm. Sci*., 94, 571–575.

125. Roberts, M.S., Magnusson, B.M., Burczynski, F.J., Weiss, M. (2002). Enterohepatic circulation: physiological, pharmacokinetic and clinical implications. *Clin. Pharmacokinet*., 41, 751–790.

126. Matheson, P.J., Wilson, M.A., Garrison, R.N. (2000). Regulation of intestinal blood flow. *J. Surg. Res*., 93, 182–196.

127. Yang, J., Jamei, M., Yeo, K.R., Tucker, G.T., Rostami-Hodjegan, A. (2007). Prediction of intestinal first-pass drug metabolism. *Curr. Drug Metab.*, 8, 676–684.

128. Nomeir, A.A., Morrison, R., Prelusky, D., Korfmacher, W., Broske, L., Hesk, D., McNamara, P., Mei, H. (2009). Estimation of the extent of oral absorption in animals from oral and intravenous pharmacokinetic data in drug discovery. *J. Pharm. Sci.*, 98, 4027–4038.

129. Olanoff, L.S., Walle, T., Cowart, T.D., Walle, U.K., Oexmann, M.J., Conradi, E.C. (1986). Food effects on propranolol systemic and oral clearance: support for a blood flow hypothesis. *Clin. Pharmacol. Ther.*, 40, 408–414.

130. Lemmer, B., Nold, G. (1991). Circadian changes in estimated hepatic blood flow in healthy subjects. *Br. J. Clin. Pharmacol.*, 32, 627–629.

131. Langner, B., Lemmer, B. (1988). Circadian changes in the pharmacokinetics and cardiovascular effects of oral propranolol in healthy subjects. *Eur. J. Clin. Pharmacol.*, 33, 619–624.

132. Lemmer, B., Nold, G., Behne, S., Kaiser, R. (1991). Chronopharmacokinetics and cardiovascular effects of nifedipine. *Chronobiol. Int.*, 8, 485–494.

133. Lemmer, B., Scheidel, B., Blume, H., Becker, H.J. (1991). Clinical chronopharmacology of oral sustained-release isosorbide-5-mononitrate in healthy subjects. *Eur. J. Clin. Pharmacol.*, 40, 71–75.

134. Shaffer, E.A. (2000). Review article: control of gall-bladder motor function. *Aliment. Pharmacol. Ther.*, 14 (Suppl. 2), 2–8.

135. Merck. *Merck Manual* http://merckmanual.jp/mmpej/seco3/cho0/cho30/cho3oa.html.

136. Ghibellini, G., Leslie, E.M., Brouwer, K.L. (2006). Methods to evaluate biliary excretion of drugs in humans: an updated review. *Mol. Pharm.*, 3, 198–211.

137. Yang, X., Gandhi, Y.A., Duignan, D.B., Morris, M.E. (2009). Prediction of biliary excretion in rats and humans using molecular weight and quantitative structure-pharmacokinetic relationships. *AAPS J.*, 11, 511–525.

138. Soane, R.J., Frier, M., Perkins, A.C., Jones, N.S., Davis, S.S., Illum, L. (1999). Evaluation of the clearance characteristics of bioadhesive systems in humans. *Int. J. Pharm.*, 178, 55–65.

139. Ugwoke, M.I., Verbeke, N., Kinget, R. (2001). The biopharmaceutical aspects of nasal mucoadhesive drug delivery. *J. Pharm. Pharmacol.*, 53, 3–21.

140. Patton, J.S., Fishburn, C.S., Weers, J.G. (2004). The lungs as a portal of entry for systemic drug delivery. *Proc. Am. Thorac. Soc.*, 1, 338–344.

141. Hardy, J.G., Chadwick, T.S. (2000). Sustained release drug delivery to the lungs: an option for the future. *Clin. Pharmacokinet.*, 39, 1–4.

142. Bouwstra, J.A., Honeywell-Nguyen, P. L., Gooris, G.S., Ponec, M. (2003). Structure of the skin barrier and its modulation by vesicular formulations. *Prog. Lipid Res.*, 42, 1–36.

143. Hadgraft, J. (2004). Skin deep. *Eur. J. Pharm. Biopharm.*, 58, 291–299.

144. Talreja, P., Kleene, N.K., Pickens, W.L., Wang, T.F., Kasting, G.B. (2001). Visualization of the lipid barrier and measurement of lipid pathlength in human stratum corneum. *AAPS Pharm. Sci.*, 3, E13.

145. de Jager, M.W., Gooris, G.S., Dolbnya, I.P., Ponec, M., Bouwstra, J.A. (2004). Modelling the stratum corneum lipid organisation with synthetic lipid mixtures: the importance of synthetic ceramide composition. *Biochim. Biophys. Acta*, 1664, 132–140.